SEARCH FOR PAIR PRODUCTION OF SCALAR TOP QUARKS DECAYING TO A τ LEPTON AND A b QUARK IN 1.96-TEV $p\bar{p}$ COLLISIONS

A Dissertation

by

VADIM KHOTILOVICH

Submitted to the Office of Graduate Studies of
Texas A&M University
in partial fulfillment of the requirements for the degree of

DOCTOR OF PHILOSOPHY

May 2008

Major Subject: Physics

SEARCH FOR PAIR PRODUCTION OF SCALAR TOP QUARKS DECAYING TO A τ LEPTON AND A b QUARK IN 1.96-TEV $p\bar{p}$ COLLISIONS

A Dissertation

by

VADIM KHOTILOVICH

Submitted to the Office of Graduate Studies of
Texas A&M University
in partial fulfillment of the requirements for the degree of

DOCTOR OF PHILOSOPHY

Approved by:

Co-Chairs of Committee,	Teruki Kamon
	Alexei Safonov
Committee Members,	David Toback
	Richard Arnowitt
	Stephen Fulling
Head of Department,	Edward Fry

May 2008

Major Subject: Physics

ABSTRACT

Search for Pair Production of Scalar Top Quarks Decaying to
a τ Lepton and a b Quark in 1.96-TeV $p\bar{p}$ Collisions. (May 2008)
Vadim Khotilovich, B.S., Belarus State University
Co–Chairs of Advisory Committee: Dr. Teruki Kamon
Dr. Alexei Safonov

I present the results of a search for pair production of scalar top quarks ($\tilde{t}_1$) in an R-parity violating supersymmetric scenario using 322 pb^{-1} of $p\overline{p}$ collisions at $\sqrt{s} = 1.96$ TeV collected by the upgraded Collider Detector at Fermilab. I assume each $\tilde{t}_1$ decays into a τ lepton and a b quark, with branching ratio β, and search for final states containing either an electron or a muon from a leptonic τ decay, a hadronically decaying τ lepton, and two or more jets. Two candidate events pass my final selection criteria, consistent with the expectation from standard model processes. I present upper limits on the cross section times branching ratio squared $\sigma(\tilde{t}_1\bar{\tilde{t}}_1) \times \beta^2$ as a function of the stop mass $m(\tilde{t}_1)$. Assuming $\beta = 1$, I set a 95% confidence level limit $m(\tilde{t}_1) > 153$ GeV/c^2. These limits are also fully applicable to the case of a pair produced third generation scalar leptoquark that decays into a τ lepton and a b quark.

To my parents, Gennady Yulianovich and Donata Fadeevna Khotilovich.

ACKNOWLEDGMENTS

First, I would like to thank all of the Fermilab staff, my CDF collaborators, and all the people that were involved in building and maintaining the Tevatron and the CDF detector. Without your contribution this work would have been impossible. I have gained a great amount of experience working as a part of a big scientific collaboration and about running a big scale experiment. Thank you for making it an enjoyable process.

I am very grateful to my advisors, Dr. Teruki Kamon and Dr. Alexei Safonov, for their extremely valuable guidance and enormous patience throughout my research work. I started to work with Dr. Teruki Kamon right after coming to Texas A&M University (TAMU), and during this time he was always there if I needed help or encouragement. He introduced me to the world of experimental searches for new high energy physics phenomena, and I could always rely on his vast knowledge and experience in this area. Dr. Safonov was closely involved and co-directed my work since the first baby steps of this analysis. His sharp insights helped to solve a lot of problems that arose during the study. I feel fortunate to have valuable lessons learned from him and am glad to be his friend.

It is my pleasure to thank everybody who was directly involved in this analysis at its various stages: Takashi Ogawa, Takashi Akimoto, Dr. Maxwell Chertok, and Dr. Richard Lander. Also thanks to the members of the lepton plus track trigger group for creating and studying this very important for this analysis tool. Those people include Dr. Sasha Baroiant, Dr. John Smith, Dr. Fedor Ratnikov, Dr. Maxim Goncharov, Dr. Carmine Pagliarone, Dr. Elena Vataga, and Dr. Aurore Savoy-Navarro. I am thankful for many helpful discussions about tau identification and software issues with Dr. Fedor Ratnikov, Dr. Pasha Murat, and Dr. John Conway. And thanks

to Dr. Stephan Lammel, Dr. Beate Heinemann, and Dr. Song-Ming Wan for useful physics and technical discussions.

I feel fortunate to have had a great team of colleagues at the TAMU CDF group. Many thanks go to Dr. Vyacheslav Krutelyov. With his help I joined graduate school at TAMU, and he could always provide valuable technical expertise. I would like to express my gratitude to Dr. David Toback for his insights on physics issues and for his time spent to improve the quality and English of various drafts that he got from me. To Dr. Maxim Goncharov, thank you for always offering your help and advice. Thanks to Dr. Sung-Won Lee and Dr. Michael Weinberger for being great officemates. And I am glad to have Jonathan Asaadi, Dr. Peter Wagner, Matthew Cervantes, and Christopher Battle as awesome friends. A special thank goes to my theory colleagues, Dr. Richard Arnowitt and Dr. Bhaskar Dutta, for enriching my knowledge of theoretical and phenomenological high energy physics.

I thank Dr. Tony Liss, Dr. Kenneth Osterberg, and Dr. Christopher Neu for being of great help during the preparation of the paper on this dissertation topic.

I appreciate the members of my dissertation committee: Dr. Teruki Kamon, Dr. Alexei Safonov, Dr. David Toback, Dr. Richard Arnowitt, and Dr. Stephen Fulling, for their overview of my progress and for many useful suggestions that improved my presentation and the dissertation.

I would also like to thank Sandi Smith, the Department of Physics at TAMU stuff, and Carol Picciolo for always being helpful with paperwork, academic, and administrative issues.

Finally, my deep gratitude goes to my parents, Gennady Yulianovich and Donata Fadeevna Khotilovich, and my sister Rimma Khotilovich for their love, trust, and just being there while not seeing me for years. I can't thank you enough.

TABLE OF CONTENTS

CHAPTER Page

CHAPTER Page

CHAPTER Page

LIST OF FIGURES

FIGURE Page

FIGURE Page

FIGURE Page

FIGURE Page

LIST OF TABLES

TABLE Page

TABLE Page

CHAPTER I

INTRODUCTION: THEORETICAL AND OBSERVATIONAL MOTIVATIONS FOR THE SEARCH

A. Introduction

We, as experimental particle physicists, have the ultimate goal of discovering deeper and more fundamental laws of nature. One way is to follow up on the multitude of hypotheses and models proposed by theorists. If we choose this path then our task is to to pick the ones which are most consistent with reality and to reject those which fail experimental checks. For this dissertation we choose a particular model and perform a search for a particular signature. Even though the result of our search might turn out to be negative, we can expect to set limits on some of model's parameters, which are worthy addition to the knowledge bank of science.

In this introduction we begin with an overview of the search and a few notes about the motivation for it. More details on the standard model (SM) of particle physics can be found in Section I.B and Section I.C provides more details on supersymmetric theories.

The SM is well respected theory that describes the vast majority of existing experimental data [1]. However, there are experimental observations and theoretical shortcomings (see Section I.B for details) which give us hints that the SM is only an effective theory, i.e. that it is an approximation of some more general theory. One of such more general hypotheses that has the potential to solve some of the problems

---

This dissertation follows the style of Physical Review D.

associated with SM, is the the hypothesis of supersymmetry [2, 3] (or SUSY, see Section I.C for details). Theories based on this hypothesis introduce a supersymmetric partner to every SM particle, specifically, a symmetry between the fundamental fermions and bosons in the nature. For example, spin-1/2 quarks and leptons have spin-0 quark and lepton superpartners. A multiplicative quantum number called R-parity (R_p) separates SM and SUSY species [4, 5]. It is equal to 1 for all SM particles and it is -1 for all supersymmetric particles.

SUSY theories are divided into R_p conserving models and R_p violating ($\not{R}_p$ or RPV) ones. Specifically, to conserve R_p any SUSY particle's decay can only produce odd number of SUSY particles. Thus, superparticles always would have at least one lighter SUSY particle in their decay if R_p is conserved, but if R_p is violated they can decay into ordinary SM quarks and/or leptons. There is no experimental evidence that R_p has to be conserved. However, experimental limits have been set on the strength of $\not{R}_p$ couplings [6] (for a detailed discussion of RPV SUSY see Section I.C.1).

Experimental data suggest that the superpartners of the first and second generation of fermions have masses greater than those of the standard model particles, while the mass of the lighter stop is weakly constrained and can be below that of the top quark [7]. This is due to the mixing between the left and right handed interaction eigenstates which is a function of the large Yukawa coupling of the top quark [3]. Within the framework of $\not{R}_p$ SUSY [4, 5], theoretical studies indicate that the decay mode for the light stop $\tilde{t}_1 \rightarrow \tau b$ is dominant for a wide range of SUSY model parameters [8, 9, 10], including the region favored by neutrino oscillation data [11, 12]. It should be noted that lepton number is violated in neutrino oscillations, and RPV SUSY theories with lepton number violation provide a natural explaination for this phenomenon as well as for neutrino mass generation, which gives a strong motivation for RPV searches. More details on motivations for the search from the theoretical

and experimental points of view are given in Sections I.B and I.C of this chapter.

In this search we look for experimental evidence of supersymmetry by investigating $p\overline{p}$ collisions for the presence of pair production of scalar top quarks (stop or $\tilde{t}_1$) that may undergo RPV decays into a tau lepton and a b quark. Our data is collected using the upgraded Collider Detector at Fermilab (CDF II) between March 2002 and August 2004 (the CDF II detector is describerd in Section II.B). The specific signature that we look is $p\overline{p}\rightarrow\tilde{t}_1\bar{\tilde{t}}_1\rightarrow\tau_l\tau_{\rm h}b\bar{b}$ with a final state with either an electron or muon from the decay $\tau_l \rightarrow l\nu_l\nu_\tau$ ($l =$ e or μ), a hadronically decaying tau $\tau_{\rm h}$, missing energy from the neutrinos, which are not detected by CDF, and two or more jets. A similar search was performed at CDF in Run I [13] and set a 95% confidence level (C.L.) limit on $m(\tilde{t}_1) > 122$ GeV/c^2. Comparing to Run I, the CDF II detector has improved muon detection coerage (Section II.B.3) and improved system for preselection of events with tau leptons (see Section III.A). Also, the center-of-mass energy of $p\overline{p}$ collisions at the Fermilab Tevatron was increased from 1.8 TeV to 1.96 TeV, which is expected to give a substantial increase in the $\tilde{t}_1\bar{\tilde{t}}_1$ production rate (Section IV.B), e.g. for $m(\tilde{t}_1) = 155$ GeV/c^2 the cross section grows by $\sim 35\%$.

It should also be noted that scalar top decaying into tau and b could be interpreted as a third generation scalar leptoquark (LQ_3). Some theories predict the existence of interactions between quarks and leptons which are mediated by leptoquarks [14], a new type of particles that carries both lepton and baryon number, are color triplet bosons with spin 0 or 1, and have fractional charge. The theoretical expectation that $\mathcal{B}(LQ_3 \rightarrow \tau b) = 1$ while $m(LQ_3) < m(t)$ is an additional motivation for the search. Previous LQ_3 searches at LEP [15] (model independent) and CDF [16] resulted in a 95% C.L. limit on $m(\tilde{t}_1) > 99$ GeV/c^2. More information on LQ theories and the interpretation of our results in terms of the models is given in Appendix D.

This analys has been approved for submission to Phys. Rev. Lett. by the CDF

Collaboration. A summary of the analysis can be found in Ref. [17].

B. The Standard Model of Particle Physics and Its Limitations

Now that have quickly given an overview of the search we give a more detailed discusion of the SM and its limitations with an eye towards potential solutions.

The SM is a gauge theory that combines the strong, weak, and electromagnetic interactions. In mathematical terms, the fields of these interactions are the representations of the $SU(3)_C \times SU(2)_L \times U(1)_Y$ symmetry groups, where $SU(3)_C$ corresponds to the quantum chromodynamics (QCD) theory of the strong interaction, and the $SU(2)_L \times U(1)_Y$ gauge groups corresponds to the electroweak interaction. This symmetry is spontaneously broken to $SU(3)_C \times U(1)_{EM}$ by the nonvanishing vacuum expectation value of a fundamental scalar field, the Higgs field doublet [1]. This symmetry breaking mechanism transforms the massless gauge particle eigenstates of the model into mass eigenstates, which have masses that can be experimentally measured.

The SM contains three generations of fermions, that contain the fundamental constituents of matter. It also contains four kinds of vector gauge bosons which serve as interaction carriers: gluons for the strong interactions, the W and Z bosons for the weak interactions, and photon for the electromagnetic. The scalar Higgs boson is the only SM particle which has been predicted but has not observed as yet. Table I presents the particle content of the SM. Perturbative expansion of the interaction lagrangian allows for a set of possible Feynman diagrams and rules, which present, in a visually clear fashion, the matrix elements for any interaction process to any desired order of perturbation theory.

Despite all its experimental success, the SM is considered an incomplete description of the particle world. The following list presents a set of the theoretical

TABLE I: The fundamentsl particle content of the standard model. The mass values are taken from the Particle Data Group [18]. We use notations Q and S for charge and spin of particles respectively. We do not provide uncertainties for the mass values which have higher know precision than that shown in this table.

	Fermion Generation		
	1	2	3
Quarks	u	c	t
	$1.5 - 3.0$ MeV/c^2	1.25 ± 0.09 GeV/c^2	174.2 ± 3.3 GeV/c^2
		$Q = +\frac{2}{3}$	
	d	s	b
	$3 - 7$ MeV/c^2	95 ± 25 MeV/c^2	4.20 ± 0.07 GeV/c^2
		$Q = -\frac{1}{3}$	
Leptons	e	μ	τ
	0.511 MeV/c^2	106 MeV/c^2	1.78 GeV/c^2
		$Q = -1$	
	ν_e	ν_μ	ν_τ
	< 3 eV/c^2	< 0.19 MeV/c^2	< 18.2 MeV/c^2
		$Q = 0$	
Bosons	γ	$m(\gamma) < 6 \times 10^{-17}$ eV	Q=0, S=1
	$W^\pm$	$m(W^\pm) = 80.4$ GeV/c^2	Q=$\pm$1, S=1
	Z^0	$m(Z^0) = 91.2$ GeV/c^2	Q=0, S=1
	H^0	$m(H^0) > 114$ GeV/c^2	Q=0, S=0

shortcomings of the SM and questions which they raise.

- A large number of free parameters: the three gauge couplings, the matrices of the Yukawa couplings, the Higgs parameters, mixing angles and phases [1]. Essentially, 18 parameters in the core theory, plus the values of G, c and $\hbar$. Are they all really independent and arbitrarily defined in nature?

- Choice and structure of the gauge group: why do we have three independent symmetry groups?

- How is the electroweak symmetry broken? Is the Higgs boson, which was put into the theory as a "convenient remedy", really a fundamental particle? Does it exist?
- Number of generations: why do we have three generations?
- Why do electrons and protons have the same but opposite charge?
- Mass spectrum: what is the reason each particle has the mass value it has? Why is the variation so large?
- The Higgs mass is divergent from radiative corrections in the SM. What is the proper mechanism for determining its mass while not introducing a cut-off value at some high high energy scale[1] [3]?
- Why do the interaction couplings not converge to the same value at high energies [3]?
- If neutrinos are not massless [19], how can they be properly incorporated into the SM?
- How is gravity, the fourth kind of interactions, incorporated into our understanding of particle interactions?

The SM provides no answer to these questions.

Even though there is high precision agreement between the SM predictions with experiment, there are some experimental observations that the SM is not able to explain. The first one is the evidence of massive neutrinos (see Ref. [19] for a recent review). Second, current cosmological observations show that the Universe consists

[1]It is often called as "naturalness" or "hierarchy" problem of the SM.

of 73% of dark energy, 23% of cold dark matter, and only 4% of visible matter that is described by the particle content of the SM [20, 21]. Finally, a very precise measurement of the muon anomalous magnetic moment $a_\mu = (g_\mu - 2)/2$ was performed at Brookhaven National Laboratory [22] and the difference between this measured value and the SM predictions [23] is 3.3σ.

Unsatisfied with the problems of the SM, theorists have searched for new models. Some, but not all, of the outlined questions and all the mentioned above experimental problems can be solved in supersymmetric theories.

C. Supersymmetry

Supersymmetric theories have emerged as the strongest candidates for physics beyond the SM to explain the above problems. Supersymmetry provides a solution to the Higgs mass "naturalness" problem of the SM and displays a gauge couplings unification at high energy scale [3]. SUSY also provides insights on the origins of radiative electroweak symmetry breaking[2]. R-parity violating SUSY models allow interpretation of the experimental evidence for massive neutrinos, which is a strong motivation for our analysis (described more in Section I.C.1). Many R_p conserving SUSY models provide good candidates for cold dark matter [21]. Finally, in SUSY it is possible to precisely match the observed muon anomalous magnetic moment value [24]. The following predictions of SUSY turned out to be true: heaviness of the top quark, the value of $\sin^2\theta_W$, requirement of a relatively light Higgs boson (current measurements suggest that $m(H) < 250$ GeV/c^2). Despite all these successful explanations and predictions, SUSY has not been directly discovered yet experimentally.

[2]Note that the explanation is not from a "first principles" understanding of supersymmetry itself, but would come from a deeper level theory that explains supersymmetry breaking itself.

Supersymmetry is based on the introduction of an anticommuting spinor operator which transforms a bosonic state into a fermionic state, and vice versa. This symmetry transforms every SM particle into its superpartner. Thus, regular fermions get superpartners of spin 0 which are conventionally named by adding a prefix "s" to particles names, and superpartners of regular bosons become carriers of spin 1/2 and are often distinguished by their "ino" suffix. The minimal supersymmetric model (MSSM) includes the minimal possible number of supersymmetric particles.

The gauge and mass eigenstates of the MSSM are listed in Table II. It shows that the particle content of the MSSM is more complicated than just a simple mirroring of the SM particle spectrum. For example, the description of electroweak symmetry breaking in the MSSM requires two Higgs doublets rather than just one in the SM [3]. The electroweak symmetry breaking mixes the gauge eigenstates and results in the mass eigenstates. The mixing for the first two generations of squarks is expected to be negligible [3] due to the small mass of their SM partners. Additional evidence comes from the experimental data, suggesting that the superpartners of the first and second generation are massive with masses greater than those of the SM particles [7]. However, the mixing for the third generation squarks and sleptons might be considerable and especially high for top squarks, due to the large mass of the top quark. This mass splitting allows a relatively light $\tilde{t}_1$, which could have mass even less than the top quark. It provides an important motivation for the $\tilde{t}_1\bar{\tilde{t}}_1$ production search, as light particles are more copiously produced in $p\bar{p}$ collisions at the Tevatron.

Since no SUSY particles have been observed yet, the vacuum states should not be invariant under supersymmetry and superparticles must have different masses than their SM partners. This implies that supersymmetry has to be spontaneously broken. Many possible models of spontaneous supersymmetry breaking have been proposed [25]. In the MSSM it is assumed that there is so-called soft supersymmetry

TABLE II: The particle content of the Minimal Supersymmetric Standard Model (with sfermion mixing for the first two families assumed to be negligible) [3].

Names	Spin	Gauge Eigenstates	Mass Eigenstates
Higgs bosons	0	$H_u^0\ H_d^0\ H_u^+\ H_d^-$	$h^0\ H^0\ A^0\ H^\pm$
squarks	0	$\widetilde{u}_L\ \widetilde{u}_R\ \widetilde{d}_L\ \widetilde{d}_R$	(same)
		$\widetilde{s}_L\ \widetilde{s}_R\ \widetilde{c}_L\ \widetilde{c}_R$	(same)
		$\widetilde{t}_L\ \widetilde{t}_R\ \widetilde{b}_L\ \widetilde{b}_R$	$\widetilde{t}_1\ \widetilde{t}_2\ \widetilde{b}_1\ \widetilde{b}_2$
sleptons	0	$\widetilde{e}_L\ \widetilde{e}_R\ \widetilde{\nu}_e$	(same)
		$\widetilde{\mu}_L\ \widetilde{\mu}_R\ \widetilde{\nu}_\mu$	(same)
		$\widetilde{\tau}_L\ \widetilde{\tau}_R\ \widetilde{\nu}_\tau$	$\widetilde{\tau}_1\ \widetilde{\tau}_2\ \widetilde{\nu}_\tau$
neutralinos	1/2	$\widetilde{B}^0\ \widetilde{W}^0\ \widetilde{H}_u^0\ \widetilde{H}_d^0$	$\widetilde{\chi}_1\ \widetilde{\chi}_2\ \widetilde{\chi}_3\ \widetilde{\chi}_4$
charginos	1/2	$\widetilde{W}^\pm\ \widetilde{H}_u^+\ \widetilde{H}_d^-$	$\widetilde{\chi}_1^\pm\ \widetilde{\chi}_2^\pm$
gluino	1/2	$\widetilde{g}$	(same)
goldstino (gravitino)	1/2 (3/2)	$\widetilde{G}$	(same)

breaking which happens in a "hidden sector", which is some other theory outside of the MSSM's "visible sector". There is some suppressed interaction between the two sectors which carries the breaking from the hidden to visible sector. This interaction is carried out by "messenger" fields, which are some third kind of fields (neither SM particles nor their partners). This particular analysis does not depend explicitly on the breaking mechanism, however, the mechanism may influence the R-parity violation parametrization (see Section I.C.1).

1. *Supersymmetric Models and R-Parity Violation (RPV)*

An important quantum number which separates SM particles and their superpartners is R-parity:

$$R_p \;=\; (-1)^{\,2S+3B+L} \;=\; (-1)^{\,2S+3(B-L)} \;=\; \begin{cases} +1 & \text{for ordinary SM particles,} \\ -1 & \text{for their superpartners.} \end{cases} \tag{1.1}$$

where S, B, and L are correspondingly spin, baryon, and lepton numbers for a particle. If R_p is conserved (RPC) there are major phenomenological consequences:

- At colliders (or in loops) superpartners are produced in pairs.
- Heavy superpartners decays into one other superpartner (or an odd number of superpartners) and a SM particle.
- The lightest supersymmetric particle (LSP) is stable. This feature determines supersymmetry collider signatures and makes the LSP a good candidate for the cold dark matter of the universe.

There is no strict experimental evidence which would require RPC. From the perspective of solving the dark matter problem, the most dramatic implication of broken R_p is the instability of the LSP, which rules it out as a candidate for non-baryonic dark matter, unless $\not{R}_p$ couplings are small enough to provide a gigayear lifetime of the LSP. However, the dark matter problem may have other, non-supersymmetric solutions [21, 26]. Second argument against $\not{R}_p$ SUSY is that it might eliminate the baryon asymmetry of the universe, in case if it was generated before the electroweak phase transition. However, if it was generated during or after the electroweak phase transition, RPV can provide a new mechanism for the baryon asymmetry (see review in Ref. [5]). In short, there are no definite model-independent cosmological or

astrophysics restriction on RPV terms in SUSY.

The general renormalisable superpotential of the MSSM with the extension that allows RPV term has the only possible parametrization:

$$
\begin{aligned}
W &= W_{R_p} + W^{\not L}_{\not R_p} + W^{\not B}_{\not R_p} \,, && (1.2)\\
W_{R_p} &= \epsilon_{ab}\left(h^E_{ij} L^a_i H^b_d \bar{E}_j + h^D_{ij} Q^a_i H^b_d \bar{D}_j + h^U_{ij} Q^a_i H^b_u \bar{U}_j + \mu H^a_d H^b_u\right) \,, && (1.3)\\
W^{\not L}_{\not R_p} &= \epsilon_{ab}\left(\frac{1}{2}\lambda_{ijk} L^a_i L^b_j \bar{E}_k + \lambda'_{ijk} L^a_i Q^b_j \bar{D}_k + \mu_i L^a_i H^b_u\right) \,, && (1.4)\\
W^{\not B}_{\not R_p} &= \frac{1}{2}\epsilon_{rst}\lambda''_{ijk} \bar{U}^r_i \bar{D}^s_j \bar{D}^t_k \,, && (1.5)
\end{aligned}
$$

where, $i, j, k = 1, 2, 3$ are generation indices, $a, b = 1, 2$ are $SU(2)$ and $r, s, t = 1, 2, 3$ are the $SU(3)$ indices, and ϵ_{ab} and ϵ_{rst} are totally antisymmetric tensors. The L and $\bar{E}$ notations represent the lepton doublet and singlet left-chiral superfields; $Q, \bar{U}, \bar{D}$ denote the quark doublet and singlet superfields, respectively, $h^E,\ h^D,\ h^U, \lambda,\ \lambda',\ \lambda''$ are dimensionless coupling constants, and μ and μ_i are mass mixing parameters. The W_{R_p} superpotential is R_p conserving. $W^{\not L}_{\not R_p}$ and $W^{\not B}_{\not R_p}$ violate R_p and cause lepton or baryon number violation respectively. Gauge invariance enforces antisymmetry of the λ_{ijk} couplings with respect to their first two indices and antisymmetry of the λ''_{ijk} couplings with respect to their last two indices. Specifically:

$$
\lambda_{ijk} \;=\; -\lambda_{jik}, \qquad \lambda''_{ijk} \;=\; -\lambda''_{ikj} \,. \tag{1.6}
$$

Thus, the RPV lagrangian contains a total of 48 parameters: 3 mass parameters μ_i mixing the charged lepton and down-type Higgs superfields, and 45 dimensionless Yukawa-like couplings divided into 9 λ_{ijk} and 27 λ'_{ijk} couplings which break lepton number conservation, and 9 λ''_{ijk} couplings which break baryon number conservation.

It should be noted that the most general RPV parametrization also involves $\not R_p$ terms in the soft supersymmetry breaking Lagrangian density, and the values of the

couplings depend on the choice of the weak interaction basis [5]. For example, it is possible to rotate the basis so that $\mu_i = 0$. However, for most SUSY breaking mechanisms this would result in bilinear $\not{R}_p$ terms appearing in the soft supersymmetry breaking Lagrangian density. The maximal possible number of RPV parameters is rather large[3]: $48 + 51 - 3 = 96$. For experimental searches it is useful to assume that very limited set of couplings dominate. Typically, one assumes that a single coupling dominates. Orders of magnitude for the trilinear couplings constraints obtained from non-observation experiments are $\lambda,\ \lambda',\ \lambda'' < (10^{-2} \sim 10^{-1}) \times \widetilde{m}/(100\ \mathrm{GeV}/c^2)$ [5], involving generically a linear dependence on the superpartner mass $\widetilde{m}$.

Other experimental constraints on the $W^{\not{L}}_{\not{R}_p}$ and $W^{\not{B}}_{\not{R}_p}$ operators (Eqs. (1.3) and (1.5)) come from non-observation of proton decay. To stabilize the proton it is sufficient to prohibit either the superpotential $W^{\not{L}}_{\not{R}_p}$ or $W^{\not{B}}_{\not{R}_p}$. However, conserving L while allowing B violation is not discrete gauge anomaly-free [27]. Also, the experimental limits on λ''_{ikj} coming from the nucleon decay experiments are rather strong [5]. Because of these limits it is common to disregard the λ'' terms.

The advantage of having broken R_p with lepton number violation is that it allows for non-zero neutrino masses. On the other hand, the existing data on neutrino mass oscillations sets very strict limits on RPV couplings [5, 6, 11, 12, 28, 29], and constrains them to be in the range $\lambda'_{i33} < 10^{-3} \sim 10^{-5}$. The spread in predictions come from use of different soft SUSY breaking mechanisms, various approaches in simplifying the RPV parameters set or using different RPV anzats, or electroweak basis choice.

---

[3]Note: 48 comes from the superpotential parametrization (which introduces explicit R_p breaking), 51 is from the soft supersymmetry breaking Lagrangian density (introduces spontaneous R_p breaking), and the total number is reduced by 3 due to the basis choice freedom.

In our search we assume that the dominant contributing RPV coupling is λ'_{333} because it is responsible for the $\tilde{t}_1 \to \tau b$ decay mode. The branching ratio of this decay depends on the relative width of this channel compared to the total width of all other possible RPV and RPC decays of $\tilde{t}_1$ which are disfavored for variety of reasons. The most natural RPC decay channel $\tilde{t}_1 \to t\widetilde{\chi}_1^0$ would be kinematically available if $m(\tilde{t}_1) \geq m(t)+m(\widetilde{\chi}_1^0)$, and the decay mode $\tilde{t}_1 \to b\widetilde{\chi}_1^+$ is open if $m(\tilde{t}_1) \geq m(b)+m(\widetilde{\chi}_1^+)$. If either of these modes is open they would take almost 100% of branching ratio. Also the following 3-body RPC decay modes would be dominating if $\widetilde{l}$ or $\widetilde{\nu}$ are lighter than stop:

$$\tilde{t}_1 \to bl\widetilde{\nu}, \quad b\nu\widetilde{l} \ \text{(3-body modes)}. \tag{1.7}$$

The only observable RPV signatures in that case would be decays of LSP.

However, the situation is dramatically different if all of the mentioned above decay modes are not kinematically allowed and stop is the NLSP, there will be competition between two types of RPC decays [10, 11]:

$$\tilde{t}_1 \to c\widetilde{\chi}_1^0 \ \text{(loop induced through flavor changing neutral current)}; \tag{1.8}$$

$$\tilde{t}_1 \to b\widetilde{\chi}_1^0 f\bar{f}' \ \text{(4-body mode)}. \tag{1.9}$$

These decays are naturally suppressed due to their loop or 4-body mechanisms. In different regions of SUSY parameter space they may compete against each other and against RPV stop decays, even though $\not{R}_p$ couplings could be as low as $10^{-3} \sim 10^{-5}$.

Theoretical studies indicate that there are regions of SUSY model parameters [8, 9, 10], including the region allowed by neutrino oscillation data [11, 12], where the decay mode for the light stop $\tilde{t}_1 \to \tau b$ is dominant one. However, there is also part of the parameters space that favors $\tilde{t}_1 \to eb$ and $\tilde{t}_1 \to \mu b$ decays over $\tilde{t}_1 \to \tau b$ [11, 12].

To provide as wide a search as possible and set limits in the most model-independent manner possible, we set upper limits on the cross section $\sigma(\tilde{t}_1\bar{\tilde{t}}_1) \times \beta^2$, neglecting additional decay modes that may pass selections of this analysis when $\beta \equiv \mathcal{B}(\tilde{t}_1 \to \tau b) < 1$. This has the advantage that we are not vulnerable to the particulars of the RPV coupling details. To set 95% confidence level limits (C.L.) on the stop mass $m(\tilde{t}_1)$, we assume that $\beta = 1$. Note that our procedure is conservative even if the contributions from other decay modes are not negligible as it will yield less stringent limits.

2. Stop Pair Production

Here we present the motivation for our choice of the stop pair production process. At the Fermilab Tevatron stop quarks and antiquarks can be produced in pairs in strong interactions ($gg/q\bar{q} \to \tilde{t}_1\bar{\tilde{t}}_1$). A single stop could also be produced at the Tevatron, e.g., via $bg \to \tilde{t}_1\tau$ [30]; however, unlike pair production, this process requires an RPV vertex. In regions of parameter space not excluded by data, $\not{R}_p$ couplings are small [5, 6], making single stop production negligible compared to pair production. Figure 1 shows the leading order (LO) Feynman diagrams that contribute to the stop pair production process. The contribution of the gluon-gluon fusion to the cross section (see Section IV.B for details) is smaller than that of $q\bar{q}$ annihilation, and it quickly decreases with stop mass: from $\sim 48\%$ at $m(\tilde{t}_1) = 100$ GeV/c^2 to $\sim 25\%$ at $m(\tilde{t}_1) = 150$ GeV/c^2. It also should be noted that there is one more diagram that contributes to the LO process: $t\bar{t} \to$ (t-channel gluino exchange) $\to \tilde{t}_1\bar{\tilde{t}}_1$. However, this diagram is strongly suppressed by the negligibly low contents of sea t-quarks in the PDFs and the high expected gluino mass.

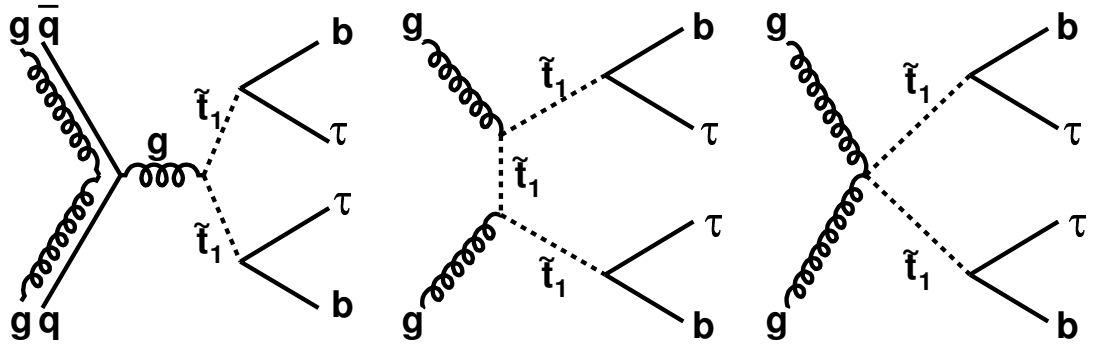

FIG. 1: Feynman diagrams for the stop pair production at the Tevatron. We assume that each of the stop quarks decay via R-parity violating coupling into b-quark and a τ.

D. Dissertation Outline

We next outline the reminder of the dissertation. Chapter II describes the experimental apparatus used in this study. Short descriptions are given for the Tevatron accelerator, the detector and data acquisition systems of the CDF II detector, and also for the infrastructure of the software used for simulation and for reconstruction of the data. In Chapter III we provide details on all our datasets and samples. Specifically, we present information about the lepton plus track triggers, which are used to collect the dataset for this study, and discuss the trigger efficiencies and their measurement. We also discuss the MC samples used to simulate the signal and background processes. Chapter IV describes the analysis methodology, signal event selection, as well as the background and systematic uncertainties estimation. Chapter V is about the procedure that we use to set the limits, the limit results themselves, the validation of the background estimation and the fit procedure, and some prospects and outlines for the future analysis. We conclude with Chapter VI with our final results. A number of Appendices are included to provide more technical details on such topics as

the tau and π^0 identification, measurement of tau ID efficiency, measurement of the efficiencies for the lepton plus track triggers, calculation of scale factors for $Z \to \tau\tau$ and $Z \to ll$ backgrounds, and interpretation of the results for third generation scalar leptoquarks. These details, while important, are given there so as to not interrupt the flow of the analysis description.

CHAPTER II

EXPERIMENTAL TOOLS

This chapter describes the main hardware and software tools that are important for this analysis: the Tevatron accelerator chain that produces and collides proton and antiproton beams (Section II.A), the CDF II detector and its subsystems (Section II.B), and the detector data acquisition and physics event reconstruction and simulation tools (Sections II.C and II.D).

A. The Tevatron Accelerator

The Tevatron is a superconducting proton-antiproton ($p\bar{p}$) accelerator located at the Fermi National Accelerator Laboratory (FNAL), also known as Fermilab. An aerial view if the Fermilab site is shown in Fig. 2 [31]. FNAL hosts a complex of accelerators and storage rings which supply protons and antiprotons to the two Tevatron collider experiments, CDF and DØ, as well as delivering beams to fixed target experiments.

Figure 3 shows a schematic drawing of Fermilab's accelerator chain. Hydrogen gas is used as a source for production of protons and antiprotons [32]. The gas is negatively ionized by a Haefely Cockcroft-Walton pre-accelerator (labeled PRE-ACC in Fig. 3), which collects the ions inside of its dome which is charged to a potential of -750 keV. The ions (H^-) are accelerated to energies of 750 keV through the column from the charged dome to the grounded wall before being injected in 40 μs-long segments into the Linac, a 150 m long linear accelerator, that raises ions' energy up to 400 MeV. Stripped of their electrons from passing a thin carbon film, the protons and are injected in 20 μs-long segments into the Booster, a circular accelerator or synchrotron with a radius of 75 m, which accelerates them to 8 GeV and gathers into bunches. The proton bunches are then transferred into the Main Injector (MI), a

FIG. 2: An aerial view of Fermilab [31].

bigger synchrotron with a radius of 525 m. To load the protons into the Tevatron, the MI accelerates 7 proton bunches to 150 GeV and combines them into a single bunch. For a 36×36 store this process is repeated 36 times.

To produce antiprotons, protons are accelerated by the MI to 120 GeV and directed to hit a nickel-copper target. Antiprotons produced during this collision are collected by an axis-symmetric electromagnetic lithium lens into a parallel beam. A pulsed dipole magnet is used to select 8 GeV antiprotons. Out of 10^5 proton collisions only one or two antiprotons are captured, and the rest is crashed into the beam dump. The momentum spread is diminished inside the Debuncher through the application of betatron (transverse) cooling and momentum (longitudinal) cooling. After cooling, antiprotons are temporarily stored in the Accumulator. When enough antiprotons have been collected, they are injected into the MI in 4 sets of 7 bunches. The MI

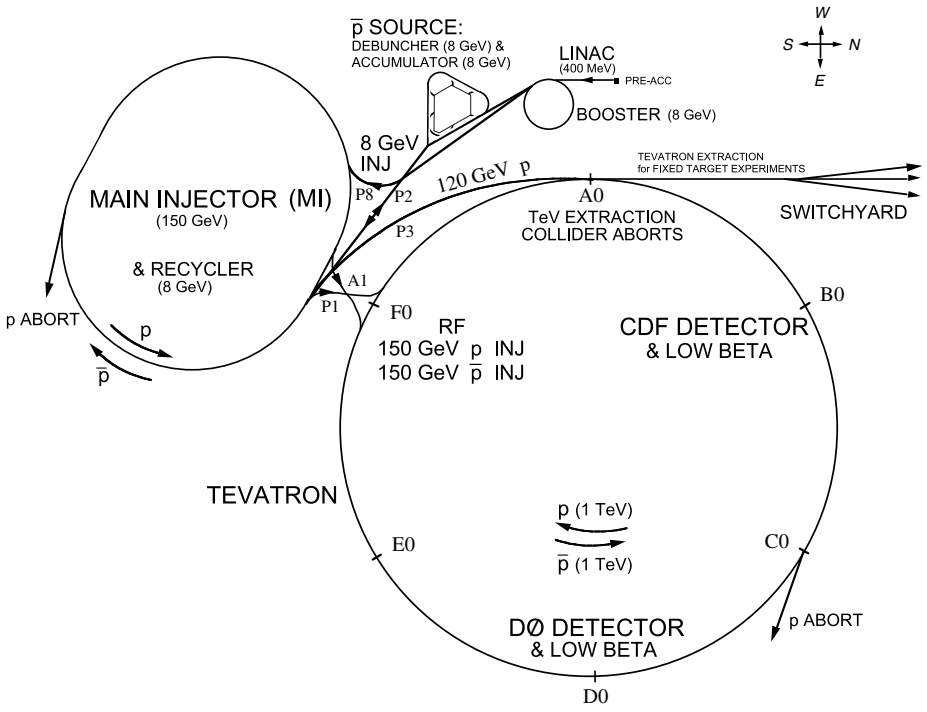

FIG. 3: A schematic drawing of Fermilab's accelerator chain [32].

accelerates them to 150 GeV and combines them into 4 bunches which are loaded into the Tevatron. The process is repeated nine times for a 36×36 store. If antiprotons are not sent to the Tevatron they may be stored in the Recycler, an 8 GeV antiproton storage ring located along the ceiling of the MI tunnel. When the Accumulator becomes full the rate of antiproton production decreases, and the Recycler provides an economical way to store antiprotons and to keep their production rate high. The Recycler was put into operation in 2003 and allowed a substantial increase in the Tevatron luminosity.

The final stage of acceleration is done inside the main Tevatron ring, a synchrotron with a radius of 1 km. It raises the energy of the 36 counter-rotating bunches of protons and antiprotons separated by 396 ns to 980 GeV. To confine beams to the synchrotron's path the Tevatron uses superconducting Ni/Ti alloy magnets that are

kept at 4.9 K and produce magnetic fields up to 4.5 Tesla. The proton and antiproton bunches counter-rotate without disturbing each other in electrostatically separated helical orbits. After acceleration the beams are typically kept inside the Tevatron from 10 to 25 hours. This is known as a "store". During a store, the beams are forced to cross at two points on the ring: B0 which is site for the CDF II detector and D0, the DØ detector site (see Fig. 3). This results in collisions of protons and antiprotons at a center-of-mass energy of 1.96 TeV.

The intensity of the beams is characterized by their luminosity. The typical initial luminosity during the time that the data for this analysis was collected was 8×10^{31} $\mathrm{cm}^{-2}\mathrm{s}^{-1}$. Luminosity is directly proportional to the product of numbers of protons and antiprotons per bunch and frequency of collisions, and inversely proportional to the product of the transverse x and y Gaussian averaged profiles of a bunch. Initially, there are about 24×10^{10} particles in each proton bunch and about 3×10^{10} in each antiproton bunch. The bunches lose particles with time due to various reasons, which results in decreasing luminosity as a function of time. When luminosity becomes too low, the store is ended. Figure 4 shows the total integrated luminosity delivered by the Tevatron and acquired by CDF as a function of the day of the year, given per year of Run II operation, for the time period when data used in this analysis were taken. One can see a continuous improvement in the performance of the Tevatron and high efficiency of CDF data taking.

B. The CDF II Detector

CDF II is a multipurpose detector designed for precision measurements of energy, momentum, and identification of particles produced in proton-antiproton collisions. The detector is described in Ref. [33] and Fig. 5 presents its isometric and elevation

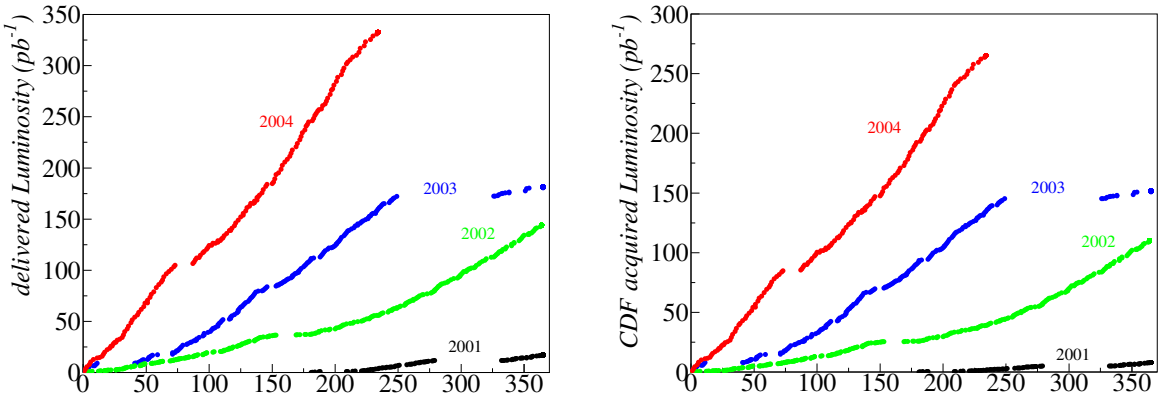

FIG. 4: Total integrated luminosity delivered (left) by the Tevatron and acquired (right) by CDF as a function of the day of the year, given per year of Run II operation.

views. Here we describe the detector elements directly related to this analysis. The CDF coordinate system is defined with respect to the proton beam direction, which defines the positive z direction, and the azimuthal angle ϕ is measured around the beam axis. The polar angle θ is measured with respect to the positive z direction. The pseudorapidity η is defined as $\eta = -\ln\tan\frac{\theta}{2}$. The transverse components of particle energy and momentum are conventionally defined as projections onto the plane transverse to the beam line, $E_T \equiv E\sin\theta$ and $p_T \equiv |\vec{p}|\sin\theta$.

The subdetectors critical to this analysis are the silicon vertex detector (SVX II), the central outer tracker (COT), the central parts of the calorimeter system, namely the central electromagnetic (CEM), with the shower maximum detector (CES) embedded inside the CEM, the central hadronic (CHA), and wall hadronic (WHA) calorimeters, and the central muon detection system located outside of the calorimeter with two subsystems: the central muon (CMUP, $|\eta| < 0.6$) and central muon system extension (CMX, $0.6 < |\eta| < 1.0$). The CMX system is new comparing to Run I and allows significant increase of muon coverage. Figure 5 depicts the detector with many of the important systems labeled. The CDF II detector has, except for

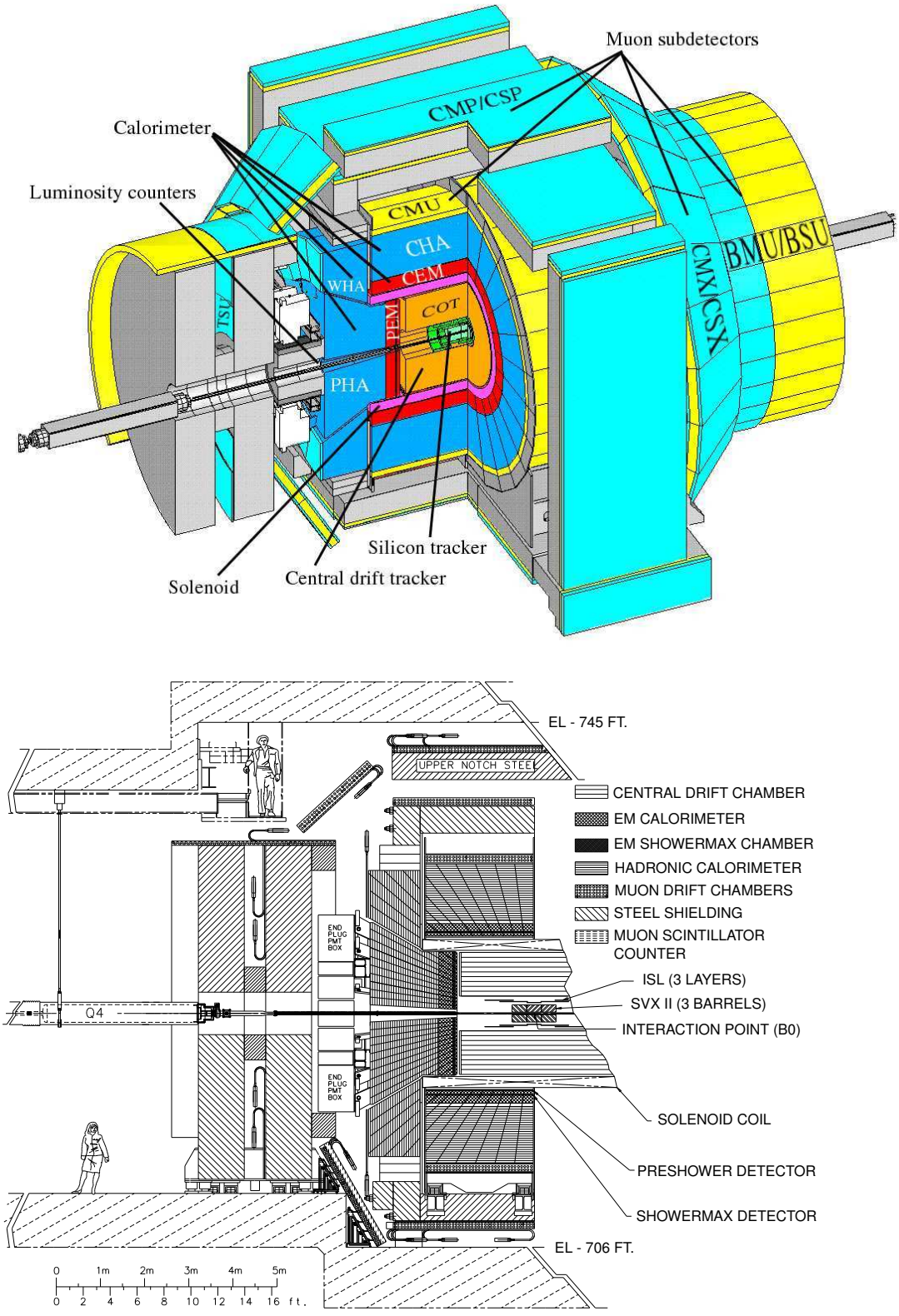

FIG. 5: An isometric [34] (top) and elevation [35] (bottom) views of the CDF II detector.

minor exceptions, forward-backward symmetry about the nominal interaction point and azimuthal symmetry about the beam line. The subdetectors are concentric, each covering as much solid angle as possible around the interaction point, and each with a roughly cylindrical geometry.

Figure 6 presents a schematic chart of different particles traversing successive detector components. Different patterns help to distinguish and identify the particles. The charges and momenta of charged particles can be measured from the curvature of the tracks as measured in the tracking chamber. Electrons and photons leave very similar pattern in the calorimeter (except that photons do not have tracks), and they deposit practically all of their energies in the electromagnetic calorimeter. Most of energy of hadrons is deposited in the hadronic calorimeter. Muons pass through and leave only traces of energy in all of the mentioned detectors, but also reach and deposit energy in the muon drift chambers. The CDF II detector was not designed for detecting neutrinos, however their presence is characterized by a net imbalance in the transverse energy deposition. Each detector element is described in detail in the following subsections.

1. The Tracking System

The innermost portion of the detector is the set of tracking detectors is to measure the momentum and charge of charged particles using their measured paths and curvatures in a magnetic field. Also they allow for the reconstruction of both the primary interaction vertex of an event and any secondary vertices due to decays of long-lived particles. The tracking system includes two detectors: the SVX II and the COT.

The SVX II is the component of the CDF II detector closest to the beam line. It provides a precise determination of the vertex position in the transverse plane via $r - \phi$ tracking as well as adding some improvement in resolution of momentum

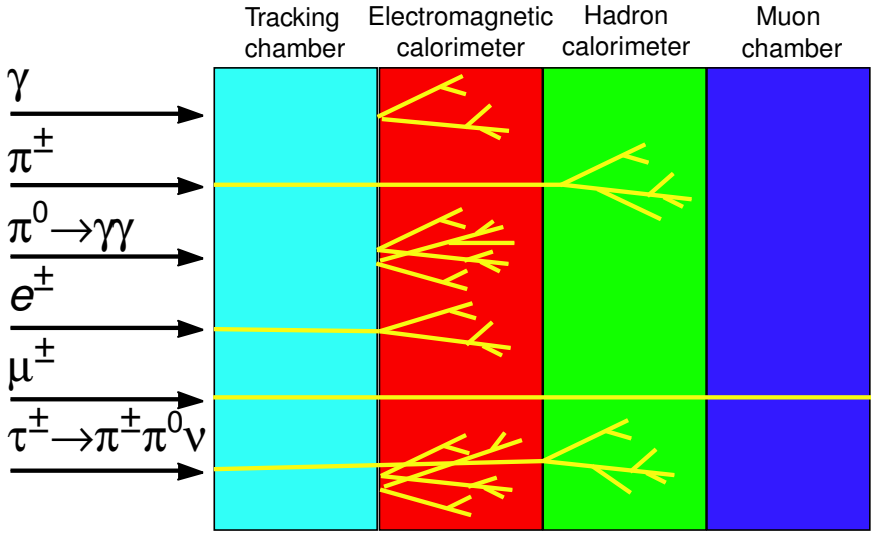

FIG. 6: Schematic chart that illustrates the interactions of various particles in the different detector components.

measured by the COT. There are three separate silicon microstrip subdetectors. At the smallest radius there is a single-sided silicon strip detector mounted on the beam pipe and called Layer 00 (L00) [36]. The original Silicon Vertex Detector (SVX) of Run I was replaced with the new SVX subsystem [37] in SVX II which has five layers of double-sided silicon arranged in 12 wedges of 15° between 2.44 and 10.6 cm radii. In the z-direction each layer is split into three 29 cm cylindrical "barrels" of 12 wedges each. The intermediate silicon layer (ISL) detector [38] surrounds the SVX II. It is 175 cm long and extends the tracking coverage to the region of $|\eta| < 1.9$. It is also structured into three barrels of twelve wedges each. The central barrel has one layer of silicon at a radius of 22 cm, and the outer barrels have two layers at 20 and 28 cm respectively. There are a total of 722,432 channels in the eight layers of SVX II and they provide full 3D standalone tracking of charged particles.

Just outside the SVX II is the central outer tracker. The COT is a cylindrical, 310 cm long [39], an open cell drift chamber covering the radii from 43.3 cm to 132.3

cm. The COT was upgraded in Run II to reconstruct charged particle trajectories in the region $|\eta| < 1$ for higher luminosities than in Run I. The COT is located inside a $B = 1.41$ T solenoidal magnetic field. The COT chamber is filled with 50-50 Argone-Ethane gas mixture with a small admixture of isopropyl alcohol and oxygen, which has maximum drift time of 100 ns (which is small comparing to the 396 ns bunch spacing). The chamber contains 96 layers of sense wires grouped into eight "superlayers" (4 axial and 4 stereo) of 12 wires each. In total there are 30,240 wires, each wire is 40 μm in diameter and made of gold-plated tungsten and run between two endplates. The superlayers alternate between purely axial wires and stereo wires tilted by 3° with respect to the beam line. The two different kinds of layers allow particle trajectories to be reconstructed in 3D. Each superlayer is divided in ϕ into cells with 12 wires each, and each making 35° angle with respect to radial lines from the z-axis. The number of cells increases from 168 for the first superlayer to 480 at the eighth one to maintain the same wire density with increasing radius.

2. The Calorimeters

The calorimeters are located outside of the tracking volume and serve to measure the energies of the particles. Electrons and photons lose energy mainly through the process of electromagnetic showering that consists of cycles of bremsstrahlung and pair production, and is characterized by the radiation length, X_0 as the average distance a particle must travel in order for $1/e$ of its original energy to remain. The electromagnetic shower reaches its maximal profile at 4-7 of X_0. Hadrons lose their energy through inelastic nuclear interactions, forming hadronic cascades in material. The nuclear interaction length, λ_I, is much longer than X_0 due to the small interaction cross section. So hadrons deposit most of their energy in the hadronic caloriometers. Muons lose only small amount of their energy in either calorimeters mostly due to

ionization.

The CDF II detector uses scintillator-based sampling calorimeters which measure energy proportional to the total number of particles created in an electromagnetic shower or hadronic cascade. The sampling calorimeters have sandwich-like structure with layers of absorber, lead or iron, and active layers of scintillator. The light produced by charged particles in the scintillator is collected by photo-multipliers, with their output being proportional to the total energy.

The CDF calorimeters cover the region $|\eta| < 3.6$. It consists of the following subsystems: central electromagnetic (CEM), with the shower maximum detector (CES) embedded inside the CEM, central hadronic (CHA), wall hadronic (WHA), plug electromagnetic (PEM), and plug hadronic (PHA) calorimeters. Figure 5 illustrates the geometric positioning of these detectors. The calorimeters are segmented into projective geometry[1] "towers".

The CEM [40] is a lead-scintillator calorimeter, while the CHA and WHA [41] consist of alternating iron and scintillator sheets. The CEM, CHA, and WHA have complete azimuthal coverage, with pseudorapidity $|\eta| < 1.1$ for the CEM and $|\eta| < 1.3$ for the CHA+WHA. The segmentation of all three detectors is determined by the size of the individual towers, each covering 15° in ϕ and $\simeq 0.1$ unit in η. The thickness of CEM is about $18X_0$ or $1\lambda_I$, while CHA and WHA are $4.7\lambda_I$ and $4.5\lambda_I$ thick respectively. The CEM and CHA single particle energy resolutions, $\delta E_T/E_T$, are[2] $0.14/\sqrt{E_T} \oplus 0.02$ and $0.5/\sqrt{E}$, respectively, where E_T is the transverse energy in GeV. The WHA energy resolution is $0.75/\sqrt{E_T} \oplus 0.04$.

The shower maximum subdetector (CES) [40] is a set of strip/wire gas-filled

[1]The divisions between towers always point at the center of the detector.

[2]The number after $\oplus$ is the average uncertainty for individual tower calibrations.

chambers embedded inside the CEM calorimeter at a depth of $6X_0$ (at a radius of 184.15 cm), where the longitudinal density of the electromagnetic shower is expected to be maximal. In each half of the CDF II detector in z, and for each 15° section in ϕ, the CES is subdivided into two further segments in z. Each half has 128 cathode strips (69 in the lower z and 59 in the higher z segment) separated by ≈ 2 cm that measure the shower position along the z direction, with a gap of ± 6.2 cm at the $z = 0$ plane. In each such segment, 64 anode wires (grouped in pairs) with a 1.45 cm pitch provide a measurement of ϕ. EM showers generate signals in several adjacent strips and wires. The reconstruction algorithms can group adjacent hits and such a set of strip or wire hits is called a CES cluster. The centroid of the cluster defines the position of an electromagnetic shower in the plane perpendicular to the radial direction with a resolution of 2 mm in each direction. The information provided by the CES detector is used both in electron identification and selection and in identifying $\pi^0 \rightarrow \gamma\gamma$ candidates resulting from tau lepton decays.

The calorimetry in the end plugs ($1.0 < |\eta| < 3.6$) has a rather complicated tower geometry, but the 15° wedge pattern is maintained. The PEM [42] has lead absorber and scintillating tile read out with wavelength shifting fibers. The PHA uses iron absorbers. These systems have replaced the gas plug calorimeters which were used in Run I. The PEM and PHA are $23.2X_0$ ($1\lambda_I$) and $6.8\lambda_I$ thick respectively. The energy resolution for high-energy electrons and photons is $0.144/\sqrt{E} \oplus 0.007$ for the PEM and $0.68/\sqrt{E} \oplus 0.04$ for the PHA.

3. The Muon Detectors

Muon identification is performed by 4 layers of single-wire proportional drift chamber. The chambers are filled with a 50-50 mixture of Argon-Ethane gas at atmospheric pressure, and have maximal drift times near 1 μs. There are three muon subdetectors

used in this analysis: the central muon detector (CMU), the central muon upgrade (CMP), and the central muon extension (CMX). The muons that pass the CMU and CMP are referred to as CMUP muons. The systems provide a resolution of about 0.2-0.6 mm in $r-\phi$ direction and about 10 cm in z-direction with nearly 100% hit efficiency.

The CMU [43] is located directly behind the hadronic calorimeter at radius 347 cm in a limited portion of the central region ($|\eta| < 0.6$). It consists of 144 modules of 16 rectangular drift cells. Each module has four radial layers of four cells running in the z-direction. The modules are arranged into two cylindrical 226 cm long barrels centered around the beam axis and connected[3] at $z = 0$.

The CMP adds additional coverage in the central region and reduces background with an additional 30-70 cm of steel shielding, corresponding to 4 pion interaction lengths. It is mounted on horizontal/vertical planes that are parallel to the beam line and are at a distance 5-6 m away from it. The drift chambers are aligned along the z-axis and are arranged into four layers, with each consecutive layer being offset by half. Outside of the CMP there are tiles of scintillators (CPS) that are used for triggering by providing a signal for muon information to be read out into trigger. This is necessary due to slow drift time of muon chambers.

The CMX covers the region $0.6 < |\eta| < 1.0$, except for a 30° gap located at the top of the detector. It is shaped as two truncated cones around the beam line (see Fig. 5). The radus of the cones is aproximately between 4 and 6 m and they are positioned between 3.5 to 5 m in $|z|$. The cones are made of eight physical layers of drift tubes, with the average muon passing through six. In order to create a truncated cones out of rectangular cells, the cells overlap at the narrow end of the cone and have

[3]There is an 18 cm gap due to the central calorimeter arch support.

no overlap at the wide end. The inside and the outside of the cones is covered with tiles of scintillators (CSX) to facilitate triggering.

C. Online Tools: The Trigger and Data Acquisition Systems

Collisions occur at the center of the CDF detector every 396 ns. The challenging task performed by the trigger and data acquisition (DAQ) system is to select, to monitor the quality, and to store useful physics events from interactions happening at the rate of 7.6 MHz. Figure 7 [35] presents the data flow diagram through the CDF II trigger and DAQ system. The necessary rejection rate is roughly 10^6:1, as only about 100 events per second can be written to tape with an average logging rate of $\sim$ 23 MB/s. For this purpose the CDF II has a three-level trigger system, which we will refer to as L1, L2, and L3. The first two levels consist of special-purpose custom built hardware, allowing for a gradual reduction of the event rate to $<$ 50 kHz at L1 and down to 300 Hz at L2. At L1 and L2 the event data is separated into many pieces corresponding to the different detector subsystems. After L2 accepts an event, the data from all the detector systems is combined into a single event data record by the event builder [44]. Level 3 is a farm of "commodity" computers running Linux that filters the datastream coming from the event builder to about 100 events per second and sends them for data storage. The system is designed so that the operation results in a minimal or no loss of important data (no dead time).

At each level there are a number of different trigger paths that correspond to triggering on different physics signals. The relevant trigger pathes for this analysis are lepton+track trigger pathes that are designed to select events with a central electron or muon and an isolated track. We will discuss the lepton+track triggers and physics behind them in details in Section III.A. Here we will only describe the basic elements

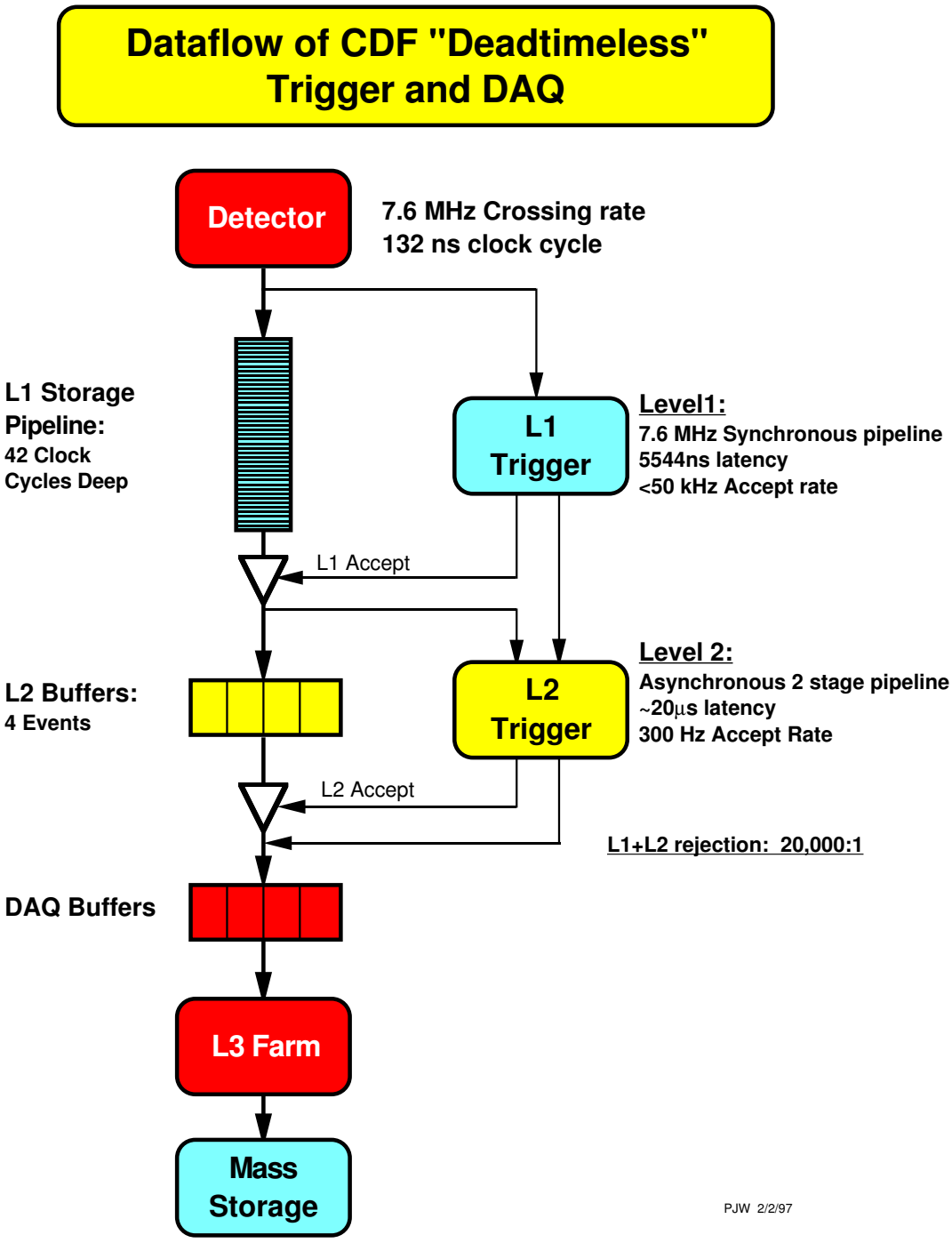

FIG. 7: Data flow diagram for the deadtimeless trigger and DAQ system at CDF [35].

of the trigger system that are important for us.

Level 1 picks up events from the 42-cell pipeline for storing events from every beam crossing and performs some simple hardware based reconstruction. The time it takes for L1 to analyze an event is $\sim$ 4 μs. At L1, the eXtremely Fast Track (XFT) trigger [45] reconstructs tracks in the COT, based on the hit information from axial COT superlayers only. There are two stages of the track reconstruction: the track segments are reconstructed in each superlayer; the segments are linked into a single track by comparing sets of track segments with predefined patterns. A track is reported by the XFT if 3 or 4 segments were successfully linked. Depending on the configuration, the track segment may be reconstructed with 10 to 12 hits. In the first year of Run II the XFT configuration was set to require 10 out of 12 hits (the "2-miss" XFT configuration). The increased luminosity and COT hit occupancy resulted in an increased XFT fake rate, thus the XFT was reconfigured to require 11 out of 12 hits (the "1-miss" configuration). If there are multiple XFT track candidates within one ϕ-slice ($\Delta\phi = 1.25^o$) at superlayer 6, only the track with the highest p_T is reported to L1.

In addition to this simple tracking information, L1 has access to the energy measurements for the calorimeter "trigger towers", defined as groups of two physical towers adjacent in η. This tower segmentation is used only in the trigger at L1 and L2; in all other parts of the text the term "tower" always refers to a physical tower unless specified otherwise. The L1 trigger performs spatial matching between an extrapolation of the track trajectories into the calorimeter in the $r-\phi$ plane. The muon triggering at L1 is based on the muon primitives [35] which are created using an etrapolation of the track position into the muon chambers. It is then linked to the muon chamber hits positions with a potential addition of CMP or CSX hits used for confirmation.

Both L1 and L2 have access to the measurement of missing transverse energy $\not\!\!E_T$ defined as $\not\!\!E_T = -\sum_i E_T^i \vec{n}_i$, where E_T^i is the magnitude of the transverse energy contained in trigger tower i, and $\vec{n}_i$ is the unit vector from the nominal interaction point to the tower in the plane transverse to the beam direction. Level 2 performs the same reconstruction algorithms as L1 but with greater accuracy and a longer decision time of $\sim$ 20 μs. It also performs clustering of energy in adjacent trigger towers, and has a better energy measurement due to increased bit count in the readout. In addition, the CES detector information is available for two fixed thresholds of the pulse readings in the CES system. Level 2 also matches the extrapolated track positions with calorimeter clusters and CES clusters.

Level 3 uses a simplified version of the offline reconstruction code (Section II.D), allowing further refinement of the selection. There are about 200 separate paths or combinations of L1&L2&L3 triggers that are implemented at Level 3. About 5% of the events that pass L3 are selected to monitor the quality of data taking and functionality of the detector systems in real time at the CDF control room.

D. Offline Software

The software used in high-energy physics serves many special purposes, but the main goal is to reduce and to interpret the experimental data. In order to do that, the software must provide a framework in which low level signals coming from various detectors can be used to reconstruct such high level objects as tracks, vertices, electrons, muons, taus, jets, etc. These high level objects are used to select events that exhibit patterns that might be due to some physics theory. A special case of data is Monte Carlo (MC) simulated data, which is used extensively to compare theoretical expectations and experimental observations. After a physics event is generated and

the detector response to it is simulated, the framework should be able to handle it almost as if it was a real event in detector. The following subsections provide details on the offline software and some of its algorithms for reconstruction and MC generation and simulation.

1. Reconstruction Software

The CDF II offline software is a large system designed using the "data flow" concept, when various modules consecutively process a stream of data [46]. It is mainly written in C++ and its event data format is largely based on input/output framework of ROOT system [47]. To produce most of high level object for analysis, the standard CDF executable called PRODUCTION runs a series of modules that apply various reconstruction algorithms to raw detector data[4]. Those objects are: tracks, vertices, electrons, muons, jets and π^0's. However, to reconstruct tau lepton hadronic decays we used a custom analysis level reconstruction[5]. Below we shortly describe the algorithms.

The charged particle tracks are reconstructed using helical pattern recognition algorithms applied to tracker hits: first, short stubs are formed from hits in the 12 layers in each superlayer, then the stubs are linked together to form tracks. A helix is defined by its curvature $C = q/2R$, where R is the radius of the helix x-y projection and q is the particle charge sign, beamline impact parameter d_0, and the following variables measured at the closest to the beamline point: z-coordinate z_0, azimuthal and polar angles ϕ_0 and $\lambda = \cot\theta$. The p_T of a track is determined by the helix

[4]Raw detector data are usually corrected by applying calibration tables that are kept in a relational database. Such corrections are necessary due to irregularities of detector response and due to misalignments. Most of calibrations have some specific update procedures in order to keep them up-to-date.

[5]Later our tau identification procedure was implemented as a standard one.

curvature as $p_T = \frac{eBc}{|2C|} \approx \frac{21\ \mathrm{GeV}/(c\cdot\mathrm{cm})}{|C|}$. The COT fully covers the region $|\eta| < 1$ providing momentum resolution $\delta p_T/p_T^2 \approx 0.0015\ c/\mathrm{GeV}$ and the efficiency about 99.6% for high-p_T electron and muon tracks [48]. Other parameters' resolutions are $\delta z_0 \approx 0.3$ cm, $\delta d_0 \approx 0.25$ mm, $\delta\phi_0 \approx 0.6$ mrad, and $\delta\lambda \approx 3$ mrad.

When the SVX II tracking information is available, the standalone silicon tracking provides the impact parameter resolution $\delta d_0 = 40\ \mu$m (including 30 μm contribution from the beamline), z-position resolution $\delta z_0 = 70\ \mu$m, and ϕ_0 resolution of 0.3 mrad. It is also possible to perform full 3D pattern recognition in COT and SVX separately, and then link them together in a fit in order to extract the best values of helix parameters. Such combined recognition improves the momentum resolution to $\delta p_T/p_T^2 \approx 0.0007\ c/\mathrm{GeV}$.

The first step in identifying an electron candidate is forming a clusters that combines up to two CEM towers adjacent in η. This is reasonable because electrons deposit their energy in a small region. And as they deposit almost all their energy in EM calorimeter, corresponding CHA towers should carry less then 0.125 of EM towers energy. The information about electron shower position and profile is determined at the point of the strongest showering at CES by fitting the shape position of CES clusters of 9 strips and nine wires. If such a calorimeter cluster could be matched to a track we get an electron candidate, and if no matching track could be found, a photon candidate is formed.

Muon candidate reconstruction begins with stub finding, with stubs being straight line patterns of hits in three or four layers of the muon chambers that are consistent with particle trajectories. Then stubs are linked together with tracks extrapolated into muon chambers. This analysis uses muon candidates that have both, CMU and CMP stubs, or just one CMX stub. Adding the amounts of energy deposited by a track passing through the calorimeter towers completes the information necessary to

form a muon candidate.

In this study we use jets reconstructed by the standard JETCLU algorithm by looking for clusters of energy in the calorimeter within a cone of radius $\Delta R \equiv \sqrt{\Delta\eta^2 + \Delta\phi^2} = 0.4$. Towers with $E_T > 1$ GeV are used as a seed for the jet search, then the nearby towers are added to the clusters until its radius is within $\Delta R \leq 0.4$. In order to avoid having towers that belong to more than one cluster, and additional step of splitting and merging is performed [49]. A series of correction are made to jet energies in order to best approximate the corresponding quark energies [50]. We apply so called "Level 5" corrections[6] which take into account relative detector response, multiple interactions and energy loss in the uninstrumented regions of the calorimeter.

The net imbalance in the transverse energy deposition defines a quantity called missing transverse energy ($\not\!\!E_T$ or MET), which is often interpreted as neutrino energy. The uncorrected MET is the magnitude of $\vec{\not\!\!E}_T^{\,\mathrm{raw}} \equiv -\sum E_T^i \, \hat{n}_i$, where $\hat{n}_i$ is the unit vector in the transverse plane pointing from the interaction point to the energy deposition in calorimeter cell i. $\not\!\!E_T$ is $\not\!\!E_T^{\,\mathrm{raw}}$ further corrected for the muon p_T and for the effects of non-ideal response of the calorimeter to e, τ, and jets (see Section IV.C.6.d for details). $\not\!\!E_T$ is typically used as a scalar, in which case it refers to the magnitude of the vector defined above. Studies in minimum bias events gave an estimate of the MET resolution at $0.4 \times \sqrt{\sum E_T}$, where $\sum E_T$ is the scalar sum of the transverse energy of towers in the calorimeters.

The detailed description of the τ_{h} and π^0 identification algorithms and variables could be found in Appendix A.A and Ref. [51]. Here we will only outline major definitions that are necessary to describe our analysis. The τ_{h} candidate is defined

[6] We use version jetCorr04b of the JetUser package.

by a narrow cluster of calorimeter towers associated with one or more tracks and zero or more π^0 candidates. The tracks contributing to a $\tau_{\rm h}$ candidate must satisfy the following requirements: the highest p_T track ("seed track") is required to have $p_T > 6$ GeV/c; the other tracks must have $p_T > 1$ GeV/c and be within a tau track signal cone with an opening angle

$$\alpha_{\rm trk} = min[0.17, max(5\ {\rm GeV}/E_{\rm clu}, 0.05)] \tag{2.1}$$

around the seed track. We reconstruct π^0 candidates by looking at narrow strip and wire clusters in the CES [51]. The contributing π^0 candidates are required to have $E_T > 1$ GeV and to be within a π^0 signal cone of $\alpha_{\pi_0} = 0.17$ rad with respect to the seed track. The track and π^0 isolation regions are defined as annuli between the respective signal cones and the cone of 0.52 rad around the seed track. We define the tau tracking isolation as number of tracks with $p_T > 1$ GeV/c in the track isolation region, and the π^0 isolation is defined as sum of the transverse energies of the π^0 candidates in the π^0 isolation region. The $\tau_{\rm h}$ candidate visible 4−momentum is defined as

$$p^\tau \equiv \sum_{\delta\theta<\alpha_{\rm trk}} p^{\rm trk} + \sum_{\delta\theta<\alpha_{\pi^0}} p^{\pi^0}\ , \tag{2.2}$$

where $\sum p^{\rm trk}$ and $\sum p^{\pi^0}$ are the sums of momenta of tracks and π^0 candidates in their respective signal cones.

2. Monte Carlo Event Simulation

This study relies heavily on the use of Monte Carlo event generation which is followed by full detector simulation and event reconstruction. Due to the complexity of the detector system, MC methods provide the only possible way to accurately model the observables for the stop pair production predictions. We are also dependent on

MC predictions for most of the background processes. A full generation-simulation-reconstruction chain is fulfilled by the standard at CDF set of executables called MC Production [52]. We used the official CDF Electroweak group MC Production tarball made with the offline CDF software version 5.3.3.

The MC Production runs first one of MC event generators which use theoretical cross section formulae, random number generation, initial and final state radiation and hadronization mechanisms, and special particle decayer packages to produce possible outcomes of physics processes. The result for each generated event is a list of particles that would enter the detector volume including their kinematics and relation to the primary collision particles. We use PYTHIA [53] version 6.216 as a MC generator, as it reliably describes the $p\bar{p}\rightarrow\tilde{t}_1\tilde{t}_1$ production, QCD radiation and hadronization. It is based on leading order matrix elements followed by coherent parton shower eveluation and hadronization to simulate gluon radiation and fragmentation. For proper handling of the τ lepton and b quark decays we use TAUOLA v2.6 [54] and QQ v9.1b [55] correspondingly. We do that because PYTHIA has limited implementation for decays of these particles. In the generation we use CTEQ5L [56] for the parton distribution functions (PDFs) and the renormalization scale, Q, is given by $Q = \sqrt{m(\tilde{t}_1)^2 + p_T(\tilde{t}_1)^2}$. For each run a number of events proportional to the run integrated luminosity was generated. Effects of the instantaneous luminosity are taken into account by adding extra minimum bias events [52], which are also generated using PYTHIA.

Further, an event undergoes the GEANT3-based [57] CDF II full detector simulation. The detector parametrization used for this purpose is measured in real data corresponding to the data taking period used in this analysis. Before entering the actual detector simulation simulation, each primary vertex is placed in a particular space-time point following a (Gaussian) distribution with run-dependent parameters.

The GEANT3-based simulation performs the following tasks: step-by-step particle propagation through the detector medium following a detailed geometrical representation of CDF II, creation of detector hits (digitization) using particle position and energy loss in each step, and particle-to-hit association. The results of this procedure are finally converted into the raw data format that is the same as coming from the real detectors and data.

CHAPTER III

DATASETS AND MONTE CARLO SAMPLES

The datasets used in this analysis were collected by the lepton plus track triggers [58]. These triggers select events that contain electron (or muon) and an isolated track, that requires isolation in its 10°-30°annulus. If tau decays hadronically, it would very likely pass such an isolated track requirement. Thus, the triggers provide data samples enriched with the electron (muon) plus an hadronically decaying tau signature. The minimum $p_T$requirements for the "lepton" and the "track" legs are 8 and 5 GeV/c correspondingly.

The dataset contains 322 ± 19 pb^{-1} of data taken by CDF between March 2002 and August 2004. The standard of 6% on the integrated luminosity is taken from Ref. [59]. For this analysis we select physics runs that have fully functioning detector systems that are relevant to this analysis. For this purpose we use the run list conventionally named at CDF as "good run list," and we use its 7th version. As we do not use b-tagging for this study, we do not require good silicon tracking system during runs in this list. However, we do require fully functioning electron and muon detector systems. It should be noted that the CMX system started its operation in August 2002, so we ignore bad CMX system indication for runs <150145. It makes the luminosity obtained by the CMX muon plus track trigger path 18 pb^{-1} less than for the other triggers.

Signal samples for the study were obtained using PYTHIA [53] with the GEANT3-based [57] CDF II detector simulation. Estimation of the backgrounds was performed using MC simulated samples as well as the same lepton plus track triggers dataset. Further in this chapter we provide more details on the lepton plus track triggers, their efficiencies and the samples for the analysis.

A. Lepton Plus Track Triggers and Datasets

The lepton plus track triggers in the CDF Run II were designed to be sensitive to events with two medium-p_T leptons, including events where one of the leptons is an hadronically decaying tau ($\tau_{\rm h}$). The "lepton" leg of the triggers corresponds to electron or muon candidate, that might originate from a real electron or muon, or a leptonically decaying tau (τ_l). Such triggers allow us to explore a large region of SUSY parameter space where we may expect taus in the final states. The improved tracking in CDF Run II that allowed to use tracking information in L1 triggers served as another motivation (see Section II.C).

The original design and detailed studies for these triggers are presented in Refs. [60] and [61]. The evolution of the triggers since their implementation as well as possible physics topics that might benefit from use of the triggers are discussed in Ref. [62].

The lepton plus track triggers include three trigger paths: electron plus track, CMUP muon plus track, and CMX muon plus track. Each of the three pathes of lepton plus track triggers has specific requirements at each level which are given in Tables III, IV, and V for electron plus track, CMUP muon plus track, and CMX muon plus track correspondingly. Since their installation in January 2002, the triggers experienced several minor modifications which were necessary in order to adjust better to the existing running conditions [62]. The requirements presented in here are for the later runs in the dataset.

TABLE III: Requirements for the electron plus track (TAU_ELECTRON8_TRACK5_ISO) trigger path.

Trigger Name	Requirements
Level 1	
L1_CEM8_PT8	• electron side: seed tower $E_T \geq 8$ GeV in central; $E^{\rm had}/E^{\rm em} \leq 0.125$; "4 layer" or "3 layer" XFT $p_T \geq 8.34$ GeV/c; pointing to the seed tower;
Level 2	
L2_CEM8_PT8_CES3_&_TRK5_DPHI10	• electron side: cluster seed $E_T \geq 8$ GeV in central, shoulder $E_T \geq 5$ GeV; $E^{\rm had}/E^{\rm em} \leq 0.125$; "4 layer" XFT $p_T \geq 8.34$ GeV/c pointing to the seed; CES $E \geq 3$ GeV; • isolated track side: second "4 layer" XFT $p_T \geq 5.18$ GeV/c; • other requirements: the angle between 1st and 2nd XFT is $\geq 10°$;
Level 3	
L3_ELECTRON8_TRACK5_ISO	• electron side: $E_T \geq 8$ GeV (calculated with track z_0); $p_T \geq 8$ GeV/c; $\chi^2_{strip} \leq 20$; $\lvert\Delta z_{\rm CES}\rvert \leq 8$ cm; • isolated track side: $p_T \geq 5$ GeV/c; $\lvert\eta\rvert \leq 1.5$; no track with $p_T > 1.5$ GeV/c and $\lvert\Delta z_0\rvert < 15$ cm in $0.175 \leq \Delta R \leq 0.524$; • other requirements: $\lvert z_0(e) - z_0({\rm trk})\rvert \leq 15$ cm; $\Delta R(e, {\rm trk}) \geq 0.175$.

TABLE IV: Requirements for the CMUP muon plus track (TAU_CMUP8_TRACK5_ISO) trigger path.

Trigger Name	Requirements
Level 1	
L1_CMUP6_PT4	CMU stub $p_T \geq 6$ GeV/c; number of CMP hit layers > 2; "4 layer" associated XFT $p_T \geq 4.09$ GeV/c;
Level 2	
L2_CMUP6_PT8	"4 layer" XFT $p_T \geq 8.34$ GeV/c;
Level 3	
L3_CMUP8_TRACK5_ISO	• muon side: $p_T \geq 8$ GeV/c; $\lvert\Delta x_{\rm CMU}\rvert < 15$ cm; $\lvert\Delta x_{\rm CMP}\rvert < 20$ cm; • isolated track side: $p_T \geq 5$ GeV/c; $\lvert\eta\rvert \leq 1.5$; no track with $p_T > 1.5$ GeV/c and $\lvert\Delta z_0\rvert < 15$ cm in $0.175 \leq \Delta\Theta \leq 0.524$; • other requirements: $\lvert z_0(\mu) - z_0(\mathrm{trk})\rvert \leq 15$ cm; $\Delta R(\mu, \mathrm{trk}) \geq 0.175$.

Figure 8 illustrates the reduction of the cross section for each trigger path at each trigger level, comparing to the cross section values for inelastic scattering, $Z \rightarrow \ell\ell$ (where ℓ is e, μ or τ), and stop pair production with $m(\tilde{t}_1) = 100$ GeV/c^2. It shows the effectiveness of the triggers in reducing the amount of data necessary for a relevant physics analysis.

B. Lepton Plus Track Trigger Efficiencies

The lepton plus track triggers are very efficient in selecting events with an electron/muon candidate and an isolated track in the final state. The trigger algorithms are simpler and are optimized not only for efficiency but also for speed, datastream

TABLE V: Requirements for the CMX muon plus track (TAU_CMUP8_TRACK5_ISO) trigger path.

Trigger Name	Requirements
Level 1	
L1_CMX6_PT8_CSX	CMX stub $p_T \geq 6$ GeV/c; "4 layer" associated XFT $p_T \geq 8.34$ GeV/c; require CSX;
Level 2	
L2_AUTO_L1_CMX6_PT8_CSX	auto accept;
Level 3	
L3_CMX8_TRACK5_ISO	• muon side: $p_T \geq 8$ GeV/c; $\lvert\Delta x_{\rm CMX}\rvert < 30$ cm; • isolated track side: $p_T \geq 5$ GeV/c; $\lvert\eta\rvert \leq 1.5$; no track with $p_T > 1.5$ GeV/c and $\lvert\Delta z_0\rvert < 15$ cm in $0.175 \leq \Delta\Theta \leq 0.524$; • other requirements: $\lvert z_0(\mu) - z_0(\mathrm{trk})\rvert \leq 15$ cm; $\Delta R(\mu, \mathrm{trk}) \geq 0.175$.

capacity, and degree of data reduction. Thus, the main sources of inefficiency are L1 and L2 triggers, which utilize low level detector data to perform simple but fast reconstruction.

We parametrize the trigger efficiencies as functions of p_T and other trigger parameters. We use the parametrized trigger efficiencies for MC samples for signal and backgrounds. Then we convolute them with MC in order to calculate average trigger efficiency. Trigger efficiencies for the lepton+track triggers were measured for each of the two legs separately using data taken over the same running period as the one used in this measurement. The details of the measurements are presented in Appendix B. Here we give a brief summary.

Efficiency for the electron leg is calculated using a sample of conversion electrons

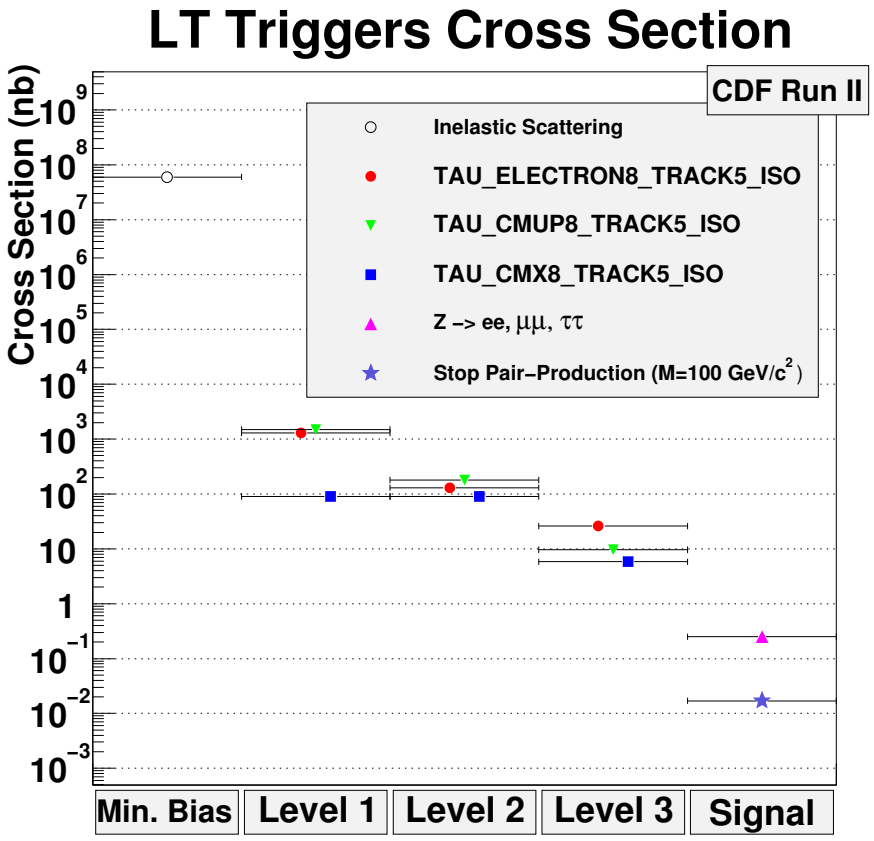

FIG. 8: The reduction of the cross section for each trigger path at each trigger level, comparing to the cross section values for inelastic scattering, $Z \to \ell\ell$ (where ℓ is e, μ or τ), and stop pair production with $m(\tilde{t}_1) = 100$ GeV/c^2.

reconstructed in jet and muon data and is described in detail in Appendix B.B and Refs. [63, 64]. Efficiency of the muon leg in the muon+track trigger was measured using $Z \to \mu\mu$ and Υ events as a function of muon track p_T and associated track p_T, see Appendix B.C and Refs. [65, 66]. Average plateau efficiency for the muon leg is found to be approximately 95%. For the "track" leg, the measurement of the trigger efficiency (see Appendices B.A and Refs. [67, 68]) is made in assumption that this leg is a hadronic tau and the efficiency is parametrized as a function of several tau variables. In the course of measuring efficiencies, we verified that the trigger efficiencies for the two legs are independent, e.g., we compared efficiency for events

with a single tau candidate and for events with tau candidate and an additional loose lepton. Average efficiency for the track leg above 10 GeV/c is approximately 96%, and it shows slow continuous growth towards higher p_T. We attribute this tendency to special features in the XFT track finding algorithm as discussed in Ref. [67].

C. Monte Carlo Signal Samples

In order to simulate and reconstruct signal events $p\bar{p}\rightarrow\tilde{t}_1\tilde{t}_1$ we use run dependent MC production [52]. The details of generation and simulation were described earlier in Section II.D.2. The full event reconstruction procedure was explained in Section II.D.1. Here we just mention that PYTHIA [53] version 6.216 is a MC generator of choice, and it uses CTEQ5L [56] for PDFs and $Q = \sqrt{m(\tilde{t}_1)^2 + p_T(\tilde{t}_1)^2}$ for the renormalization scale. The full CDF II detector simulation is based on GEANT3 package [57].

For each of the $\tilde{t}_1$ mass point (100, 110, ... 170 GeV/c^2) we generate a sample of 1 event per nb^{-1} (about 70k events per sample).

D. Data and MC Samples for Background Estimations

Here we only list the samples that we use for the background studies. For general discussion of the backgrounds see Section IV.E.

To estimate the contribution of Drell-Yan backgrounds, $Z/\gamma^* \rightarrow \tau_l\tau_{\rm h}$ and $Z/\gamma^* \rightarrow ll$ we use the official MC samples, which were produced with the same MC production tarball as our signal samples. However, it should be noted that we use data to correct Drell-Yan backgrounds for deficiencies in kinematics of Z boson production simulation in MC. In Appendix C we present detailed discussion about it. For the $t\bar{t}$ and diboson productions we use the official samples provided by the CDF Top group. All the samples we produced using PYTHIA as MC generator. For the reference purpose, the

following list shows the CDF MC dataset names for the mentioned samples:

- $Z/\gamma^* \rightarrow \tau_l\tau_{\rm h}$: `zewk8t`;
- $Z/\gamma^* \rightarrow ee$: `zewkae`;
- $Z/\gamma^* \rightarrow \mu\mu$: `zewk6m`;
- inclusive $t\bar{t}$: `ttop0z`;
- WW: `wtop1w`.

Our estimate of the QCD background contribution is data based, using the lepton plus track dataset with non-isolated lepton, as it is described in Section IV.E.4.

CHAPTER IV

EVENT ANALYSIS

A. Overview and Analysis Methodology

To every data sample we apply a set of selection criteria that are optimized to enhance the separation of signal events from events that belong to background process. If after such a selection we would see in the end a significant excess of number of events observed in data over our background expectations, that would be a sign of stop discovery. However, if no significant excess would be observed, we may set an upper 95% C.L. on stop pair production cross section times β^2, which we define as $\beta \equiv \mathcal{B}(\tilde{t}_1 \to \tau b)$.

Our analysis technique is similar to a 'blind' analysis technique and avoids any bias in the results. After selecting a quality lepton (electron or muon), a hadronic tau candidates and applying additional cuts to suppress backgrounds, we divide events into several regions (see Section IV.A.3 for details) using number of jets separated from lepton and tau and transverse mass of lepton and transverse missing energy. The region with two or more jets and low transverse mass contains most of the signal and relatively low fraction of the background. We do not look at the data in this region until all the selection criteria for signal events and estimation of the signal event acceptance and the backgrounds were finalized in each region.

It should be noted that during the limit calculation we use signal events not only from the signal region. That allows us to obtain a better limit.

1. Analysis Procedure

The event selection has the following steps:

1) preselection[1]: applying filers for "good run list"(see Chapter III), possible special HEPG event selection, and filter for removing possible duplicate events;

2) selection of a reconstructed electron or muon and a hadronic tau candidates that have specific kinematic requirements and are within fiducial volume of the detector (Section IV.C.1);

3) improving quality of the lepton and hadronic tau candidates by applying standard sets of identification cuts (Sections IV.C.2 and IV.C.3);

4) further improving the selection quality by requiring leptons to be isolated from tracks and jets (Section IV.C.4);

5) applying parametrized trigger efficiencies to Monte Carlo events (Section IV.C.5);

6) additional event level requirements in order to suppress and separate backgrounds (Section IV.C.6) and to sort events out into different side-band and control regions (Section IV.A.3).

This procedure was implemented using the Stntuple package from CDFSOFT2. Stntuple provides an extended ROOT ntuple format with a corresponding infrastructure that provides tools for developing an analysis code.

The event selection procedure is performed for all our datasets and samples. As it was mentioned in previous Section, in order to avoid biasing our results we do not look at data in the signal region until our selection is optimized and validated. After the selection and estimation of backgrounds is finalized, we open the signal region for data events.

[1]Note that for MC samples the number of events that are left after the preselection is considered as a baseline number to calculate the acceptances.

For statistical interpretation of the data, we developed a likelihood method that, in addition to our primary signal region, utilizes side-band regions (Section IV.A.3), which are used to perform data-driven background estimations and to improve the sensitivity of the analysis. The result of such statistical interpretation is the likelihood which might be used either to set upper 95% C.L. limits on $\sigma(\tilde{t}_1\bar{\tilde{t}}_1)\times\beta^2$. or to measure the value of $\sigma(\tilde{t}_1\bar{\tilde{t}}_1)\times\beta^2$ in case of an observed data excess in the signal region.

2. Signal and Background Properties Overview

In this Section we mention the properties of signal events that distinguish them from background events and give a short overview of SM processes that are important backgrounds for this study. The detailed description of the background estimation procedures is given in Section IV.E.

Most of signal events are expected to have two or more energetic jets that originate from decays of b quarks. Also signal events tend to have low transverse mass of lepton and $\not\!\!E_T$, which is defined as

$$m_T(l,\not\!\!E_T) = \sqrt{2\times {p_T}^l \not\!\!E_T \times (1-\cos\Delta\Theta)}. \tag{4.1}$$

It should be noted that for electron one should use its measured E_T instead of the track p_T, as it provides more accurate number for a true electron energy. Another variable that helps in separation of sinal events from background is the scalar sum of lepton, tau and missing energy

$$Y_T(l,\tau_{\rm h},\not\!\!E_T) \equiv p_T(l) + p_T(\tau_{\rm h}) + \not\!\!E_T. \tag{4.2}$$

Note again that we use E_T instead of p_T for electron.

Major backgrounds for this search are Drell-Yan $Z\to\tau\tau$ and $Z\to ll$ events. The $Z\to\tau_l\tau_{\rm h}+\geq 2$ jets process has similar signature as our RPV stop pair production.

As for the $Z \rightarrow ll+ \geq 2$ jets processes, one of the leptons might be misidentified as tau candidate. The fraction of events with two or more extra jets is small for Drell-Yan processes, so the requirement of $N_{\rm jet} \geq 2$ with ${E_T}^{\rm cor} > 20$ GeV effectively separates signal from Drell-Yan backgrounds. The value of jet energy threshold was optimized for better limit setting (see Section IV.C.6.e). Also typical values of Y_T in Drell-Yan events are usually smaller than those in signal events.

The minor backgrounds include $t\bar{t}$, $W+$jets, QCD multijet, and diboson production events. The $t\bar{t}$ pair production also provides a similar signature as our signal, however it has smaller than Drell-Yan with two or more jets cross section. The $t\bar{t}$ events also tend to have high m_T values. Diboson production include WW, WZ, and ZZ pair production. They have very small cross section, and they contribute very little to our analysis. In QCD multijet events, e.g., semileptonic b quark decays or γ conversions can be misidentified as lepton signal candidates, and narrow jets can be misidentified as tau candidates. We use isolation requirements applied to the lepton and tau candidates and minimal Y_T cut to discriminate this background. The $W+$jets events find their way into our sample via their jet being misidentified as a tau candidate. These events typically have large m_T which helps to separate them from signal.

3. Signal, Side-Band and Control Region Definitions

As it was discussed in Section IV.A.2, signal events tend to have small m_T and two or more extra jets. We define signal region as $m_T < 35$ GeV/c^2 and $N_{\rm jet} \geq 2$. The value of $m_T < 35$ GeV/c^2 was not specifically optimized, but it separates the $W+$jets background very effectively. We use m_T and $N_{\rm jet}$ to define side-band and control regions. Table VI illustrates the definition of six regions in the m_T versus $N_{\rm jet}$ plane with the dominant contribution indicated for each region. Regions A, B, C and D are

used in setting final limit, regions A′ and B′ are used as control regions. We also use lower than default 110 GeV value of Y_T cut, $Y_T \geq 80$ GeV, to consider all the regions except A for control and validation purposes.

TABLE VI: Definition of six regions in the m_T versus $N_{\rm jet}$ plane with the dominant contribution indicated for each region. Regions A, B, C and D are used in setting final limit, regions A′ and B′ are used as control regions.

	$m_T < 35$	$m_T > 35$
$N_{\rm jet} \geq 2$	A ($\simeq$60% of signal, Drell-Yan)	B ($\simeq$40% of signal, W+jets, $t\bar{t}$)
$N_{\rm jet} = 1$	A′(Drell-Yan)	B′ (W+jets)
$N_{\rm jet} = 0$	C (Drell-Yan)	D (W+jets)

B. Stop Pair Production Cross Section and Its Uncertainty

As it was mentioned in Section I.C.2, at the Fermilab Tevatron stop quarks and antiquarks can be produced in pairs and Figure 1 shows the LO Feynman diagrams that contribute to the stop pair production process. To estimate the next-to-leading (NLO) cross section of stop pair production we use PROSPINO version 2 [69], our nominal choice of CTEQ6.1M PDFs [70], and a renormalization scale of $Q = \sqrt{m(\tilde{t}_1)^2 + p_T(\tilde{t}_1)^2}$. The expected cross section dependence on $m(\tilde{t}_1)$ is shown in Fig. 9, which presents the numerical values from Table VII.

There are two major sources for the systematic uncertainty on the theoretical prediction for the cross section. They are coming from the uncertainties on the choice of PDF and the choice of the renormalization and factorization scales. We analyzed the dependence of the theoretical cross section on choice of the PDF set by using

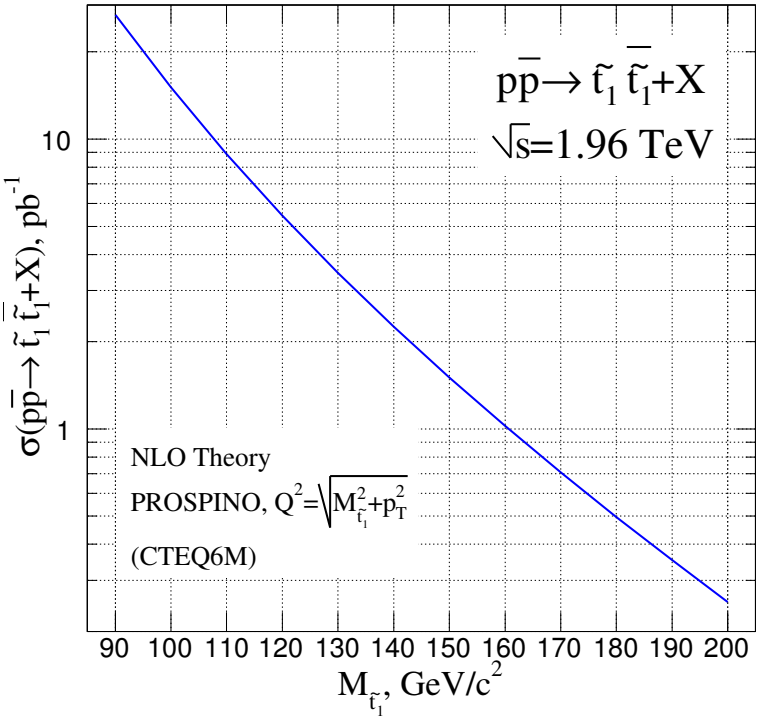

FIG. 9: The NLO cross section for the $p\bar{p} \to \tilde{t}_1\bar{\tilde{t}}_1$ process using CTEQ6M PDF set and with renormalization and factorization scales set to $\sqrt{m(\tilde{t}_1)^2 + p_T(\tilde{t}_1)^2}$.

the CTEQ6.1 infrastructure for the uncertainty estimation [70]. CTEQ6.1 provides a special "error" set of 20 uncertainty pairs. The set is based on $\pm 1\sigma$ deviations of a diagonalized set of 20 parameters which have their most likely values tuned using a global fit to experimental data. We calculate the cross section deviations from its most likely value obtained with the best-fit PDF for all 40 "error" PDFs. Following the special summation procedure described in details in [71], we combine these numbers in order to find the "+" and "−" uncertainties on the cross section due to the choice of PDF. We also studied the cross section dependence on a choice of the renormalization and factorization scales, by using a half and a double of the default values.

TABLE VII: Predictions for the stop pair production cross section (in pb) as a function of stop mass at NLO as calculated by the PROSPINO program [69]. Calculation is using CTEQ6M PDF set and renormalization and factorization scales are both set to $\sqrt{m(\tilde{t}_1)^2 + p_T(\tilde{t}_1)^2}$.

	$m(\tilde{t}_1)$[GeV/c^2]							
	100	110	120	130	140	150	160	170
$\sigma(p\bar{p}\to\tilde{t}_1\bar{\tilde{t}}_1)$ [pb]	15.1	8.89	5.44	3.45	2.25	1.50	1.023	0.708

We find that PDF uncertainties are surprisingly large[2] and are comparable to the effect due to variations in the scale. Table VIII provides details on the the uncertainty values for each case and stop mass. We combine both uncertainties into a single number by summing them in quadratures to obtain an ∼18% systematic uncertainty on the theoretical cross section. The details on how we use this uncertainty while calculating the stop cross section and mass limits could be found in Section V.C.

C. Signal Event Selection and the Acceptance

1. Geometric and Kinematic Acceptance for Leptons

a. Definitions

The geometrical and kinematical event acceptance is defined as a fraction of stop events satisfying the following requirements: an event has at least one reconstructed pair of lepton ($l = e$ or μ) and $\tau_{\rm h}$ candidates that satisfy kinematical and fiducial requirements as specified in Table IX and are separated by the requirement

[2]PDF uncertainty is an order of 10% mainly due to the "error" PDFs sets number 5 and number 15, which are related to the high x gluon fraction, which is rather poorly constrained.

TABLE VIII: Estimated theoretical uncertainties on the stop pair production cross section due to variations in the PDF and the choice of the renormalization and factorization scales.

Uncertainty	$m(\tilde{t}_1)[\mathrm{GeV}/c^2]$							
source:	100	110	120	130	140	150	160	170
	Uncertainty [%]							
PDF"+"	13.3	14.1	14.9	15.5	16.0	16.2	16.5	16.7
PDF"−"	−9.13	−9.8	−10.0	−10.3	−10.3	−10.4	−10.5	−10.2
$0.25Q^2$	13.1	12.1	11.3	10.6	10.0	9.5	9.1	9.0
$2Q^2$	−15.1	−14.7	−14.3	−14.1	−13.9	−13.8	−13.7	−13.5
Combined"+"	18.7	18.6	18.8	18.8	18.9	18.8	18.8	19.0
Combined"−"	−17.6	−17.7	−17.5	−17.5	−17.3	−17.2	−17.2	−17.0

$\Delta R(l, \tau_{\mathrm{h}}) > 0.7$. Note that these fiducial requirements ensure not only robust event reconstruction, but also high and well understood efficiency of triggering.

For the signal acceptance calculation we require that selected lepton and tau candidates are matched to generator level (HEPG) leptons in order to exclude mistags, e.g. when one of the jets is identified as a tau candidate. While after applying all the identification and selection cuts, these mistags are seen extremely rarely, at this stage mistagging happens rather often and therefore meaningful acceptance number requires matching of reconstructed objects to the generator level information.

b. Corrections and Systematic Uncertainties

The dominant sources for the corrections and systematic uncertainties in measurement of the geometrical and kinematical event acceptance are following: the track

TABLE IX: Geometrical and kinematical requirements for electron, muon, and tau.

Electron:	Muon:	Tau
CdfEmObject	CdfMuon	CdfTau
CEM	CMUP or CMX	
$E_T > 10$ GeV	$p_T > 10$ GeV/c	${p_T}^{\mathrm{seed-trk}} > 6$ GeV/c
$p_T > 8$ GeV/c		${p_T}^{\mathrm{vis}} > 15$ GeV/c
$\lvert\eta\rvert < 1.0$		$\lvert\eta^{\tau}_{\mathrm{det}}\rvert < 1.0$
$\lvert z_0^{e-\mathrm{trk}}\rvert < 60$ cm	$\lvert z_0^{\mu-\mathrm{trk}}\rvert < 60$ cm	
$\lvert z_{\mathrm{COT}}\rvert < 150$ cm	$\lvert z^{\mu-\mathrm{trk}}_{R=137}\rvert < 150$ cm	$\lvert z^{\tau-\mathrm{trk}}_{R=137}\rvert < 150$ cm
Ele SMX Fiducial = 1	Fiducial in CMUP or CMX	$9 < \lvert z^{\tau-\mathrm{trk}}_{R_{\mathrm{CES}}}\rvert < 230$ cm

reconstruction efficiency, the muon stub-finding efficiencies the and material uncertainty. The detailed discussion of most of them is presented in Ref. [51].

The track reconstruction efficiency was studied in $W \rightarrow e\nu$ events and it revealed no difference between data and MC, with an uncertainty of 0.4% per track. We assign this as a systematic uncertainty due to knowledge of the tracking reconstruction efficiency for the electron track and for the seed track in one-prong taus. The case of three-prong taus is somewhat different, because the additional tracks create higher occupancies that may have a larger effect on pattern recognition. We assign a systematic uncertainty in the knowledge of track reconstruction efficiency of 3% for the three-prong taus, making use of the results obtained in the CDF measurement of $D^{\pm}$ meson production [72]. The $D^{\pm}$ mesons have multiplicity and momentum distributions similar to those of the three-prong taus, making such comparisons valid. Note that the three-prong taus constitute about a third of the total used in the study, and

thus the average systematic uncertainty due to the track reconstruction efficiency in $e\tau_{\rm h}$ events must be weighted accordingly:

$$\epsilon^{\rm trk}_{e\tau_{\rm h}} \simeq 2/3 \times (\epsilon_e + \epsilon_{1-{\rm pr}}) + 1/3 \times \sqrt{(\epsilon_e^2 + \epsilon_{3-{\rm pr}}^2)} \simeq 1.4\% \ , \tag{4.3}$$

where $\epsilon_{1-{\rm pr}}$ and $\epsilon_{3-{\rm pr}}$ are track reconstruction efficiency uncertainties for one and three-prong taus, and ϵ_e is electron track reconstruction efficiency uncertainty. Note that this uncertainty is "per event" and not "per track."

For muon channels we do not consider the track reconstruction efficiency for muon leg separately, instead we use the results of Ref. [73] which are the scale factors to compensate for the difference in stub-finding efficiencies between data and MC: $f^{\rm CMUP} = 0.941 \pm 0.008$ and $f^{\rm CMX} = 0.987 \pm 0.003$, for the CMUP and CMX respectively. So, to find the average systematic uncertainty due to the track reconstruction efficiency in $\mu\tau_{\rm h}$ events we make use of Eq. (4.3) setting $\epsilon_e = 0$, which results in $\epsilon^{\rm trk}_{\mu\tau_{\rm h}} \simeq 1.2\%$.

The MC prediction for the efficiency of the $|z_0^{\rm e-trk}| < 60$ cm cut is checked by comparing its efficiency in minimum bias $p\bar{p}$ collision data to the MC prediction. No deviation is found and the statistical accuracy of this comparison, 0.3%, is assigned as a systematic uncertainty.

The uncertainty due to the imprecise knowledge of the amount of material in the detector is estimated by comparing the default acceptance to that measured with the case where the amount of material in the detector simulation is shifted. The comparison leads to about a 0.4% effect. For the $\mu\tau$ channel, without the impact of bremsstrahlung that exists for the electron channel, the effect of material uncertainty can be neglected. The effects of difference due to calorimeter scale calibration in data and MC turned out to be negligible compared to the leading effects.

We also performed a study [74] of the effect of a cut on the maximum number of

TABLE X: The scale factors and systematic uncertainties in measurement of the geometrical and kinematical event acceptance.

Channel	CEM	CMUP	CMX
Effect	Multiplicative Correction		
Track Reconstruction	1.000 ± 0.014	1.000 ± 0.012	1.000 ± 0.012
Stub Reconstruction	1.0	0.941 ± 0.008	0.987 ± 0.003
$\|z_0\| < 60$ cm	1.000 ± 0.003	1.000 ± 0.003	1.000 ± 0.003
Material Uncertainty	1.000 ± 0.004	1.0	1.0
Scale factor	1.000 ± 0.015	0.941 ± 0.015	1.000 ± 0.013

towers N_{tow} in a tau cluster, which is set to six. A significant difference between data and MC due to this effect might be expected due to the deficiencies in the simulation of the lateral profile of a hadronic shower in the calorimeter. However, our study have shown that the corresponding systematic uncertainty due to this effect is negligible.

Table X shows the combination of correction factors and associated uncertainties.

c. Results

The geometrical and kinematical event acceptance depends on the mass of the stop. Table XI shows the break down of efficiencies of the requirements for signal events with $m(\tilde{t}_1) = 150$ GeV/c^2. In Table XII we present the summary of acceptance calculations for each of the generated stop mass points.

2. Electron and Muon Identification and Efficiency

Table XIII shows the efficiency for electron at each stage of the identification cuts. We assign a scale factor of 1.00 with a systematic uncertainty of 0.5%, as suggested by recent data and MC comparisons [75]. Note that this scale factor is fully applicable for events with electron $E_T > 20$ GeV, while about 25% of stop events have electrons with lower E_T. To correct for this, we use results of Ref. [76], where the low E_T electron

TABLE XI: Kinematical and geometrical acceptance for the case of $m(\tilde{t}_1) = 150$ GeV/c^2. Note that reconstructed objects (CdfElectron, CdfMuon or CdfTau for e, μ or $\tau_{\rm h}$ candidates correspondingly) are required to match to a corresponding HEPG particle. Fiduciality requirement includes XFT fiduciality and CES or CMUP/CMX fiduciality.

$e + \tau$		$\mu^{\rm CMUP} + \tau$		$\mu^{\rm CMX} + \tau$	
Electron:	Efficiency (%)	Muon:	Efficiency (%)	Muon:	Efficiency (%)
CdfElectron	73.9 ± 0.2	CdfMuon:	68.8 ± 0.2		68.8 ± 0.2
η	84.5 ± 0.2	CMUP	38.2 ± 0.2	CMX	18.7 ± 0.2
E_T	77.7 ± 0.2				
p_T	94.1 ± 0.1	p_T	83.0 ± 0.3	p_T	78.3 ± 0.4
z_0	97.0 ± 0.1	z_0	96.7 ± 0.1	z_0	97.3 ± 0.2
Fiducial	84.2 ± 0.2	Fiducial	97.8 ± 0.1	Fiducial	67.7 ± 0.5
Total	37.3 ± 0.2		23.8 ± 0.2		7.67 ± 0.10
Tau:					
CdfTau(*)	66.3 ± 0.3		66.3 ± 0.4		65.3 ± 0.7
η	87.5 ± 0.3		87.8 ± 0.3		87.5 ± 0.6
E_T	95.2 ± 0.2		95.2 ± 0.2		95.2 ± 0.4
Seed p_T	97.5 ± 0.1		97.6 ± 0.2		98.2 ± 0.3
Fiducial	90.6 ± 0.2		89.6 ± 0.3		90.5 ± 0.6
Total	48.8 ± 0.3		48.5 ± 0.4		48.3 ± 0.7
$\Delta R(e, \tau)$	96.7 ± 0.2		96.1 ± 0.2		97.3 ± 0.3
α	17.6 ± 0.1		11.06 ± 0.12		3.61 ± 0.07
Scale Factor	1.000 ± 0.015		0.941 ± 0.015		0.987 ± 0.013
Final α	$17.6 \pm 0.1 \pm 0.3$		$10.41 \pm 0.11 \pm 0.17$		$3.56 \pm 0.07 \pm 0.05$

ID scale factor was determined to be 1.000 ± 0.025. Weighting the two numbers, we obtain an average systematic uncertainty of approximately 1%. Note that isolations are not included in the lepton ID and are considered separately (see Section IV.C.4).

To improve purity of the signal, a set of muon identification cuts is applied. We use nearly standard cuts (e.g. see Ref. [73]), as nearly 75% of our signal muons have p_T >20 GeV/c. The full list of cuts and corresponding MC efficiency can be found in Table XIV.

We estimate the efficiency of the muon identification cuts using MC for events

TABLE XII: Acceptance for $\tilde{t}_1\bar{\tilde{t}}_1 \to b\bar{b}\tau_l\tau_h$ as a function of stop quark mass. Acceptance values quoted at this point are not corrected for the known differences in stub finding efficiency between data and MC.

	$m(\tilde{t}_1)$ [GeV/c^2]				
	100	110	120	130	140
α^{CEM}	11.15 ± 0.12	12.61 ± 0.12	14.12 ± 0.13	15.36 ± 0.14	16.60 ± 0.14
α^{CMUP}	7.28 ± 0.10	7.96 ± 0.10	8.97 ± 0.11	9.71 ± 0.11	10.06 ± 0.12
α^{CMX}	2.58 ± 0.06	2.84 ± 0.06	3.16 ± 0.06	3.28 ± 0.07	3.60 ± 0.07
	150	160	170		
α^{CEM}	17.59 ± 0.14	18.59 ± 0.15	19.45 ± 0.15		
α^{CMUP}	11.07 ± 0.12	11.89 ± 0.12	12.10 ± 0.13		
α^{CMX}	3.61 ± 0.07	3.77 ± 0.07	4.18 ± 0.08		

passing the acceptance cuts and scale the efficiency using scale factors from [73]. Note that we total additional systematics of 3% for CMUP, as our $\Delta x_{\mathrm{CMU}} < 4$ cm is different to the standard one ($\Delta x_{\mathrm{CMU}} < 3$ cm), and this cut is mainly responsible for the differences between data and MC. We used Fig. 14 of Ref. [77] to estimate the difference in the scale factor due to difference in cuts and find that it to be at the level of 1%. Combining with a scale factor uncertainty from Ref. [73] and re-weighting the uncertainty to account for about 25% of events in the lower p_T region (below 20 GeV/c), we conclude that the 3% uncertainty that we use is very conservative. We do not require presence of the primary vertex, so the beam (x, y) position is used to correct the measured track impact parameter.

TABLE XIII: Efficiency of electron identification cuts using stop MC sample with $m(\tilde{t}_1) = 150$ GeV/c^2. We apply a scale factor from Ref. [75].

	Efficiency [%]
Track Quality	99.8 ± 0.1
$E^{\text{had}}/E^{\text{em}} < 0.055 + 0.00045 \times E$	97.9 ± 0.1
$E/p < 2.0$ (for $p_T < 50$ GeV)	92.1 ± 0.2
$-3.0 < Q_{\text{trk}} \cdot \Delta x < 1.5$ cm	98.9 ± 0.1
$\lvert\Delta z\rvert < 3$ cm	99.6 ± 0.1
$\chi^2_{\text{strip}} < 10$	96.8 ± 0.2
$L_{\text{shr}} < 0.2$	97.9 ± 0.1
$\lvert d_0\rvert < 0.2$ cm	99.6 ± 0.1
Cumulative	83.8 ± 0.3
Scale Factor	1.00 ± 0.01
Final Efficiency(*)	$83.8 \pm 0.4 \pm 0.9$

3. Tau Identification and Efficiency

We apply the same hadronic tau ID cuts as in the $Z \to \tau\tau$ cross section measurement, except for the different tau tracking isolation. This modification is necessary because stop events have significantly more activity due to hard jets in the event, which becomes a dominant issue in the efficiency of the isolation cut. In this measurement we estimate the efficiency using MC and correct it using the same scale factors except for the isolation cut. The dominant background in this analysis is $Z \to \tau\tau$ and not QCD. This motivates us to loosen the isolation requirement: instead of using the p_T sum of tracks in the isolation cone, we fall back to original requirement of no

TABLE XIV: Efficiency of muon ID cuts for CMUP and CMX muons for $\tilde{t}_1\bar{\tilde{t}}_1 \to b\bar{b}\tau_\mu\tau_{\rm h}$ for the case $m(\tilde{t}_1) = 150$ GeV/c^2. We use MC efficiency as a default. We quote alternative efficiencies obtained either directly from data or via MC-to-data comparisons as explained in the text. For all other cuts we use MC and apply scale factors from Ref. [73], and assign additional systematics of 3% for CMUP taking into account differences between our cuts and the cuts used in Ref. [73].

	CMUP	CMX
Track Quality	99.9 ± 0.1	99.9 ± 0.1
$E^{\rm em} < 2$, $E^{\rm had} < 6$ GeV	93.5 ± 0.3	93.8 ± 0.5
$\lvert d_0\rvert < 0.2$ cm	99.9 ± 0.1	99.9 ± 0.1
$\Delta x_{\rm CMU} < 4$ and $\Delta x_{\rm CMP} < 7$		
or $\Delta x_{\rm CMX} < 6$ cm	97.8 ± 0.2	98.0 ± 0.3
Cumulative	91.3 ± 0.3	91.9 ± 0.6
Scale Factor	0.939 ± 0.030	0.990 ± 0.003
Final Efficiency(*)	$84.9 \pm 0.3 \pm 3.7$	$91.0 \pm 0.6 \pm 0.3$

tracks with $p_T > 1$ GeV/c in the isolation cone. However, in this analysis procedure we chose to separate the isolation cuts from identification, and the issues related to isolation are discussed later in Section IV.C.4. Full list of cuts and their efficiencies can be found in Table XV. The scale factor of 1.00 ± 0.03 resulted from our study [74] and we provide some details on how it was obtained in Appendix A.B.

4. Lepton Isolation Requirements and Efficiencies

We require that both lepton (e, μ) and tau candidates are isolated. The isolation requirement that we use contains two parts: jet isolation and tracking isolation. For the jet isolation part we require no jets in an annulus of $0.3 < \Delta R < 0.8$ around the

TABLE XV: Efficiency of tau ID cuts for $\tilde{t}_1\bar{\tilde{t}}_1 \rightarrow b\bar{b}\tau_l\tau_h$ for the case $m(\tilde{t}_1) = 150$ GeV/c^2. We assign a systematic uncertainty of 3% [74].

Requirement	Electron Channel	Muon Channel	
		CMUP	CMX
Seed Track Quality	99.4 ± 0.1	99.4 ± 0.1	99.2 ± 0.2
$\lvert z_0^{\tau-\text{seed}} - z_0^{e/\mu-\text{trk}}\rvert \leq 5$ cm	98.9 ± 0.1	98.8 ± 0.2	99.1 ± 0.2
$d_0^{\tau-\text{seed}} < 0.2$ cm	98.0 ± 0.2	97.6 ± 0.2	96.7 ± 0.4
$\xi > 0.1$	94.5 ± 0.3	94.4 ± 0.3	94.1 ± 0.6
$m^{\text{trk}} \leq 1.8$ GeV/c^2 & $m^{\text{trk}+\pi^0} \leq 2.5$ GeV/c^2	95.3 ± 0.1	95.6 ± 0.3	94.5 ± 0.6
$N_{\text{trk}}^{\tau\ \text{cone}} = 1$ or 3	86.7 ± 0.4	85.7 ± 0.5	85.0 ± 0.9
Cumulative	75.2 ± 0.5	74.0 ± 0.6	71.8 ± 1.1
Scale Factor	1.00 ± 0.03	1.00 ± 0.03	1.00 ± 0.03
Final Efficiency(*)	$75.2 \pm 0.5 \pm 2.2$	$74.0 \pm 0.6 \pm 2.2$	$71.8 \pm 1.1 \pm 2.2$

lepton or tau, and we use jets as defined in Table XVI.

The tracking isolation for an electron or muon candidate, which we denote as $I_{\text{trk}}^{\Delta R<0.4}$, is defined as the sum of p_T of all tracks around the lepton within $\Delta R < 0.4$, and we require $I_{\text{trk}}^{\Delta R<0.4} < 2$ GeV/c. Motivation for using the lepton-jet isolation is that the tracking isolation strongly depends on a presence of jets nearby: efficiency becomes very low if a jet happens to be near lepton. Figure 10 shows how average track isolation efficiency depends on ΔR to the closest jet compared to the efficiency for $Z \rightarrow \tau\tau$ events, in which jets are rarely present. Note that with a moderate cut of $\Delta R > 0.8$ efficiency in stop events becomes quite similar to the one in $Z \rightarrow \tau\tau$ events.

TABLE XVI: Jet definition used in this analysis. Jet ${E_T}^{\rm cor}$ threshold of 15 GeV is used for $\not\!\!E_T$ corrections and for lepton and tau jet isolation; the threshold of 20 GeV is optimized value used for extra jet counting.

$\lvert\eta^{\rm det}\rvert$	< 2.4
${E_T}^{\rm raw}$	> 10 GeV
${E_T}^{\rm cor}$	> 20 GeV (15 GeV)
$\Delta R(e/\mu/\tau_{\rm h}, {\rm jet})$	> 0.8

Remaining residual difference is small and is partially due to the jet thresholds (a jet with ${E_T}^{\rm cor} < 15$ GeV can happen to be near the lepton, but will not be considered as a "jet"). The lower bound in lepton-jet isolation is dictated by the fact that electron or tau will always be identified as a jet and therefore we always expect a jet somewhere within $\Delta R < 0.3$ around electron or tau. We keep the same definition for muons for consistency.

As a side note, we found that ISAJET MC predicts a noticeably different track isolation efficiency, which we attribute to deficiencies in the underlying event simulation. This problem is not new and was discussed in the Rick Field's underlying events studies [78].

With lepton-jet isolation applied, we estimate the track isolation efficiency using PYTHIA MC. We do not apply any scale factors as our previous studies in $Z \to \tau\tau$ have indicated a good agreement between data and MC.

Tor tau's tracking isolation we loosen the default isolation requirement: instead of using the p_T sum of tracks in the isolation cone, we fall back to original requirement of no tracks with $p_T > 1$ GeV/c in the isolation cone.

We separately studied the luminosity dependence and found it to be weak. Note

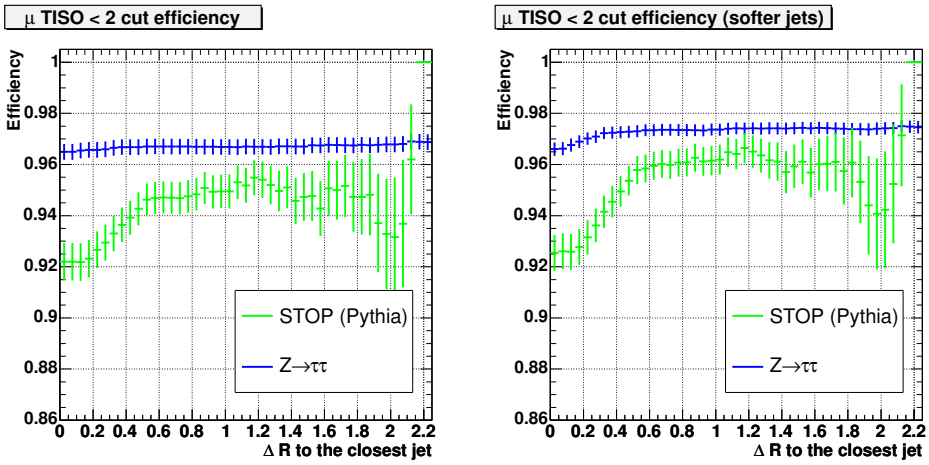

FIG. 10: a) Cumulative efficiency of the lepton track isolation as a function of ΔR, where ΔR is the cut value of minimal separation between jet and a lepton. We compare $Z \rightarrow \mu\mu$ and stop events after all other ID cuts applied. This plot shows that track isolation strongly depends on jet closeness; b) To amplify this effect, we plot the same distribution, but with a softer jet definition threshold (${E_T}^{\rm raw} > 6$, ${E_T}^{\rm cor} > 10$ GeV). This plot shows even better agreement between track isolation efficiencies in Z and stop samples for events with applied jet isolation $\Delta R > 0.8$.

that lepton-jet isolation is much less dependent on the instantaneous luminosity due to a relatively stiff requirement that the jet has to have energy above 15 GeV.

Table XVII shows the efficiency of isolation cuts for $m(\tilde{t}_1) = 150$ GeV/c^2. We assign a 3% overall systematic uncertainty that well covers difference between isolation in $Z \rightarrow ll$ and stop events and also small differences between $Z \rightarrow ll$ data and MC.

5. Trigger Efficiencies

For the detailed discussions of the efficiencies for the lepton plus track triggers, please see Section III.B and Appendix B. Here we only present the results for average trigger efficiencies in Table XVIII. These numbers were obtained by convoluting the parametrized trigger efficiencies with our MC samples of $Z \rightarrow \tau\tau$ and signal events.

TABLE XVII: Efficiency of isolation requirements for $\tilde{t}_1\bar{\tilde{t}}_1 \rightarrow b\bar{b}\tau_l\tau_h$ for the case $m(\tilde{t}_1) = 150$ GeV/c^2. We assign the systematic uncertainty of 3% for these cuts.

Requirement	Electron Channel	Muon Channel	
		CMUP	CMX
Lepton:			
Jet Separation	89.4 ± 0.3	87.9 ± 0.4	88.9 ± 0.7
$I_{\rm trk}^{\Delta R<0.4} < 2.0$ GeV/c	87.7 ± 0.3	92.6 ± 0.3	93.6 ± 0.6
Tau:			
Jet Separation	93.4 ± 0.3	94.0 ± 0.4	94.2 ± 0.7
$N_{\rm trk}^{\tau,\,\Delta\Theta} = 0$ & $N_{\rm trk}^{\tau,\,\Delta R} = 0$	78.6 ± 0.5	78.9 ± 0.7	78.4 ± 1.2
$I_{\pi^0}^{\tau,\,\Delta\Theta} \leq 0.6$ GeV/c	95.5 ± 0.3	95.7 ± 0.4	95.7 ± 0.7
Scale Factor	1.00 ± 0.03	1.00 ± 0.03	1.00 ± 0.03

6. Additional Requirements and Their Efficiencies

We then apply several additional event level requirements to reduce remaining backgrounds.

a. Conversion Electron Removal

This is applicable to the electron channel only. We remove events, in which primary electron candidate is likely produced by a photon conversion. Definition of a conversion candidate is given in Table XIX.

TABLE XVIII: Average trigger efficiency for $Z \rightarrow \tau_l \tau_{\rm h}$ and $\tilde{t}_1\bar{\tilde{t}}_1 \rightarrow b\bar{b}\tau_l\tau_{\rm h}$ for the case $m(\tilde{t}_1) = 150$ GeV/c^2.

Trigger	$Z \rightarrow \tau\tau$	$\tilde{t}_1\bar{\tilde{t}}_1 \rightarrow b\bar{b}\tau\tau$
CEM $\epsilon^e_{L1} \times \epsilon^e_{L2} \times \epsilon^e_{L3}$	$96.0 \pm 0.1 \pm 1.0$	$97.6 \pm 0.2 \pm 1.0$
CMUP$\epsilon^\mu_{L1} \times \epsilon^\mu_{L2} \times \epsilon^\mu_{L3}$	$95.8 \pm 0.1 \pm 1.0$	$95.8 \pm 0.3 \pm 1.0$
CMX $\epsilon^\mu_{L1} \times \epsilon^\mu_{L2} \times \epsilon^\mu_{L3}$	$94.7 \pm 0.3 \pm 1.0$	$94.6 \pm 0.5 \pm 1.0$
TAU $\epsilon^\tau_{L1} \times \epsilon^\tau_{L2} \times \epsilon^\tau_{L3}$	$95.3 \pm 0.2 \pm 1.0$	$96.4 \pm 0.3 \pm 1.0$

TABLE XIX: Requirements for a pair of tracks to be tagged as a conversion. S_{xy} is defined as the distance between the two track trajectory helices at the point of their closest approach to each other.

$\lvert\Delta(\cot\theta)\rvert \leq 0.04$
$\Delta S_{xy} \leq 0.2$

b. Cosmic Ray Removal

Cosmic removal is applicable to the muon channel. Sometimes, cosmic ray will pass through the detector and shower in the calorimeter producing an event topology similar to a single muon and a one prong tau candidate. It may even overlap with some activity in the calorimeter, e.g. a jet event. However, we find that such occurrences happen at a completely negligible rate due to the tight selection criteria, e.g. Δz matching, Y_T cut, jet thresholds incompatible with a soft minimum bias event etc. We use results of the standard Cosmic Ray Tagger [79] to reject such events. The only sizable presence of this background is expected in the $N_{\rm jet} = 0$ bin.

c. Drell-Yan Removal

We remove events with likely $Z \rightarrow \mu\mu$ or $Z \rightarrow ee$ candidates defined as shown in Table XX. Note that in the electron channels we use both calorimeter- and tau-based veto. In the tau-based veto case, to minimize effect on the signal, we additionally require that $\Delta\phi(e,\tau) > 2.9$.

TABLE XX: $Z \rightarrow \mu\mu$ and $Z \rightarrow ee$ veto definition.

$Z \rightarrow \mu\mu$	$Z \rightarrow ee$	
	Calorimeter-Based	Tau-Based
Second Track: Match to any stub $p_T \geq$10 GeV/c $\lvert z_0^{\rm trk} - z_0^{\mu}\rvert < 5$ cm Opposite charge $76 \leq m(\mu, \text{trk}) \leq 106$ GeV/c^2	Second CdfEmObject: $E_T > 8$ GeV $E^{\rm had}/E^{\rm em} < 0.12$ $76 < m(e, EmObj) < 106$ GeV/c^2	Tau: passes ID cuts $\Delta\phi(e,\tau) > 2.9$ rad $76 < m(e,\tau) < 106$ GeV/c^2

d. Missing Energy Corrections

After we have selected quality lepton and tau we perform corrections of missing energy which are done in three stages:

- corrections for the lepton (especially in muon case);
- adjusting $\not\!\!E_T$ due to jet energy corrections;
- tau related corrections.

To correct the components of $\not\!\!E_T$ vector due to energy lost with the muon we do the following:

$$(\not\!\!E_T{}^{\rm cor})_x = (\not\!\!E_T)_x - (p_T(\mu) - E_T{}^{\rm em+had}(\mu))\cos\phi(\mu), \tag{4.4}$$

$$(\not\!\!E_T{}^{\rm cor})_y = (\not\!\!E_T)_y - (p_T(\mu) - E_T{}^{\rm em+had}(\mu))\sin\phi(\mu). \tag{4.5}$$

The similar correction for the electron is as follows:

$$(\not\!\!E_T{}^{\rm cor})_x = (\not\!\!E_T)_x - (E_T(e))_x(f_{E_T}^{\rm cor}(e) - 1), \tag{4.6}$$

$$(\not\!\!E_T{}^{\rm cor})_y = (\not\!\!E_T)_y - (E_T(e))_y(f_{E_T}^{\rm cor}(e) - 1), \tag{4.7}$$

where $f_{E_T}^{\rm cor}(e)$ is a correction factor for electron transverse energy.

For the purpose of $\not\!\!E_T$ correction we use jets which are defined as in Table XVI with the only difference being lower jet energy threshold, $E_T{}^{\rm cor} > 15$ GeV. For such jets we perform the following transformation:

$$(\not\!\!E_T{}^{\rm cor})_x = (\not\!\!E_T)_x - \sum_{\rm jets}(p_T({\rm jet}))_x(f^{\rm cor}({\rm jet}) - 1), \tag{4.8}$$

$$(\not\!\!E_T{}^{\rm cor})_y = (\not\!\!E_T)_y - \sum_{\rm jets}(p_T({\rm jet}))_y(f^{\rm cor}({\rm jet}) - 1), \tag{4.9}$$

where $p_T({\rm jet})$ is uncorrected jet transverse momentum and $f^{\rm cor}({\rm jet})$ is "Level 5" correction factor for a jet.

Tau related correction is a bit more involved. The main part of it comes from the difference between tau cluster transverse momentum and tau transverse visible momentum $p_T{}^{\rm vis}(\tau)$, which was corrected in a way similar to Ref. [80]. Tau cluster towers which contribute to the default cluster momentum have threshold of E_T >1 GeV. However in data we can see noticeable leakage in the neighboring low E_T towers, which we found is not properly simulated in MC. To account for that, we calculate expanded tau cluster momentum $p_T{}^{\rm exp.\ cluster}(\tau)$, which additionally includes those adjacent low E_T towers, and use it in $\not\!\!E_T$ correction:

$$(\not\!\!E_T{}^{\rm cor})_x = (\not\!\!E_T)_x - (p_T{}^{\rm vis}(\tau) - p_T{}^{\rm exp.\ cluster}(\tau))_x, \tag{4.10}$$

$$(\not\!\!E_T{}^{\rm cor})_y = (\not\!\!E_T)_y - (p_T{}^{\rm vis}(\tau) - p_T{}^{\rm exp.\ cluster}(\tau))_y. \tag{4.11}$$

Note, that we correct $\not\!\!E_T$ only for the lepton or tau from the lepton-tau pair which we are considering.

The performance of the $\not\!\!E_T$ corrections on the example of stop events in $\mu\tau_{\rm h}$ channel with $m(\tilde{t}_1) = 150$ GeV/c^2 is illustrated in Fig. 11. Looking at the changes in "mean" and "sigma" of the fit we clearly see the improvement in $\not\!\!E_T$ resolution.

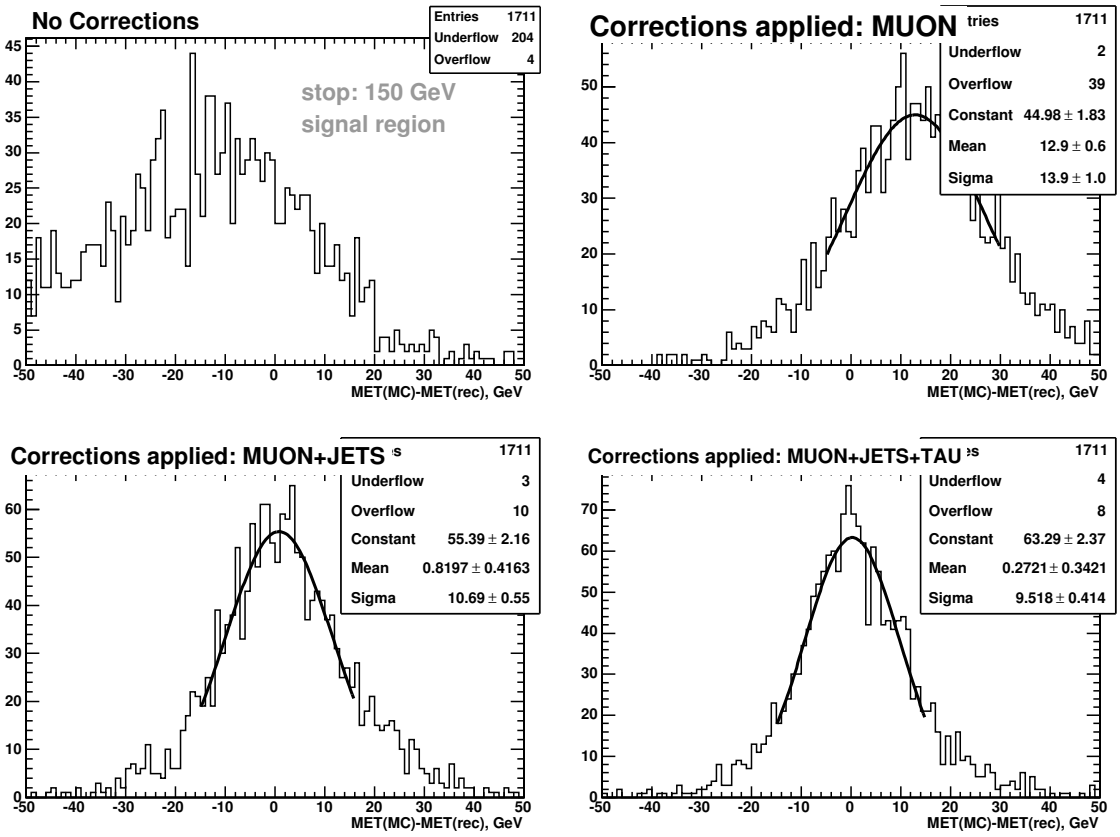

FIG. 11: Difference between HEPG calculated and reconstructed $\not\!\!E_T$ for different stages of $\not\!\!E_T$ correction (from left to right, from top to bottom): no correction; correction for muon was applied; corrections for muon and extra jets were applied; and corrections for muon, extra jets and tau were applied. For this example we used the $\mu\tau_{\rm h}$ sample of stop events with $m(\tilde{t}_1) = 150$ GeV/c^2.

e. Y_T Cut and Jet Energy Threshold Optimization

To suppress Z+jets and QCD backgrounds, we set a minimum on the scalar sum of lepton, tau and missing energy, denoted as Y_T (Eq.(4.2)). We optimize cut value for the Y_T variable for the best limit. In addition we optimize value of jet energy threshold for counting extra jets (see Table XVI and the next subsection). We checked that using simple $S/\sqrt{(S+B)}$ ratio gives similar result to more involved calculations using the *bayes.f* routine [81]. The resulting 2D plots of $S/\sqrt{(S+B)}$ ratio for different values of Y_T and jet energy cuts for the samples of 130 and 160 GeV/c^2 stop are shown in Fig. 12. Simpler plots depicting 1D slices of the previous 160 GeV/c^2 stop plot for a few values of Y_T and jet energy are presented in Fig. 13.

We chose optimized value of the cuts to be $Y_T \geq 110$ GeV and ${E_T}^{\rm cor} > 20$ GeV.

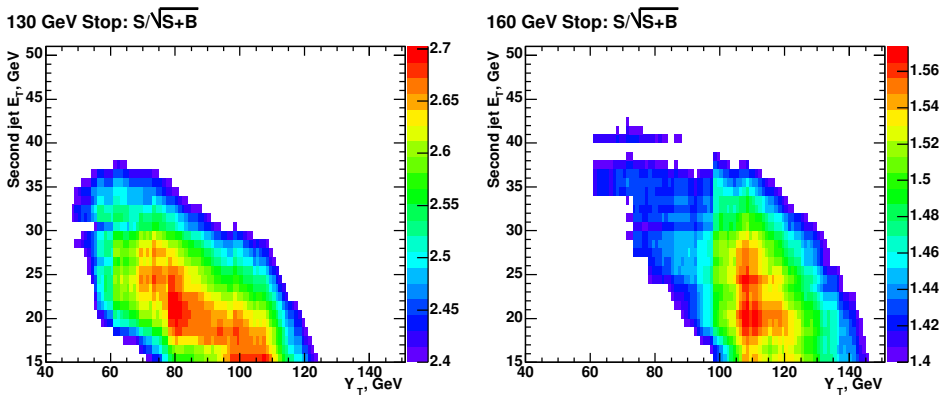

FIG. 12: $S/\sqrt{(S+B)}$ for different values of Y_T and jet energy cuts for the stop mass 130 (left) and 160 GeV/c^2 (right) samples. Electron and muon channels are combined together. Backgrounds include contributions of $Z \to \tau\tau$, $Z \to ll$ and $t\bar{t}$.

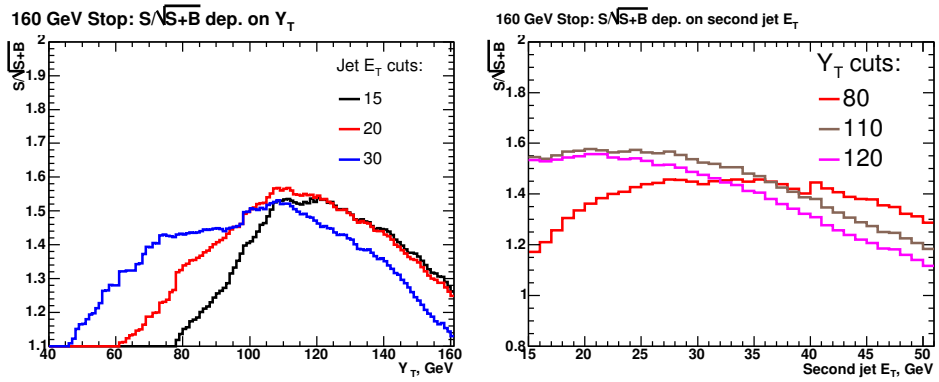

FIG. 13: $S/\sqrt{(S+B)}$ as a function of value of Y_T cut for several choices of jet energy threshold (left) and jet energy threshold for several choices of minimal Y_T (right).

f. Summary of Additional Requirements Efficiencies

Events that satisfy the requirement on Y_T are sorted into six regions, according to the values of m_T and $N_{\rm jet}$(see Section IV.A.3). This concludes the additional event level requirements selection. Results for $m(\tilde{t}_1)$=150 GeV/c^2 stop events in region A are shown in Table XXI.

g. Total Signal Event Acceptance in the Signal and Control Regions

Table XXII gives total selection efficiencies for region A as well as scale factors required to obtain efficiency for all the complementary regions for a range of stop masses. Total selection efficiency for regions C and D is always less than 0.01% and can be safely ignored compared to expected background contribution in these regions. Figure 14 on page 74 shows total selection efficiency for region A versus stop mass for CEM electron, CMUP muon, CMX muon and combined CMUP+CMX muon channels. The efficiency exhibits almost linear growth when $m(\tilde{t}_1)$ is increasing.

TABLE XXI: Efficiency of event level cuts for 150 GeV/c^2 stop. The last two cuts are applicable for region A only.

Requirement	$e + \tau_{\rm h}$	CMUP $\mu + \tau_{\rm h}$	CMX $\mu + \tau_{\rm h}$
$Q_l \times Q_\tau = -1$	99.2 ± 0.1	99.2 ± 0.2	99.4 ± 0.3
Conversion Removal	97.9 ± 0.2	–	–
Cosmic Removal	–	100.0	100.0
$Z \rightarrow ll$ Removal	90.9 ± 0.5	99.4 ± 0.2	99.5 ± 0.2
$Y_T(l, \tau, \not\!\!E_T) > 110$ GeV	79.8 ± 0.7	83.4 ± 0.7	77.9 ± 1.5
$N_{\rm jet} \geq 2$	83.3 ± 0.7	84.0 ± 0.8	83.8 ± 1.5
$m_T(l, \not\!\!E_T) < 35$ GeV/c^2	69.3 ± 1.0	69.0 ± 1.1	72.9 ± 1.9
Cumulative	40.7 ± 0.8	47.7 ± 1.0	47.1 ± 1.7

TABLE XXII: Total selection efficiency for region A as well as scale factors required to obtain efficiency for the complementary regions B, A′ and B′. Total selection efficiency for regions C and D is always less than 0.01% and can be safely ignored compared to expected background contribution in these regions. Scale factors are included (including corrections for the stub finding efficiency).

	$m(\tilde{t}_1)$ [GeV/c^2]			
	100	110	120	130
$\epsilon_{\rm A}^{\rm CEM}$[%]	0.60 ± 0.03	0.93 ± 0.02	1.31 ± 0.04	1.65 ± 0.05
$f_{\rm B}/f_{\rm A}$	43.9 ± 3.3	39.5 ± 2.4	42.0 ± 2.1	41.3 ± 1.8
$f_{\rm A'}/f_{\rm A}$	54.2 ± 3.7	39.5 ± 2.4	29.6 ± 1.8	26.8 ± 1.5
$f_{\rm B'}/f_{\rm A}$	18.4 ± 2.1	14.0 ± 1.5	10.4 ± 1.1	11.3 ± 1.0
$f_{\rm C}/f_{\rm A}$	7.1 ± 1.3	3.0 ± 0.7	2.8 ± 0.6	1.7 ± 0.4
$f_{\rm D}/f_{\rm A}$	2.6 ± 0.8	0.5 ± 0.3	0.1 ± 0.1	0.5 ± 0.2
$\epsilon_{\rm A}^{\rm CMUP}$[%]	0.46 ± 0.02	0.69 ± 0.03	0.94 ± 0.03	1.17 ± 0.04
$f_{\rm B}/f_{\rm A}$	36.6 ± 3.2	37.8 ± 2.6	40.3 ± 2.3	38.5 ± 2.0
$f_{\rm A'}/f_{\rm A}$	44.0 ± 3.5	36.4 ± 2.6	32.5 ± 2.1	25.4 ± 1.6
$f_{\rm B'}/f_{\rm A}$	14.7 ± 2.0	13.5 ± 1.6	13.2 ± 1.3	8.8 ± 1.0
$f_{\rm C}/f_{\rm A}$	7.8 ± 1.5	3.3 ± 0.8	3.5 ± 0.7	1.2 ± 0.4
$f_{\rm D}/f_{\rm A}$	2.5 ± 0.8	1.5 ± 0.5	0.4 ± 0.2	0.3 ± 0.2
$\epsilon_{\rm A}^{\rm CMX}$[%]	0.17 ± 0.02	0.26 ± 0.02	0.36 ± 0.02	0.44 ± 0.03
$f_{\rm B}/f_{\rm A}$	34.5 ± 5.6	40.1 ± 4.7	30.0 ± 3.5	39.6 ± 3.6
$f_{\rm A'}/f_{\rm A}$	53.1 ± 7.0	22.7 ± 3.6	35.0 ± 3.7	25.3 ± 2.9
$f_{\rm B'}/f_{\rm A}$	19.5 ± 4.2	15.1 ± 2.9	13.2 ± 2.3	8.9 ± 1.7
$f_{\rm C}/f_{\rm A}$	11.5 ± 3.2	2.9 ± 1.3	0.8 ± 0.6	1.4 ± 0.7
$f_{\rm D}/f_{\rm A}$	2.7 ± 1.5	1.2 ± 0.8	0.4 ± 0.4	0.7 ± 0.5
	140	150	160	170
$\epsilon_{\rm A}^{\rm CEM}$[%]	2.08 ± 0.05	2.33 ± 0.06	2.49 ± 0.06	2.73 ± 0.06
$f_{\rm B}/f_{\rm A}$	39.6 ± 1.6	44.3 ± 1.6	49.8 ± 1.6	48.8 ± 1.5
$f_{\rm A'}/f_{\rm A}$	23.0 ± 1.2	18.6 ± 1.0	16.4 ± 1.0	14.4 ± 0.9
$f_{\rm B'}/f_{\rm A}$	9.4 ± 0.8	9.2 ± 0.7	8.4 ± 0.7	7.0 ± 0.6
$f_{\rm C}/f_{\rm A}$	1.2 ± 0.3	0.8 ± 0.2	0.7 ± 0.2	0.6 ± 0.2
$f_{\rm D}/f_{\rm A}$	0.5 ± 0.2	0.4 ± 0.1	0.2 ± 0.1	0.3 ± 0.1
$\epsilon_{\rm A}^{\rm CMUP}$[%]	1.38 ± 0.04	1.65 ± 0.05	1.79 ± 0.05	2.04 ± 0.05
$f_{\rm B}/f_{\rm A}$	41.1 ± 1.9	44.9 ± 1.8	47.9 ± 1.8	43.0 ± 1.6
$f_{\rm A'}/f_{\rm A}$	19.7 ± 1.3	17.0 ± 1.1	17.0 ± 1.1	15.3 ± 1.0
$f_{\rm B'}/f_{\rm A}$	7.9 ± 0.8	9.5 ± 0.8	8.2 ± 0.8	6.7 ± 0.6
$f_{\rm C}/f_{\rm A}$	1.1 ± 0.3	0.7 ± 0.2	0.8 ± 0.2	0.7 ± 0.2
$f_{\rm D}/f_{\rm A}$	0.4 ± 0.2	0.5 ± 0.2	0.6 ± 0.2	0.2 ± 0.1
$\epsilon_{\rm A}^{\rm CMX}$[%]	0.51 ± 0.03	0.59 ± 0.03	0.67 ± 0.03	0.72 ± 0.03
$f_{\rm B}/f_{\rm A}$	42.9 ± 3.4	37.2 ± 3.0	45.0 ± 3.0	50.9 ± 3.1
$f_{\rm A'}/f_{\rm A}$	18.5 ± 2.3	16.4 ± 2.0	12.7 ± 1.7	14.5 ± 1.7
$f_{\rm B'}/f_{\rm A}$	6.5 ± 1.4	9.5 ± 1.5	7.1 ± 1.3	8.2 ± 1.3
$f_{\rm C}/f_{\rm A}$	2.1 ± 0.8	0.3 ± 0.3	0.7 ± 0.4	0.4 ± 0.3
$f_{\rm D}/f_{\rm A}$	0.9 ± 0.5	0.3 ± 0.3	0.2 ± 0.2	0.0 ± 0.0

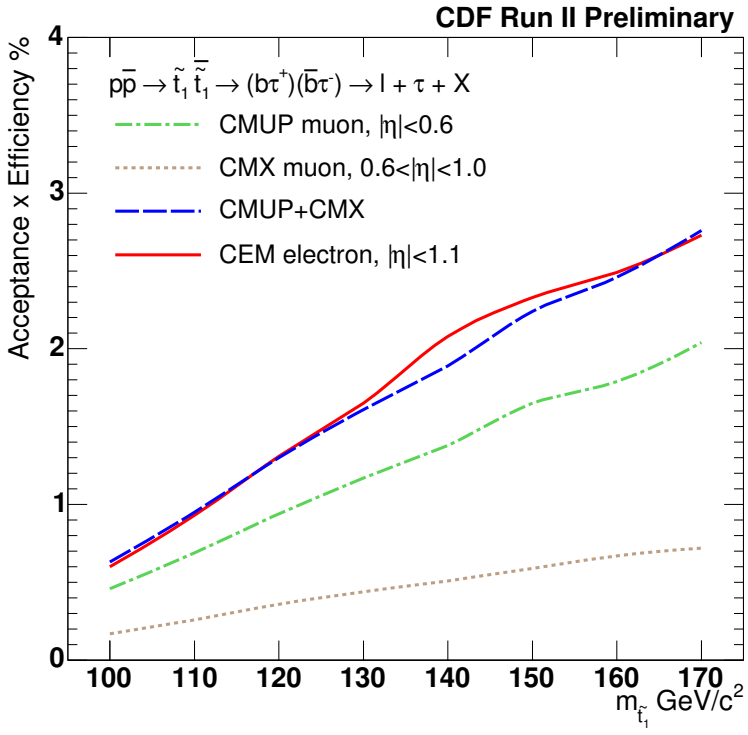

FIG. 14: Total selection efficiency for region A versus stop mass for CEM electron, CMUP muon, CMX muon and combined CMUP+CMX muon channels.

D. Systematic Uncertainties for the Acceptance

In this section we discuss the remaining systematic uncertainties due to parton distribution functions, initial and final state radiation, jet energy scale, and $\not\!\!E_T$ resolution.

1. Parton Distribution Functions

To estimate the systematic uncertainty on the total event acceptance due to PDFs we employed the re-weighting method described in Refs. [71, 82, 83]. Instead of simulating many samples, this method allows to use a single sample to calculate acceptances for different PDF sets by weighting events according to the probability of observing their incoming partons[3] using each PDF set. For this task use a special "error" set of 20 uncertainty pairs of CTEQ6M [70]. This set is based on $\pm 1\sigma$ deviations of a diagonalized set of 20 parameters which have their most likely values tuned using a global fit to experimental data. We calculate the full event selection acceptance variations for all 40 "error" PDFs. The variations are taken with respect to the central best-fit PDF. All the variations are summed up in quadratures according to a special prescription [71] to obtain the positive and negative uncertainties on the acceptance. The results of these study are shown in Table XXIII. We take the average of "positive" and "negative" uncertainties as the symmetrized uncertainties.

Note that the CTEQ6M set does not include PDF variation due to the uncertainty on $\Lambda_{\rm QCD}$. We use the MRST group's sets of PDFs to estimate this uncertainty, which is taken as a difference between the acceptances obtained with MRST72 ($\Lambda_{\rm QCD} = 228$ MeV) and MRST75 ($\Lambda_{\rm QCD} = 300$ MeV). We find that its contribution is negligible.

[3] The information about partons is extracted from the HEPG bank.

TABLE XXIII: Uncertainties in the total selection efficiency ($\epsilon_{\rm A}$) for $\tilde{t}_1\bar{\tilde{t}}_1 \to b\bar{b}\tau_l\tau_{\rm h}$ due to variations in PDFs.

	$m(\tilde{t}_1)$ [GeV/c^2]							
	100	110	120	130	140	150	160	170
	$e+\tau$ channel							
Negative [%]	5.2	5.2	4.8	5.1	5.5	4.6	5.2	5.2
Positive [%]	3.7	3.7	3.4	3.3	3.4	2.9	3.1	3.2
$e+\tau$ average [%]	4.5	4.5	4.1	4.2	4.5	3.8	4.2	4.2
	$\mu+\tau$ channel							
Negative [%]	5.9	5.5	5.2	5.3	5.0	5.0	4.6	5.0
Positive [%]	4.1	3.7	3.4	3.6	3.3	3.1	3.1	3.2
Average [%]	5.0	4.6	4.3	4.5	4.2	4.1	3.9	4.1
$\Lambda_{\rm QCD}$ variation [%]	0.13	0.18	0.15	0.18	0.15	0.17	0.15	0.10
$\mu+\tau$ average [%]	5.0	4.6	4.3	4.5	4.2	4.1	3.9	4.1

2. Initial and Final State Radiation

The uncertainty due to the initial and final state radiation is estimated by separately turning the ISR and FSR switches in PYTHIA off. For that we used samples and methodology from our previous analysis iteration [84]. We assign systematic uncertainty of 1.5% for ISR and 2.0% for FSR. The results are in agreement with the results from Ref. [84] and the previous Run I studies indicate as well that these uncertainties are small.

This technique is known to overestimate the effect. However we decided to continue employing it because the contribution of the effect is small and it has no effect on the result. Also the resulting uncertainty numbers are easily influenced by statistical fluctuations which will cover any unaccounted effects of ISR/FSR.

3. Jet Energy Scale

To estimate the effect of imprecise knowledge of the jet energy scale, we used the standard CDF method described in Ref. [50] and provided in the JetUser package. This method allows shifting the jet scale up or down by 1σ. The sensitivity in the total event selection depends on how often signal events have jets that are around the energy threshold. By increasing the stop mass, one expects jets to be more energetic, which should decrease the importance of this uncertainty. Results of our estimations in Table XXIV agree with this expectation. We take an average of the up and down shifts as uncertainty. We verified that the results of the analysis are not sensitive to using the average value instead of the $\pm\sigma$ parts.

TABLE XXIV: Uncertainties in the total selection efficiency for $\tilde{t}_1\bar{\tilde{t}}_1 \to b\bar{b}\tau_l\tau_{\rm h}$ due to variations in jet energy scale (absolute and relative combined) using a standard method provided in the JetUser package.

	$m(\tilde{t}_1)$ [GeV/c^2]							
	100	110	120	130	140	150	160	170
	$e+\tau$ channel							
$+1\sigma$ [%]	9.2	7.4	8.6	4.6	3.9	2.7	2.0	1.3
-1σ [%]	−7.5	−10.0	−7.1	−5.8	−3.3	−4.3	−3.4	−1.8
Average [%]	8.4	8.7	7.8	5.2	3.6	3.5	2.7	1.6
	$\mu+\tau$ channel							
$+1\sigma$ [%]	6.7	8.8	7.1	5.2	3.8	2.3	2.0	1.3
-1σ [%]	−8.4	−6.4	−6.5	−5.5	−4.1	−2.3	−2.8	−1.0
Average [%]	7.6	7.6	6.8	5.4	3.9	2.3	2.4	1.2

4. Missing E_T Resolution

Another possible systematic effect that has to be considered is the accuracy in simulating the $\not\!\!E_T$ in MC, because our Y_T and m_T requirements are correlated with $\not\!\!E_T$.

As we are using jets for $\not\!\!E_T$ correction (see Section IV.C.6.d), a large part of that systematic effect is correlated with uncertainty of the jet energy scale, which was discussed in the previous section. Another part comes from the missing E_T for the tau decay. To account for the effect, we turn off calculation of the expanded tau cluster momentum (see Section IV.C.6.d) and use default tau cluster momentum for the correction of $\not\!\!E_T$. We take the resulting difference of the acceptances as a value of the systematic uncertainty, which turns out to be rather small. The values for different samples are presented in Table XXV.

TABLE XXV: Estimated uncertainties in the total selection efficiency for $\tilde{t}_1\bar{\tilde{t}}_1 \to b\bar{b}\tau_l\tau_{\rm h}$ obtained by turning off calculation of expanded tau cluster momentum used in correction of $\not\!\!E_T$.

	$m(\tilde{t}_1)$ [GeV/c^2]							
	100	110	120	130	140	150	160	170
$e+\tau$	0.9	0.3	0.5	0.1	0.8	0.4	1.0	1.2
$\mu+\tau$	0.8	2.1	0.9	0.9	0.8	0.8	0.6	1.4

5. Summary of the Systematic Uncertainties

A full list of all systematic uncertainties considered in this analysis is shown in Table XXVI. The list includes uncertainties discussed in this section as well as those considered earlier to provide a complete reference of all uncertainties affecting this study.

TABLE XXVI: Summary of systematic uncertainties in the $\tilde{t}_1\bar{\tilde{t}}_1 \to b\bar{b}\tau_l\tau_h$ study. The first number in each column corresponds to the $e + \tau_h$ channel and second one to the $\mu + \tau_h$ channel.

	$m(\tilde{t}_1)$ [GeV/c^2]							
Systematics Type	100	110	120	130	140	150	160	170
PDF $e(\mu)$	4.5(5.0)	4.5(4.6)	4.1(4.3)	4.2(4.5)	4.5(4.2)	3.8(4.1)	4.2(3.9)	4.2(4.1)
ISR	1.5	1.5	1.5	1.5	1.5	1.5	1.5	1.5
FSR	2.0	2.0	2.0	2.0	2.0	2.0	2.0	2.0
Jet Scale $e(\mu)$	8.4(7.6)	8.7(7.6)	7.8(6.8)	5.2(5.4)	3.6(3.9)	3.5(2.3)	2.7(2.4)	1.6(1.2)
$\not\!\!E_T$ $e(\mu)$	0.9(0.8)	0.3(2.1)	0.5(0.9)	0.1(0.9)	0.8(0.8)	0.4(0.8)	1.0(0.6)	1.2(1.4)
α $e(\mu)$	1.5(1.4)	1.5(1.4)	1.5(1.4)	1.5(1.4)	1.5(1.4)	1.5(1.4)	1.5(1.4)	1.5(1.4)
ID $e(\mu)$	1.0(3.0)	1.0(3.0)	1.0(3.0)	1.0(3.0)	1.0(3.0)	1.0(3.0)	1.0(3.0)	1.0(3.0)
ID τ	3.0	3.0	3.0	3.0	3.0	3.0	3.0	3.0
ISO	3.0	3.0	3.0	3.0	3.0	3.0	3.0	3.0
Total $e + \tau$	10.8	11.1	10.3	8.5	7.8	7.3	7.2	6.9
Total $\mu + \tau$	10.9	10.7	10.0	9.2	8.3	7.5	7.5	7.3

E. Background Estimation in the Control Regions

We estimate the number of SM events in control regions by using the method similar to one in the $Z \to \tau\tau$ cross section measurement [51].

1. $Z/\gamma^*(\to \tau\tau)$+jets

The $Z \to \tau\tau$ contribution is eveluated by using PYTHIA MC sample and applying the same cuts as in the data analysis.

The estimated $Z \to \tau\tau$ rate is corrected for scale factors (ID and reconstruction efficiencies) and trigger efficiency. Corresponding uncertainties are propagated into the final estimation of the $Z \to \tau\tau$ yield.

A special set of scale factors is necessary to correct kinematics of Z boson production in MC. Table XXVII presents the results for such scale factors in different regions for the case of $Y_T \geq 110$ GeV. The details on how these scale factors were estimated are given in Appendix C.

TABLE XXVII: Scale factors for $Z \to \tau\tau$ for $Y_T \geq 110$ GeV.

	N_{jet}		
	0	1	≥ 2
$m_T < 35$	$1.00 \pm 0.10(st) \pm 0.02(sys)$	$0.90 \pm 0.09(st) \pm 0.14(sys)$	$1.02 \pm 0.19(st) \pm 0.18(sys)$
$m_T > 35$	$0.99 \pm 0.18(st) \pm 0.02(sys)$	$0.94 \pm 0.23(st) \pm 0.11(sys)$	$1.03 \pm 0.23(st) \pm 0.19(sys)$

2. $Z/\gamma^*(\to ll)$+jets

$Z/\gamma^* \to \mu\mu$ can be backgrounds in two ways: (i) one of the muons passes hadronic tau requirements by leaving substantial deposition in the calorimeter, or (ii) the recoil jet in the $Z/\gamma^* \to \mu\mu$ event is misidentified for a hadronic tau while the event pass

$Z \to \mu\mu$ candidate removal either because one of the muons is not reconstructed (e.g., fall outside the detector coverage) or if the invariant mass of the two muon candidates falls outside the Z window mass cut. We use PYTHIA MC to estimate the size of these backgrounds and find it negligible in signal region A.

The contribution from the $Z \to ee$ events is larger because of a larger rate of electron to be misidentified as tau and due to larger bremsstrahlung effect.

We also need to use a special set of scale factors to correct kinematics of Z boson production in MC. As the phase space of Z boson is different between $Z \to \tau\tau$ and $Z \to ll$ after all the cuts were applied, the resulting scale factors that we present in Table XXVIII are also different than in the case of $Z \to \tau\tau$. The way they were estimated was different as well. Details of the study can be found in Appendix C.

TABLE XXVIII: Scale factors for $Z \to ee$ for $Y_T \geq 110$ GeV.

	N_{jet}		
	0	1	≥ 2
$m_T < 35$	1.07 ± 0.13	0.99 ± 0.12	1.28 ± 0.27
$m_T > 35$	0.87 ± 0.13	0.91 ± 0.12	1.19 ± 0.28

3. $t\bar{t}$ and Diboson Production

The $t\bar{t}$ and diboson production can naturally be backgrounds as they can have a real electron or muon and a hadronic tau in the final state. These backgrounds can be reliably estimated using corresponding MC and known NLO cross sections. The $t\bar{t}$ production gives considerable contribution to the region B. The cross sections that we use for $t\bar{t}$ and WW processes are 6.7 ± 0.7 pb [85] and 13.5 ± 0.5 pb [86] respectively.

In our previous study [84] we found that contributions from WZ and ZZ processes were negligibly small, so we don't consider them here.

4. QCD

Light-quark QCD production could mimic our signal when one jet is misidentified as an electron (e.g. conversions), while the other jet passes as a τ candidate. Typically, the track multiplicity of jets misidentified as $\tau_{\rm h}$ candidates peaks in the two-prong bin for the range of jet E_T and ${p_T}^{\tau}$ in this analysis [87]. On the other hand, heavy flavor QCD production has two important distinct features. First, it has "real" electrons from its semileptonic decays. Second, misidentified $\tau_{\rm h}$ candidates from heavy flavor jets have different track multiplicity distribution than real $\tau_{\rm h}$. This difference is likely due to the decay modes of B mesons[4].

Jet and tracking isolations (Section IV.C.4) which we apply to the lepton and tau candidates are very effective in suppressing this background. The QCD multijet contribution is estimated by extrapolating the number of observed events in data for events with non-isolated leptons, defined by 2 GeV/c $< I_{\rm trk}^{\Delta R<0.4} <$ 10 GeV/c, into the class of events with an isolated lepton, defined by $I_{\rm trk}^{\Delta R<0.4} <$ 2 GeV/c [51]. For example, we find no events in region A in the $e\tau_{\rm h}$ channel, and estimate a rate of $0.00^{+0.23}_{-0.00}$ QCD events in signal region.

5. W + jets

Each W + jets event can become a background event when a jet is misidentified as a tau candidate. However, this background can be strongly suppressed by the event

[4] E.g. some of the "heavy" mesons are good candidates for being misidentified as $\tau_{\rm h}$ (the $D^{\pm}$ meson has mass of 1.9 GeV/c^2 compared to m_{τ} = 1.8 GeV/c^2 and decays into three pions)

topology cuts that force remaining $W+$jets events to have low transverse mass, m_T, which is equivalent to require a heavy boost of the W, thus diminishing its contribution. The $W+$jets events that pass our selection criteria may originate from the $W(\rightarrow l)$+jets or $W(\rightarrow \tau\rightarrow l)$+jets processes. The $W(\rightarrow \tau\rightarrow l)$+jets events are suppressed by the branching ratio of the $\tau\rightarrow l$ decay. However, they have relatively low $\not\!\!E_T$ and m_T values because the neutrinos from W and τ decays partially compensate each other.

We use regions A, B, C, and D (see in Table VI) to perform statistical estimation of the $W+$jets rate. The details of the likelihood procedure are described in Section V.A. Here we note an important assumption on the procedure. The rate of W events scales so that

$$\mathcal{R} \equiv \left[N^{W+j}(\mathrm{B})/N^{W+j}(\mathrm{D})\right] / \left[N^{W+j}(\mathrm{A})/N^{W+j}(\mathrm{C})\right] = f^W_{\mathrm{BD}}/f^W_{\mathrm{AC}} \sim 1 \pm 0.5. \quad (4.12)$$

This assumption is based on the expectation that m_T distribution in W+jets events is primarily defined by decay of W boson, and should not be affected much by extra jets. Also, while the absolute $W+$jets rates from PYTHIA MC are unreliable, the ratios in $\mathcal{R}$ should be reasonably well modeled. We studied this assumption in details in the previous iteration of the analysis [84]. We checked with PYTHIA MC that it is true within the uncertainty of ± 0.5 margin (we had rather limited statistics of W plus more than one jet samples). We take $\mathcal{R}$ as a nuisance in our likelihood procedure (Section V.A) and use the ± 0.5 range for integration, assuming that its distribution is flat. The choice of the margin or of the distribution has little influence on the final results.

We carry out the estimate of the $W+$jets contribution using the technique described in Section V.A.4. We use a statistical procedure that builds two-dimensional likelihood dependent on $\sigma(\tilde{t}_1\bar{\tilde{t}}_1)\times\beta^2$ and N^W_i for some chosen region i. Note, that the

results for N_i^W estimates that are obtained there are presented only for the illustration purpose and are not independent from number of data events and contribution of other backgrounds.

6. Backgrounds Summary

Table XXIX presents a summary of the expected number of background events for each of the six regions from all sources except W + jets events (it is considered separately in Section V.A.4). The calculation assumes that the integrated luminosity for the CMUP and CEM data is 322 pb^{-1} and 304 pb^{-1} for the CMX data. These numbers include corresponding reconstruction and ID scale factors as well as the trigger simulation, uncertainty on the luminosity is not included.

TABLE XXIX: Summary of the SM backgrounds excluding the W+jet events.

Process	Expected Rate for $\mathcal{L} = 322$ pb^{-1} (303.7 pb^{-1} for CMX)					
	A	B	A′	B′	C	D
$e + \tau$ Channel						
$Z \to \tau\tau$	0.73 ± 0.12	0.38 ± 0.09	1.84 ± 0.19	0.42 ± 0.09	1.84 ± 0.19	0.56 ± 0.10
$Z \to ee$	0.76 ± 0.21	0.29 ± 0.13	1.59 ± 0.31	0.94 ± 0.24	6.45 ± 0.62	2.47 ± 0.38
QCD	$0.00^{+0.23}_{-0.00}$	$0.25^{+0.37}_{-0.18}$	$0.00^{+0.23}_{-0.00}$	$0.0^{+0.23}_{-0.00}$	$0.25^{+0.37}_{-0.18}$	$0.50^{+0.46}_{-0.28}$
$t\bar{t}$	0.26 ± 0.05	1.64 ± 0.13	0.03 ± 0.02	0.36 ± 0.06	0.00 ± 0.00	0.01 ± 0.01
WW	0.01 ± 0.01	0.14 ± 0.04	0.06 ± 0.03	0.64 ± 0.08	0.11 ± 0.03	1.30 ± 0.12
W+jet	To be determined in the fit					
Total $e\tau$:	$1.99^{+0.45}_{-0.39}$	$2.77^{+0.45}_{-0.31}$	$3.32^{+0.53}_{-0.47}$	$2.25^{+0.36}_{-0.28}$	$9.11^{+1.15}_{-1.10}$	$4.51^{+0.67}_{-0.56}$
$\mu + \tau$ CMUP Channel						
$Z \to \tau\tau$	0.50 ± 0.09	0.13 ± 0.05	1.19 ± 0.14	0.33 ± 0.07	2.02 ± 0.18	0.45 ± 0.09
$Z \to \mu\mu$	0.00 ± 0.47	0.39 ± 0.14	0.39 ± 0.14	0.59 ± 0.17	1.51 ± 0.27	2.25 ± 0.33
QCD	$0.00^{+0.23}_{-0.00}$	$0.00^{+0.23}_{-0.00}$	$0.50^{+0.46}_{-0.28}$	$0.25^{+0.37}_{-0.18}$	$0.25^{+0.37}_{-0.18}$	$0.50^{+0.46}_{-0.28}$
$t\bar{t}$	0.12 ± 0.03	0.96 ± 0.09	0.05 ± 0.02	0.24 ± 0.05	0.00 ± 0.00	0.05 ± 0.02
WW	0.02 ± 0.01	0.08 ± 0.03	0.04 ± 0.02	0.35 ± 0.06	0.09 ± 0.03	0.69 ± 0.08
W+jet	To be determined in the fit					
Total(*):	$0.65^{+0.27}_{-0.15}$	$1.65^{+0.32}_{-0.23}$	$2.04^{+0.53}_{-0.38}$	$1.69^{+0.42}_{-0.27}$	$3.99^{+0.54}_{-0.44}$	$3.65^{+0.63}_{-0.51}$
$\mu + \tau$ CMX Channel						
$Z \to \tau\tau$	0.19 ± 0.06	0.04 ± 0.03	0.40 ± 0.09	0.09 ± 0.04	0.51 ± 0.10	0.21 ± 0.06
$Z \to \mu\mu$	0.06 ± 0.06	0.11 ± 0.08	0.16 ± 0.10	0.33 ± 0.14	0.38 ± 0.15	1.10 ± 0.25
QCD	$0.00^{+0.23}_{-0.00}$	$0.00^{+0.23}_{-0.00}$	$0.00^{+0.23}_{-0.00}$	$0.00^{+0.23}_{-0.00}$	$0.25^{+0.37}_{-0.18}$	$0.25^{+0.37}_{-0.18}$
$t\bar{t}$	0.09 ± 0.03	0.38 ± 0.06	0.01 ± 0.01	0.07 ± 0.03	0.00 ± 0.00	0.01 ± 0.01
WW	0.01 ± 0.01	0.10 ± 0.03	0.01 ± 0.01	0.11 ± 0.03	0.02 ± 0.01	0.29 ± 0.05
W+jet	To be determined in the fit					
Total(*):	$0.37^{+0.25}_{-0.11}$	$0.65^{+0.26}_{-0.12}$	$0.54^{+0.27}_{-0.14}$	$0.57^{+0.27}_{-0.14}$	$1.20^{+0.42}_{-0.26}$	$1.71^{+0.46}_{-0.33}$
Total $\mu\tau$:	$1.02^{+0.37}_{-0.18}$	$2.29^{+0.42}_{-0.26}$	$2.58^{+0.59}_{-0.40}$	$2.25^{+0.50}_{-0.30}$	$5.18^{+0.69}_{-0.51}$	$5.36^{+0.78}_{-0.61}$

CHAPTER V

SETTING LIMITS

A. The Fit Procedure and Limit Setting Methods

For statistical interpretation of the data, we developed a likelihood method that utilizes our primary signal region A and side-band regions B, C, and D (Section IV.A.3) simultaneously. It improves the sensitivity of the analysis and allows to perform a data-driven W + jets background estimation. We fit the number of events in regions A, B, C, and D to estimate overall normalizations of signal and W + jets backgrounds with the assumption of $\mathcal{R} \sim 1$. During the fitting we take into account all signal acceptances, non-W background predictions and observations in data for all the four regions.

The result of such statistical interpretation is either to set upper 95% C.L. limits on $\sigma(\tilde{t}_1\bar{\tilde{t}}_1) \times \beta^2$ or to measure the value of $\sigma(\tilde{t}_1\bar{\tilde{t}}_1) \times \beta^2$ in case of an observed data excess in the signal region.

1. Building the Likelihood

As discussed earlier, out of the four regions, signal is expected to dominate in region A as well as in region B.[1] The W + jets events are primarily in region D as well as in regions C and B. All four regions have contributions from other previously discussed backgrounds, which are summarized in Table XXIX.

We build a likelihood function as follows: we start with combined rates of signal and background processes, ν_i, in each of the four regions i =A, B, C, D and calculate

[1]Region B has $\sim$ 40% of number of signal events in region A for $m(\tilde{t}_1) = 150$ GeV/c^2

probability of the true rates being within $d\nu_i$ of ν_i given the number of observed events N_i:

$$d\mathcal{P} = \prod_{i=\mathrm{A,B,C,D}} P(\nu_i, N_i) d\nu_i, \tag{5.1}$$

where $P(\nu_i, N_i)$ is simple Poisson distribution for expected rate ν_i and the number of observed events N_i.

We then define $\epsilon_i = \nu_i^s/\nu_A^s$ for the signal events (i =B, C, D) and express each rate as a sum of rates of W, signal and "other" background events (superscripts w, s and b, respectively):

$$\begin{aligned}
\nu_\mathrm{A} &= \nu_\mathrm{A}^b + \nu_\mathrm{A}^w + \nu_\mathrm{A}^s \\
\nu_\mathrm{B} &= \nu_\mathrm{B}^b + \nu_\mathrm{A}^w/\nu_\mathrm{C}^w \times \nu_\mathrm{D}^w \times r + \epsilon_B \nu_\mathrm{A}^s \\
\nu_\mathrm{C} &= \nu_\mathrm{C}^b + \nu_\mathrm{C}^w + \epsilon_C \nu_\mathrm{A}^s \\
\nu_\mathrm{D} &= \nu_\mathrm{D}^b + \nu_\mathrm{D}^w + \epsilon_D \nu_\mathrm{A}^s .
\end{aligned} \tag{5.2}$$

Here $r = (\nu_\mathrm{B}^w/\nu_\mathrm{D}^w)/(\nu_\mathrm{A}^w/\nu_\mathrm{C}^w)$, which would be 1 if the scaling for the number of $W+$jets events was exact. It is introduced as a nuisance parameter with flat distribution in the 0.5 to 1.5 region to account for possible deviations from exact equality (see Section IV.E.5 for more discussion). We perform a transformation of variables $(\nu_\mathrm{A}, \nu_\mathrm{B}, \nu_\mathrm{C}, \nu_\mathrm{D}) \to (\nu_\mathrm{A}^w, \nu_\mathrm{C}^w, \nu_\mathrm{D}^w, \nu_\mathrm{A}^s)$. The Jacobian of this transformation is

$$J = \epsilon_\mathrm{C} r \frac{\nu_\mathrm{A}^w \nu_\mathrm{D}^w}{(\nu_\mathrm{C}^w)^2} - \epsilon_\mathrm{D} r \frac{\nu_\mathrm{A}^w}{\nu_\mathrm{C}^w} + \epsilon_\mathrm{B} - r \frac{\nu_\mathrm{D}^w}{\nu_\mathrm{C}^w} = r \frac{\nu_\mathrm{A}^w}{\nu_\mathrm{C}^w} (\epsilon_\mathrm{C} \frac{\nu_\mathrm{D}^w}{\nu_\mathrm{C}^w} - \epsilon_\mathrm{D}) + (\epsilon_\mathrm{B} - r \frac{\nu_\mathrm{D}^w}{\nu_\mathrm{C}^w}) \ . \tag{5.3}$$

After that we include existing prior knowledge about other than $W+$jets backgrounds and r assuming that those are nuisance parameters and will be integrated

out later:

$$\frac{d\mathcal{P}}{d\nu^s_{\rm A}} = \frac{1}{V^w}\int\int\int d\nu^w_{\rm A} d\nu^w_{\rm C} d\nu^w_{\rm D} \times \int_{0.5}^{1.5} dr \times \prod_{i=\rm A,B,C,D} \int_{\nu^b_i=0}^{\infty} d\nu^b_i exp\left[-\frac{(\nu^b_i-\nu^b_{i0})^2}{2{\sigma^b_i}^2}\right] \prod_{i=\rm A,B,C,D} P(\nu_i, N_i) \times J(r) dr \ , \quad (5.4)$$

where V^w is a phase volume of the integral over $\nu^w_{\rm A}$, $\nu^w_{\rm C}$, and $\nu^w_{\rm D}$, which we calculate with a flat prior distribution. The choice of V^w is fairly arbitrary as long as it is reasonable in a sense that the results have very little dependence on it if it covers well the region of possible expected values of $\nu^w_{\rm A}$, $\nu^w_{\rm C}$, and $\nu^w_{\rm D}$.

Finally, we replace the signal rate in region A with a physically meaningful cross section using $\nu^s_{\rm A} = \sigma(\tilde{t}_1\bar{\tilde{t}}_1) \times \beta^2 \times L \times \mathcal{B}(\tau\tau \to \tau_l\tau_{\rm h}) \times \alpha$, where α is the full selection efficiency of signal events for region A and L is the integrated luminosity. We include prior knowledge about the acceptance and its uncertainty and define likelihood as:

$$\mathcal{L}(\sigma) = \frac{d\mathcal{P}}{d\sigma} = \int d\alpha \times exp\left[-\frac{\alpha-\alpha_0}{2\sigma^2_\alpha}\right] \times L \times \mathcal{B} \times \alpha \times \frac{d\mathcal{P}}{d\nu^s_{\rm A}}, \quad (5.5)$$

where we denoted $\sigma \equiv \sigma(\tilde{t}_1\bar{\tilde{t}}_1) \times \beta^2$ for simplicity.

We perform numerical MC integration over all integration variables in physical region (all processes must have non-negative rates) to obtain the one-dimensional likelihood function as a function of the cross section. We use 95% C.L. highest posterior density intervals to determine the maximum allowed cross section value that we report as the final limit. Combined limit is obtained by using the product of two likelihood functions:

$$\mathcal{L}(\sigma) = \mathcal{L}^{e+\tau}(\sigma) \times \mathcal{L}^{\mu+\tau}(\sigma) \ . \quad (5.6)$$

2. *Incorporating Systematic Errors into the Fit*

Systematic effects may affect not only the overall rate of events passing our selections, but also how the events are distributed among the four regions and that some of the effects are correlated between electron and muon channels.

One example is the jet scale uncertainty: when the scale is moved up from its central value, passing events will on average have more jets and therefore one can expect a migration of the events from the bins with lower number of jets to bins with higher number of jets. To handle these effects, we first define a 3×2 matrix $\mathcal{A}_{ij}$, where i runs over three N_{jet} bins and j runs over two bins in m_T, and each value is the expected acceptances in a corresponding bin. For deviated cases, we re-calculate this matrix and call it $\mathcal{A}'$. We then introduce a parameter ω associated with a particular kind of uncertainty and use linearized approximation for $\mathcal{A}(\alpha)$ as:

$$\mathcal{A}_{ij}(\alpha) = \mathcal{A}_{ij} + \omega \times (\mathcal{A}'_{ij} - \mathcal{A}_{ij}), \tag{5.7}$$

where α is the full selection efficiency of signal events for region A.

We then choose an appropriate prior p.d.f. for each case, treat corresponding ω's as nuisance parameters and integrate them out. We call this a *matrix* method, as opposed to *number* method, when we assume that the systematics does not cause noticeable migration between bins.

Some of the uncertainties, e.g., luminosity or tau ID, are correlated between electron and muon channels. Each of these is uncertainties is treated separately assuming 100% correlation between the electron and muon channels. In Table XXX, we give a short summary of the assumptions used in fitting. To simplify calculations, we separately combine all fully uncorrelated *number*-type uncertainties into one including the uncertainty due to limited MC statistics.

TABLE XXX: Handling of systematic uncertainties in the fit.

Type	Method	Prior p.d.f.(ω)	Degree of Correlation
Jet Energy Scale	matrix	gauss	100%
$\not\!\!E_T$	matrix	1 if $0 < \omega < 1$, else 0	100%
PDF	number	gauss	100%
τ ID	number	gauss	100%
ISR	number	gauss	100%
FSR	number	gauss	100%
Luminosity	number	gauss	100%
Acceptance	number	gauss	0%
$e(\mu)$ ID	number	gauss	0%
Statistical uncertainty	number	gauss	0%

3. Likelihood for the Combined Channels

We finally use the likelihood as in Eqs. (5.5) and (5.6) with σ_α defined as a sum in quadratures of uncorrelated systematic uncertainties (last group in Table XXX) and statistical uncertainty due to limited MC statistics.

To account for systematic effects correlated between channels, we adjust α_0 in the likelihood to account for possible systematic shifts:

$$\begin{aligned} \alpha_0^e &= \alpha_0^e \times (1 + \sum x_i \times \sigma_i^e) \\ \alpha_0^\mu &= \alpha_0^\mu \times (1 + \sum x_i \times \sigma_i^\mu) \ , \end{aligned} \tag{5.8}$$

where i runs over all systematics types, σ_i is the size of the systematic uncertainty of type i, and x_i are corresponding random shifts. We accordingly correct fractions $\epsilon_{\rm B}$, $\epsilon_{\rm C}$ and $\epsilon_{\rm D}$. We then re-write Eq. (5.6) as

$$\mathcal{L}(\sigma) = \int f(\vec{x}) d\vec{x} \mathcal{L}^{e+\tau}(\sigma, \vec{x}) \times \mathcal{L}^{\mu+\tau}(\sigma, \vec{x}) \ , \tag{5.9}$$

where $f(\vec{x})$ is assumed the probability density function for $\vec{x}$ and is a product of

individual PDFs (most of which are simple gauss functions, except for the $\not\!\!E_T$ case, when it is a θ-function). This simple procedure provides desired values of correlations between the two channels.

4. Estimation of W + jets Background from Likelihood

In order to check if our fitting procedure estimates W + jets background properly, we transform the likelihood function in Eq. (5.5) into two dimensional likelihood:

$$\mathcal{L}(\sigma, \nu^w) = \frac{d\mathcal{L}(\sigma)}{d\nu^w} \ , \tag{5.10}$$

where $\nu^w = \nu_i^w$ is rate of W + jets events is some region of interest i, which means we just drop the integral over ν_i^w in Eq. (5.4). We can do this for any of the six regions, while appropriately changing definition of r and, if necessary, the Jacobian (see Eq. (5.3)). To obtain one-dimensional $\mathcal{L}(\nu^w)$ distributions we may integrate out the σ dependence. However, our studies show that the two-dimensional likelihood $\mathcal{L}(\sigma, \nu^w)$ always has maximum when $\sigma = 0$[2]. It allows us to use $\mathcal{L}(\nu^w) = \mathcal{L}(\sigma = 0, \nu^w)$ to estimate the highest posterior probability intervals for ν^w.

The results of this estimation are presented later in Table XXXI. They show that we have a reasonable tool for data-driven W + jets background estimation. However, it is not useful to compare sums of number of events for W + jets and other backgrounds to data, as they are not independent on each other.

[2]We did this study after opening the signal region for data events.

B. Data Results and the Validation of the Background Estimation and Fit Procedure

1. *Observed Number of Events in the Signal and Control Regions*

In Table XXXI we show the number of events observed in data in each of the six primary (isolated) region as well as in each of the six complementary (non-isolated, used for QCD background estimation) regions. The data in region A is shown in bold font to indicate that the box (region A) was not opened until all cuts were finalized and backgrounds were estimated.

TABLE XXXI: Number of events observed in data in each of the six isolated ($N_{\rm obs}$) and nonisolated (used for QCD background estimation) regions ($N_{\rm QCD}$), along with the expected number of SM background events. Note that the $W+$jets contributions are obtained from the maxima of likelihoods that depend on the observed number of events in the data, the number of SM events excluding the $W+$jets contribution and on the $\tilde{t}_1\bar{\tilde{t}}_1$ production cross section (see Section V.A.4).

	$e+\tau_{\rm h}$ Channel				$\mu+\tau_{\rm h}$ Channel			
Reg	$N_{\rm obs}$	$N_{\rm QCD}$	SM Backgrounds		$N_{\rm obs}$	$N_{\rm QCD}$	SM Backgrounds	
			Other	$W+$jets			Other	$W+$jets
A_2	**1**	0	$2.0^{+0.5}_{-0.4}$	$0^{+0.4}_{-0}$	**1**	0	$1.0^{+0.4}_{-0.2}$	$0^{+0.5}_{-0}$
B_2	4	1	$2.8^{+0.5}_{-0.3}$	$1.0^{+2.0}_{-1.0}$	4	0	$2.3^{+0.4}_{-0.3}$	$1.7^{+2.0}_{-1.5}$
A_1	4	0	$3.3^{+0.5}_{-0.5}$	$0.2^{+1.2}_{-0.2}$	3	2	$2.6^{+0.6}_{-0.4}$	$0.1^{+0.8}_{-0.1}$
B_1	9	0	$2.3^{+0.4}_{-0.3}$	$6.7^{+3.2}_{-2.7}$	6	1	$2.3^{+0.5}_{-0.3}$	$3.8^{+2.7}_{-2.1}$
A_0	11	1	$9.1^{+1.2}_{-1.1}$	$1.6^{+2.7}_{-1.6}$	8	2	$5.2^{+0.7}_{-0.5}$	$2.5^{+2.4}_{-2.1}$
B_0	25	2	$4.5^{+0.7}_{-0.6}$	$21.1^{+5.6}_{-4.3}$	28	3	$5.4^{+0.8}_{-0.6}$	$23.6^{+4.9}_{-5.7}$

In addition we quote the numbers for SM background contributions, separately for $W+$jets and other than $W+$jets backgrounds. We do not combine them into a total SM background, as the $W+$jets estimates depend on the numbers of events observed in data and the estimates for other backgrounds.

In Table XXXII we list some of the characteristic variables for the two events

which passed all the selection requirements for region A in data. Figures 15 and 16 present the event display pictures for these two events.

TABLE XXXII: List of kinematical values for two events which pass all the selection requirements in region A in data.

	e channel	mu channel
run:	185594	186145
event:	295912	3165242
E_T(e) or $p_T(\mu)$	75.8	13.6
lepton η/ϕ	0.63/6.11	−0.12/5.20
tau ${p_T}^{\rm vis}$	41.5	26.8
tau η/ϕ	−0.52/3.36	−0.48/3.59
# extra jets	2	3
jet1 η/ϕ	−1.04/1.78	−0.55/2.14
jet2 η/ϕ	0.54/3.47	−1.14/1.84
jet3 η/ϕ		−1.16/1.07
$E_T^{\rm cor}$(jet1)	60.6	60.4
$E_T^{\rm cor}$(jet2)	59.7	29.3
$E_T^{\rm cor}$(jet3)		25.4
${\not\!\!E_T}^{\rm raw}$	9.02	70.6
$\not\!\!E_T$	29.8	81.9
$\phi({\not\!\!E_T}^{\rm raw})$	6.12	5.40
$\phi(\not\!\!E_T)$	5.90	5.24
$m_T(l, \not\!\!E_T)$	10.2	1.23
Y_T	146.8	122.3
$m(l, \tau)$	128.8	28.5
$m(l, \text{jet1})$	179.7	59.0
$m(l, \text{jet2})$	130.6	44.9
$m(\tau, \text{jet1})$	77.8	54.7
$m(\tau, \text{jet2})$	57.8	47.3

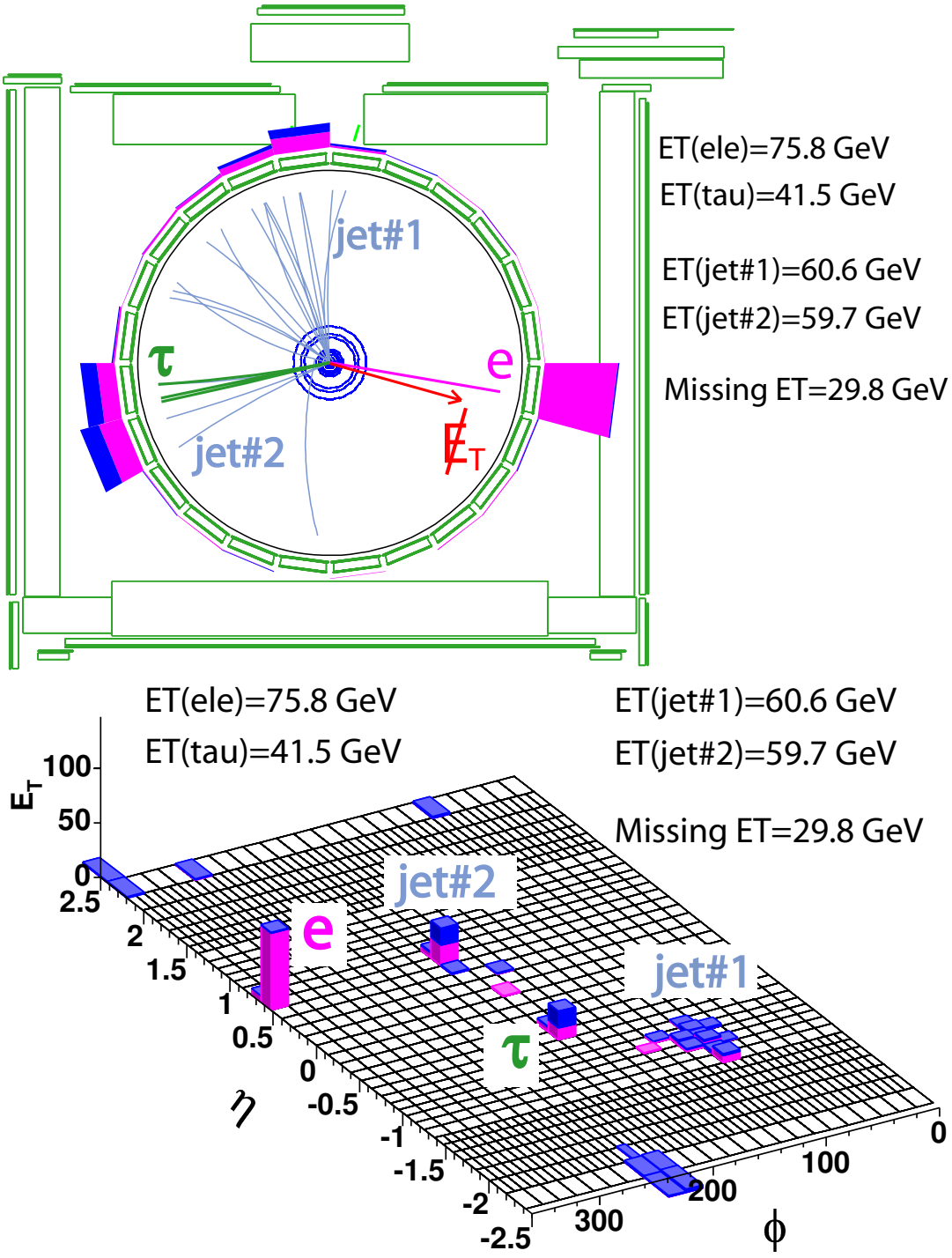

FIG. 15: Tracking and calorimeter displays for an $e\tau+2$ *jets* event (run 185594, event 295912) which passed all the selection requirements in region A..

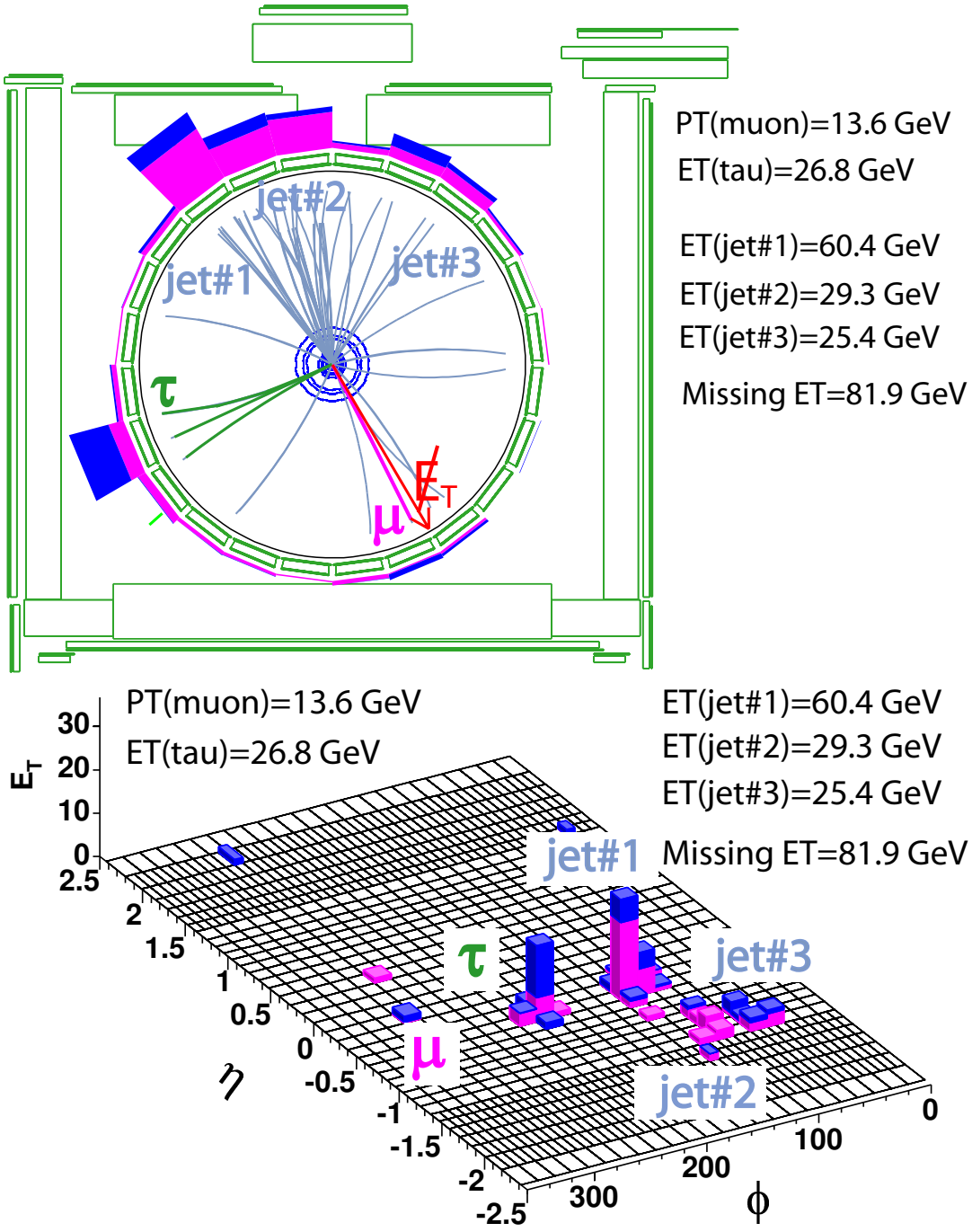

FIG. 16: Tracking and calorimeter displays for a $e\tau + 3$ *jets* event (run 186145, event 3165242) which passed all the selection requirements in region A.

2. *The Y_T >80* GeV *Control Region*

Distributions of m_T for the regions B, A′+B′ and C+D for the case of looser cut on Y_T >80 GeV (to have higher statistics) are shown in Fig. 17. Note that we use MC W + jets samples for the plots but we choose scale factor for them to get better agreement with data. Also for the muon channel we borrow the W + jets shapes from the electron channel, as there's no big enough samples of $W(\rightarrow \mu\nu)$+jets.

In Fig. 18 we present Y_T distributions for regions C and A′. Figure 19 shows MET distributions for events with Y_T >80 GeV and passed all other cuts in region C. Figure 20 displays distributions of the number of prongs in final tau candidates for the region C. Figure 21 is illustrating lepton p_T (E_T for electron) and tau visible p_T in region C. In Fig. 22 the ${E_T}^{\rm cor}$ for the leading (has the biggest ${E_T}^{corr}$) and second jets in region A, and the only jet's ${E_T}^{corr}$ in region A′ are shown. Figure 23 presents distributions of the number of jets in final candidate events with $m_T < 35$ GeV/c^2 and Y_T <80 GeV.

Data and background predictions agree reasonably well in all the plots. Especially illustrative plots are shown in Figs. 17, 20, and 23. This validates our procedure in the Y_T >80 GeV control region.

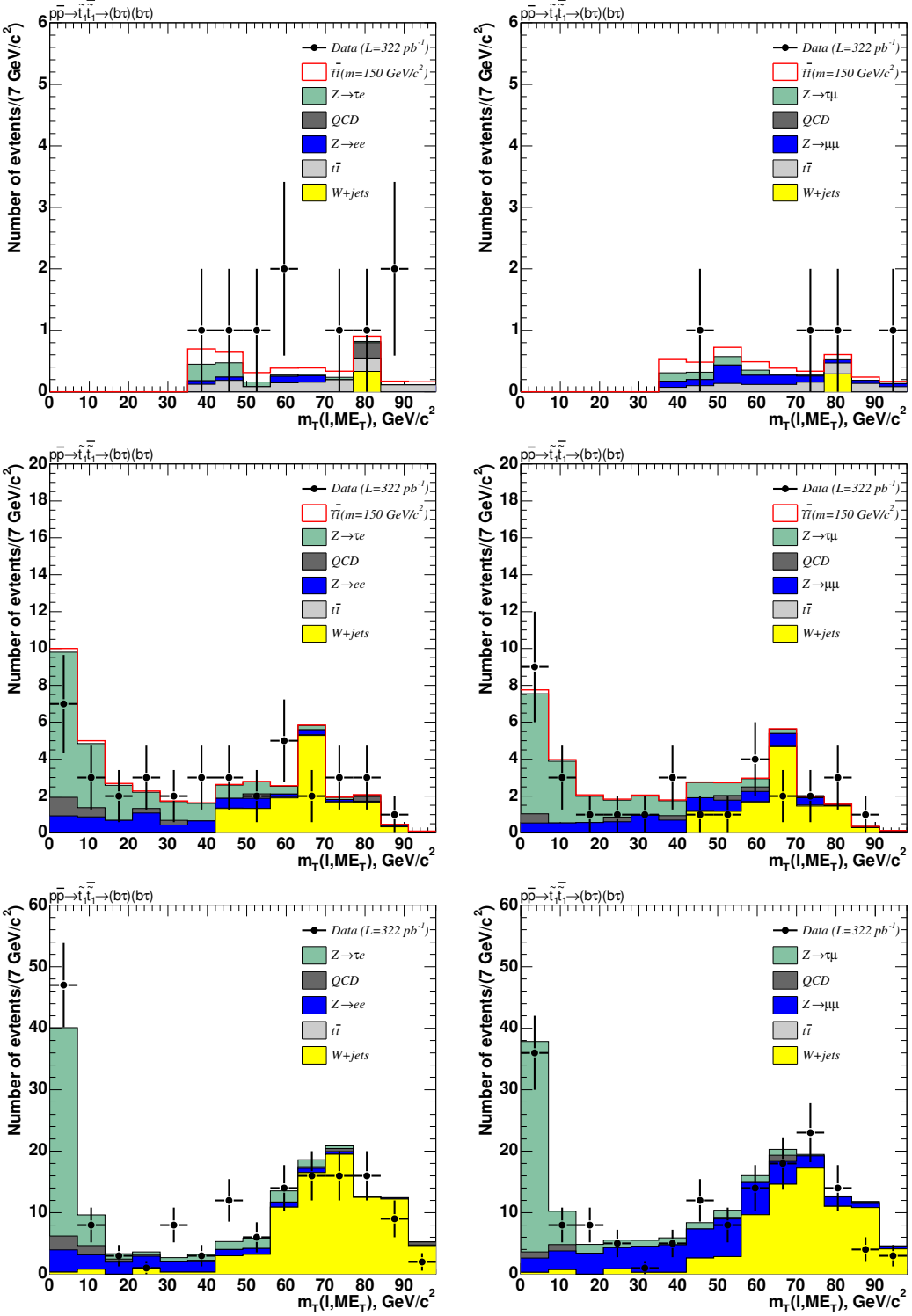

FIG. 17: Distributions of $m_T(l, \not\!\!E_T)$ in the control regions B (top), A′+B′ (middle) and C+D (bottom) (note, that we do not plot anything in region A) for events with Y_T >80 GeV in electron (left) and muon (right) channels.

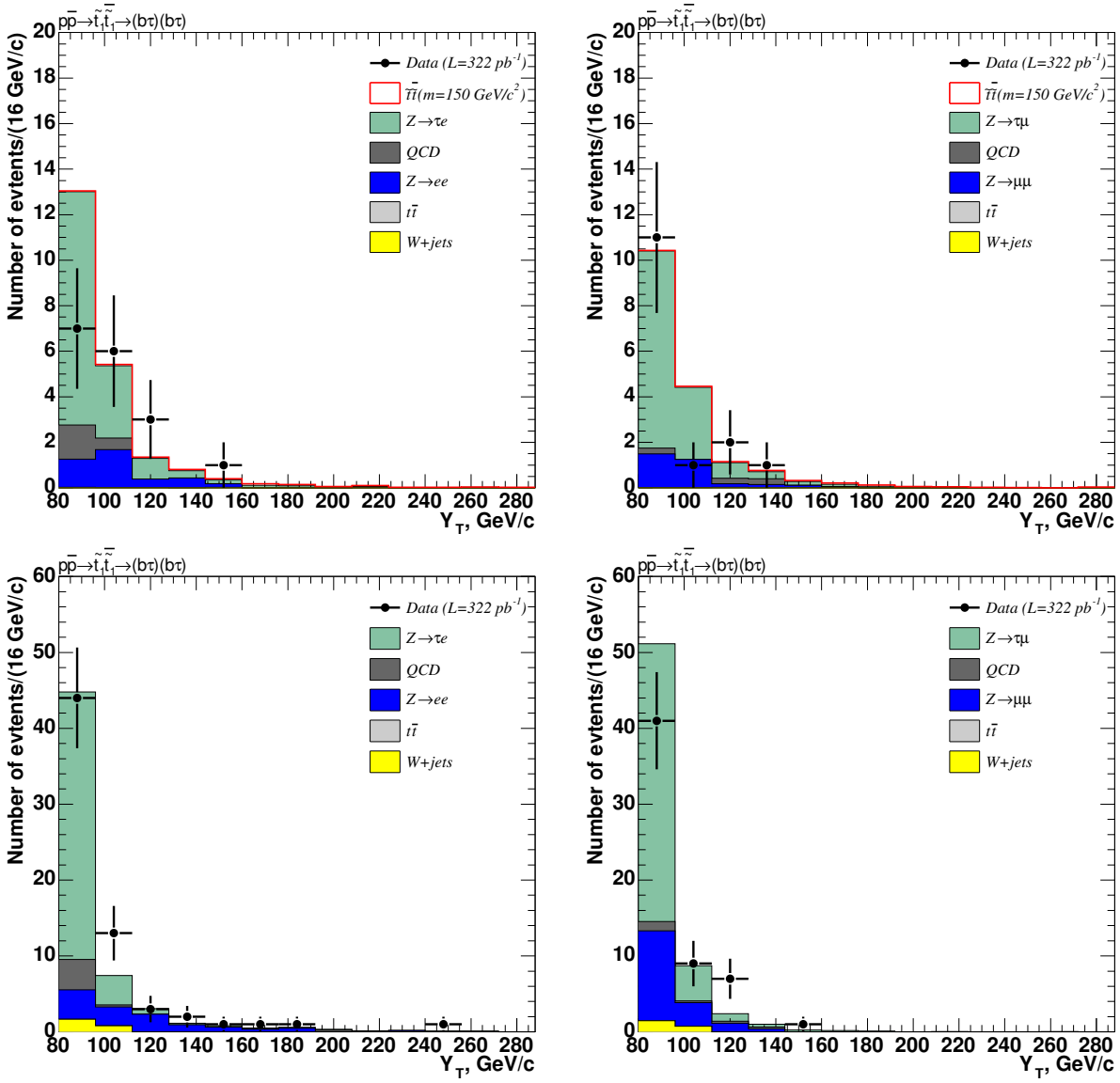

FIG. 18: Distributions of Y_T in regions A′ (top) and C (bottom) for events with Y_T >80 GeV in electron (left) and muon (right) channels.

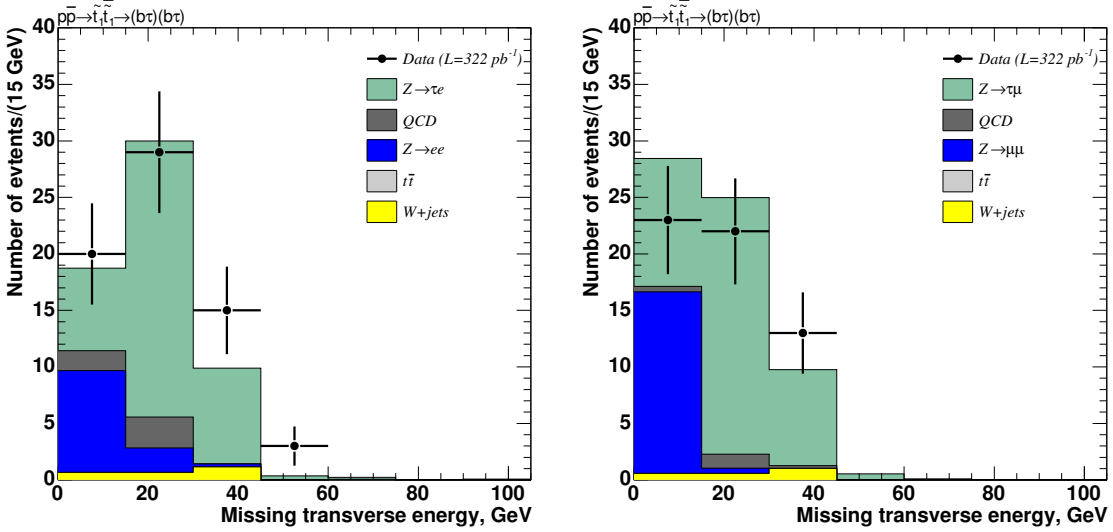

FIG. 19: Distributions of $\not\!\!E_T$ in region C for events with Y_T >80 GeV in electron (left) and muon (right) channels.

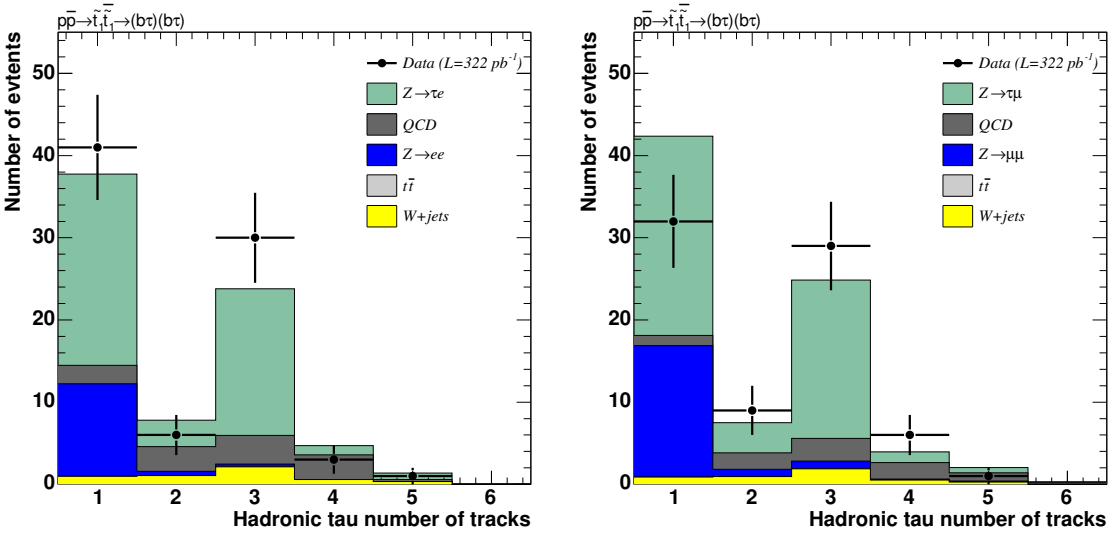

FIG. 20: Distributions of the number of tracks in final tau candidates in region C for events with Y_T >80 GeV in electron (left) and muon (right) channels. We observe a clear tau signature in 1-track and 3-track bins.

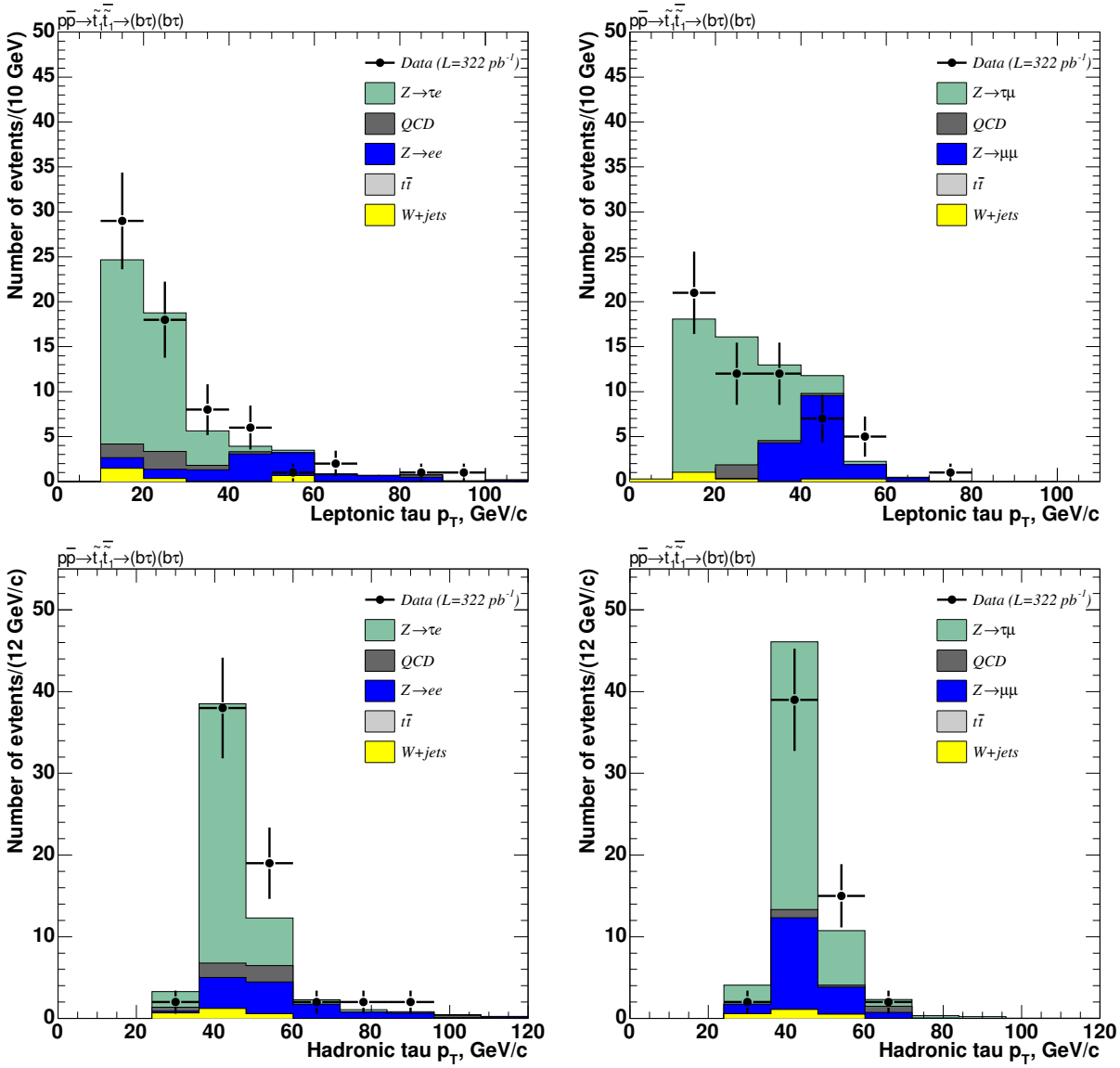

FIG. 21: Distributions for lepton p_T and tau $p_T{}^{\rm vis}$ for events with Y_T >80 GeV in electron (left) and muon (right) channels in region C.

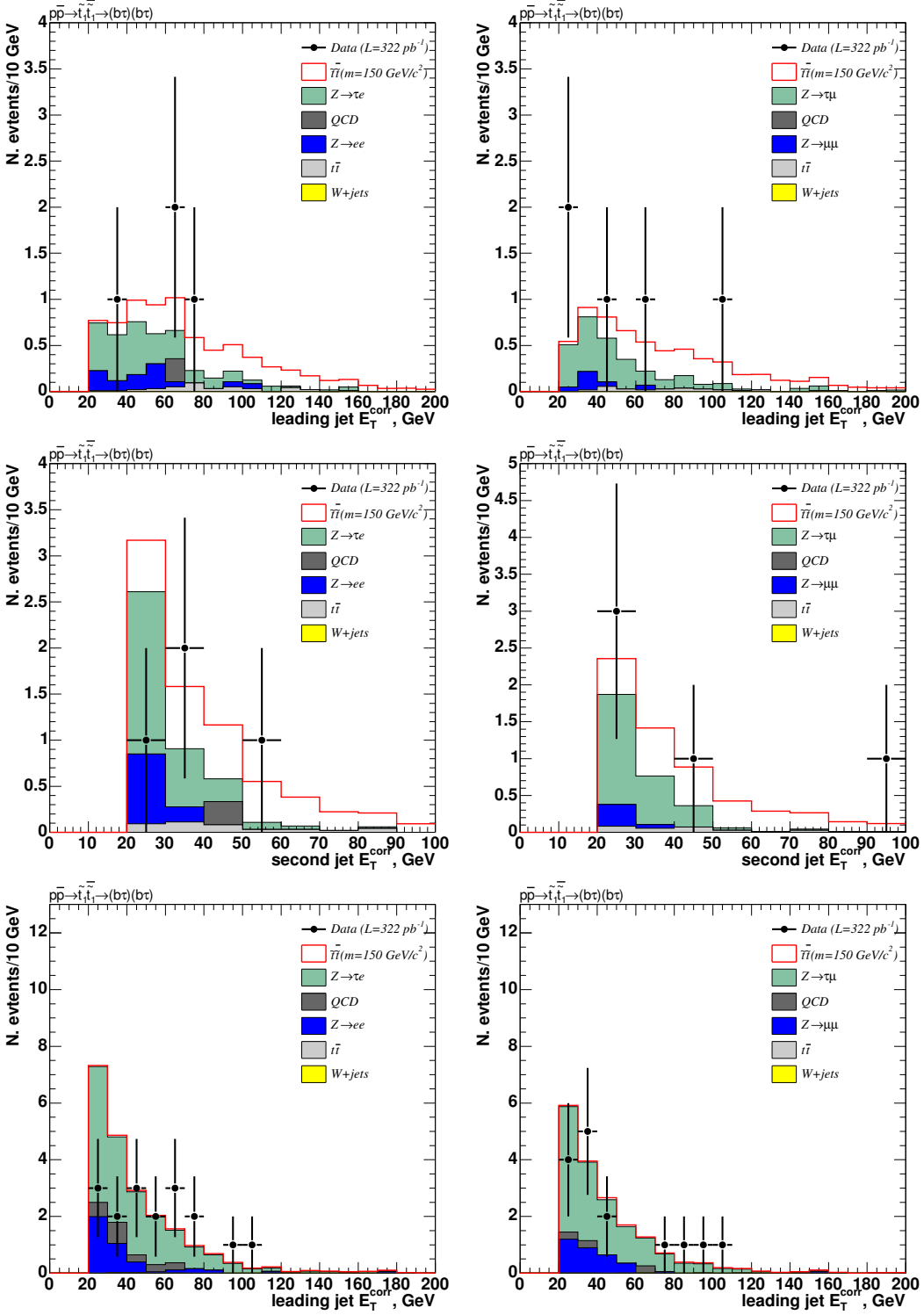

FIG. 22: Jet $E_T^{\rm cor}$ distributions for events with Y_T >80 GeV in electron (left) and muon (right) channels. From top to bottom they are for leading jet in region A, second leading jet in region A, and the jet in region A′.

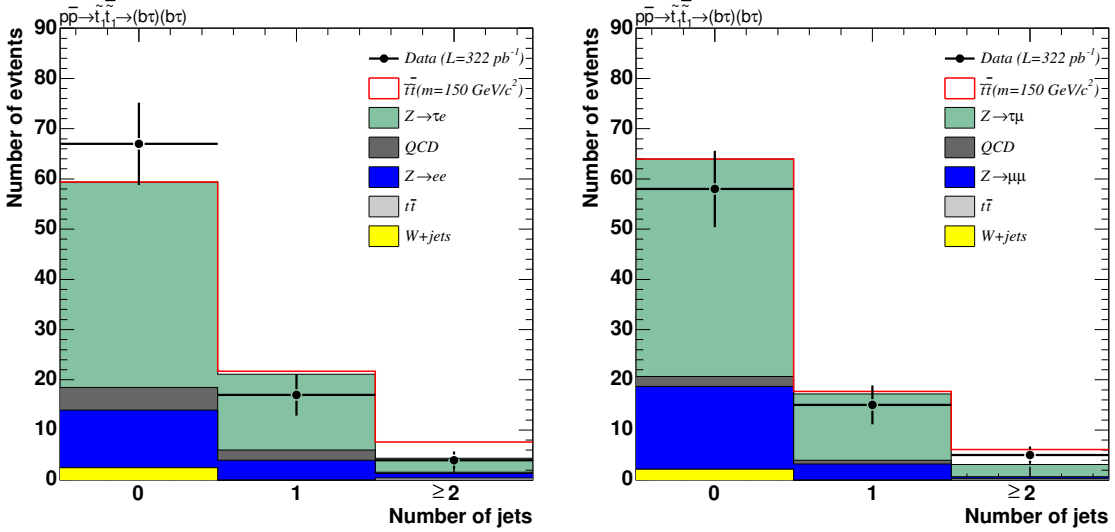

FIG. 23: Distributions of the number of jets in final candidate events for events with $m_T < 35$ GeV/c^2 and $Y_T > 80$ GeV in electron (left) and muon (right) channels.

3. *The $N_{\rm jet} = 0$ and $N_{\rm jet} = 1$ Control Regions*

If one takes into account the current limit on the stop mass (122 GeV/c^2), the expectation for the stop events in the region of $N_{\rm jet} = 1$ is absolutely negligible and therefore it can also serve as a control region. It is obvious that the W+jets background is negligible in regions A′ and C, and the agreement between data and expected backgrounds is good. E.g., see Fig. 24 for electron and muon channels separately, and Fig. 25 for the combined plot. Note that we looked at the data in the $N_{\rm jet} \geq 2$ bins only after the procedure was verified and finalized. However, we still can use our standard fitting procedure to estimate "signal" rate (in events, not in pb) in region A′ using as input the number of events in B′ and in the $N_{\rm jet} = 0$ bins. We expect no signal events and the fit returns a P.D.F. in agreement with expectation of no signal events in that region[3].

[3]As expected in this case, due to a relatively large expected number of background events in "signal" region A′, the P.D.F. is quite wide and only provides a very impre-

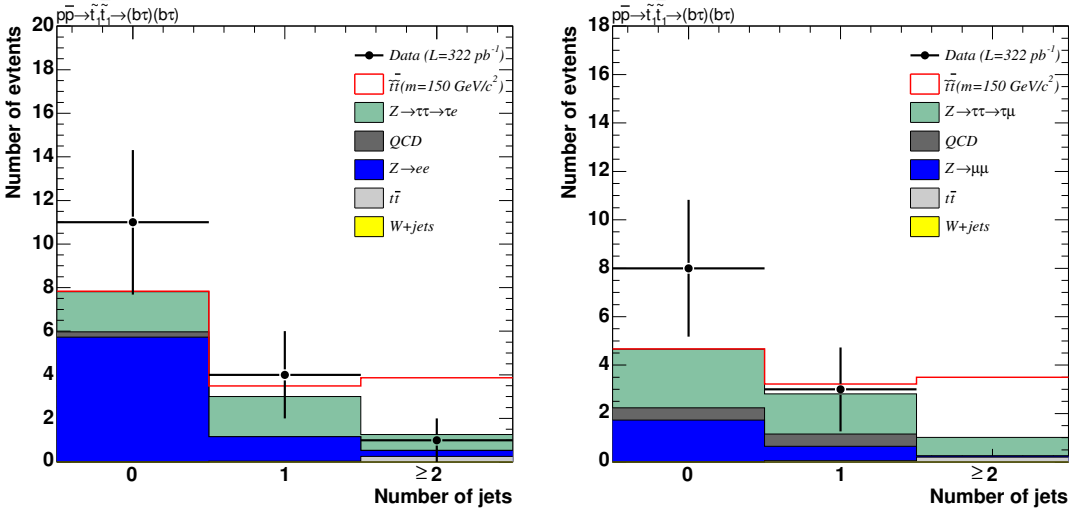

FIG. 24: Distributions of the number of jets in final candidate events for $m_T < 35$ GeV/c^2 region for electron (left) and muon (right) channel.

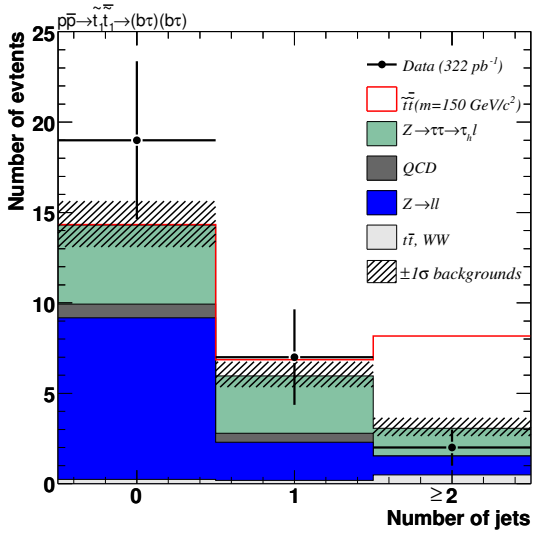

FIG. 25: Event distribution as a function of the number of jets with $E_T > 20$ GeV separated from the lepton and tau candidates for data events with $m_T(l, \not\!\!E_T) \leq 35$ GeV/c^2 (regions A, A′, and C) compared to the expectations from SM background processes and prediction for $\tilde{t}_1\bar{\tilde{t}}_1$ ($m(\tilde{t}_1) = 150$ GeV/c^2) signal. The SM background processes shown do not include the W + jets contribution.

cise confirmation that no large fluctuations happened in the region in question.

4. The Fit Procedure Performance Test

To show that the fitting routine produces expected results, we perform the following check: for each of the four regions, we sum up the rates for "known" backgrounds with the expected number of W events in each region as predicted by MC. We then calculate the expected number of stop events in each of the regions assuming that stop production exists with some cross section and add it to the sum. We round up the expected rate to represent the observed number of data events and apply our standard fit procedure. The result of this pseudo-experiment for the case of a 130 GeV stop with a cross section of 10 pb with the fit applied to the muon channel only is illustrated in Fig. 26. It shows the output PDF as a function of the stop cross section and it is clearly in good agreement with the 10 pb expectation.

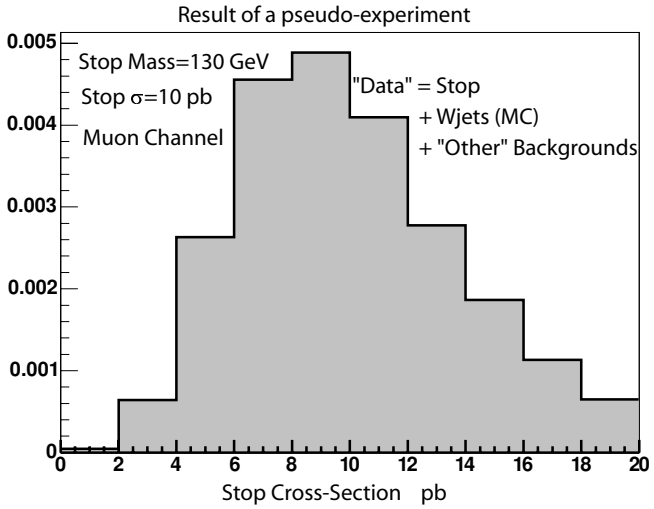

FIG. 26: PDF for the stop cross section obtained using the standard fit method for data obtained in a pseudo-experiment, in which the stop has a mass of 130 GeV/c^2 with a production cross section of 10 pb, rate of the W + jets background events is obtained using MC and other backgrounds are the same as in the real analysis. Fit is applied to muon data only. PDF obtained is consistent with the reference cross section.

C. Limits with 322 pb^{-1} Data

A total of two events are found in signal region A, which can be compared to the prediction from SM processes of roughly 3 events (see Table XXXI). With no excess in this region, we calculate a 95% C.L. upper limit on the $\tilde{t}_1\bar{\tilde{t}}_1$ production cross section times the square of branching ratio of stop RPV decay into τb pair. By comparing this limit curve to the stop pair production curve we set a 95% confidence level limit on stop quark mass.

1. Stop Pair Production Cross Section Limits

We calculate 95% C.L. upper limits on $\sigma(\tilde{t}_1\bar{\tilde{t}}_1) \times \beta^2$ as a function of stop mass, Table XXXIII, with or without convoluting uncertainties on theoretical prediction for the cross section (see Section IV.B) into our limit calculation. This is due to the fact that our fitting procedure relies on possible signal event contribution in every of the four regions. The limit without theoretical uncertainty on the cross section are our primary results on $\sigma(\tilde{t}_1\bar{\tilde{t}}_1) \times \beta^2$ limits. The limits with theoretical uncertainty are used for setting a conservative limit on stop mass.

TABLE XXXIII: 95% C.L. upper limit on $\sigma(\tilde{t}_1\bar{\tilde{t}}_1) \times \beta^2$ (in pb) as a function of $m(\tilde{t}_1)$ for the cases when theoretical uncertainty on the cross section is considered ($\sigma^{95\%}_{with\ uncert} \times \beta^2$) and is not considered ($\sigma^{95\%}_{no\ uncert} \times \beta^2$). Here $\beta \equiv \mathcal{B}(\tilde{t}_1 \to \tau b)$. Note that the limit result were the theoretical uncertainty on the cross section was considered should not be interpreted as the upper limit on the cross section and is only intended for setting a conservative limit on stop mass.

$m(\tilde{t}_1)$ [GeV/c^2]	100	110	120	130	140	150	160	170
$\sigma^{95\%}_{no\ uncert} \times \beta^2$ [pb]	4.48	3.11	2.27	1.81	1.47	1.26	1.16	1.04
$\sigma^{95\%}_{with\ uncert} \times \beta^2$ [pb]	4.73	3.37	2.50	1.99	1.61	1.38	1.26	1.14

The band in Fig. 27 shows the expected limit in case of no discovery for combined analysis of electron and muon channels and corresponds to the 68% probability range of possible limits obtained by assuming that the observed number of events follows the background expectation. The computation was performed while not taking theoretical uncertainty on the cross section into account. Actual limit on the cross section was set based on two observed events (one event in the muon channel and one event in the electron channel) overlaid with the theoretical stop cross section using CTEQ6M PDF set shown as a solid line, while dashed lines indicate the theoretical uncertainty in the cross section calculation due to renormalization and factorization scales and PDF. Also shown are previously existing limits on stop mass (or, which is equivalent, on the third generation scalar leptoquark, $\tilde{S}_0$ or S_1, mass). Appendix D provides additional discussion on interpretation of the results for third generation scalar leptoquarks.

2. Stop Mass and $\mathcal{B}(\tilde{t}_1 \to \tau b)$ Limits

Without theoretical uncertainties on $\sigma(\tilde{t}_1\bar{\tilde{t}}_1)$, the 95% C.L. upper limit on stop mass is set at the intersection of the 95% C.L. upper limit on $\sigma \times \beta^2$ curve and the theoretical prediction for $\sigma(\tilde{t}_1\bar{\tilde{t}}_1)$ This results in the limit of $m(\tilde{t}_1)$ >156 GeV/c^2 (see Fig. 27).

Setting a conservative mass limit requires accounting for theoretical uncertainties in the calculation of the stop production cross section, which are approximately 18% of the cross section value (see Section IV.B). This error is convoluted into the fitting procedure and results of calculation of the upper limit are also shown in Table XXXIII. These are used to set the mass limit by finding an intersection of the limit curve with the default cross section line (see the bottom plot in Fig. 28). We arrived to a mass limit of $m(\tilde{t}_1)$ >153 GeV/c^2. First two plots in Fig. 28 show how this limit compares to the ones which were obtained in Run I analysis [13] and our previous iteration of

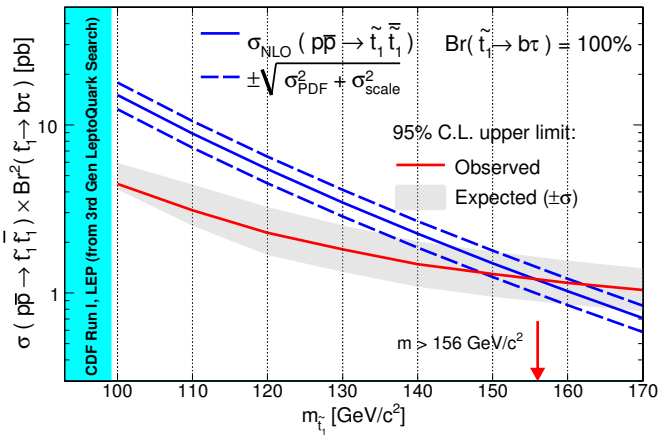

FIG. 27: Theoretical prediction for the $\tilde{t}_1\bar{\tilde{t}}_1$ production cross section (solid blue line) and its uncertainty due to factorization and normalization scales combined with the PDF uncertainty (dashed blue lines). Expected 95% C.L. upper limits for the $\tilde{t}_1\bar{\tilde{t}}_1$ production cross section (electron and muon channels are combined) are shown in red solid curve with a grey band (corresponds to a 68% probability range of possible limit if data were to follow SM background expectation). Earlier constraint obtained from CDF and LEP leptoquark searches ($m(LQ_3) > 99$ GeV/c^2) is shown. In all cases we assume the branching ratio $LQ_3 \to \tau b = 100\%$. The 95% C.L. limit on stop mass at $m(\tilde{t}_1)$ >156 GeV/c^2 was set without taking into account uncertainties on theoretical cross section.

the analysis with 200 pb^{-1} of data [84].

Also it should be noted that if one wants to be very conservative, the mass limit might be set at the intersection of the 95% C.L. upper limit curve which does not have the theoretical uncertainties convoluted in with the lower cross section uncertainty curve. This gives the most conservative mass limit of $m(\tilde{t}_1)$ >150 GeV/c^2.

Using the information from Fig. 29 we find 95% C.L. lower limit on branching ratio of stop decaying into a tau and a b quark as a function of $m(\tilde{t}_1)$ limit. The region above the solid line is excluded at 95% C.L.

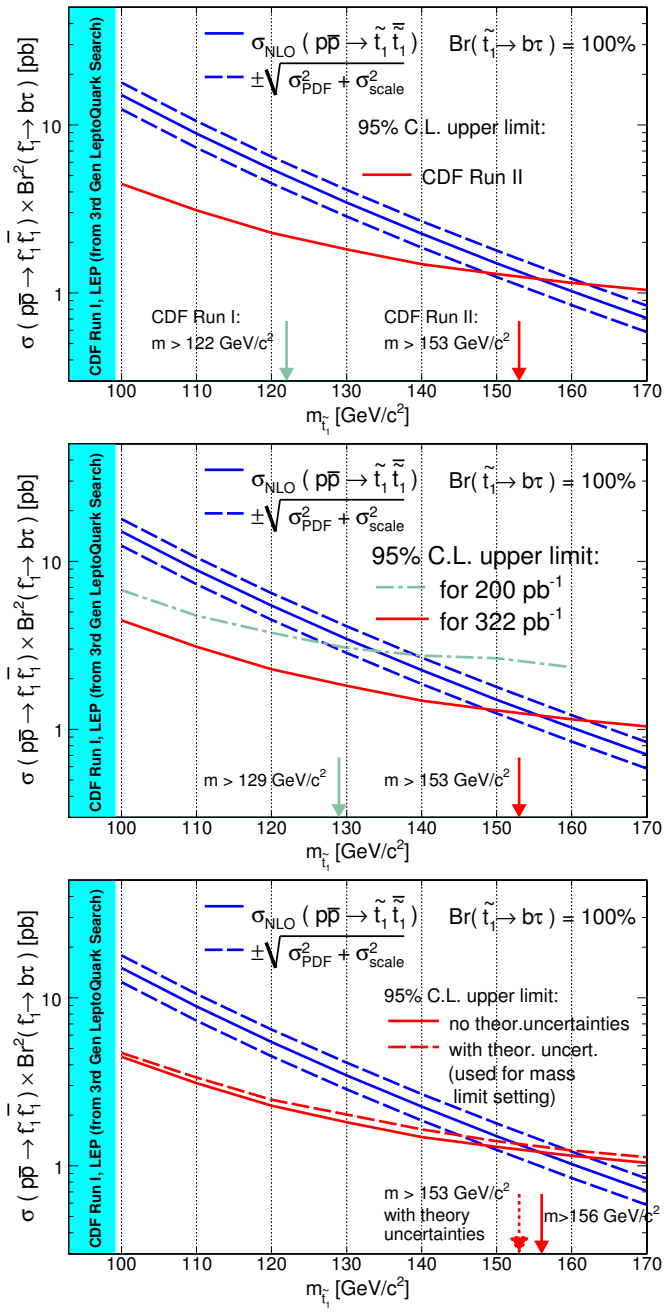

FIG. 28: Theoretical prediction for the $\tilde{t}_1\bar{\tilde{t}}_1$ production cross section (solid blue line) and its uncertainty due to factorization and normalization scales combined with the PDF error (dashed blue lines). Expected 95% C.L. upper limits on the $\tilde{t}_1\bar{\tilde{t}}_1$ production cross section are shown with red curve by combining resilts in electron and muon channels. For comparison, similar limit curve from our 200 pb^{-1} analysis (dash-dotted green line) and from Run I analysis [13] (green line) is shown. Dotted red curve represents 95% C.L. upper limit with 18% uncertainties on theoretical cross section taken into account in the fit. This curve is used to set 95% C.L. limit on stop mass which includes uncertainties on theoretical cross section at $m(\tilde{t}_1)$ >153 GeV/c^2.

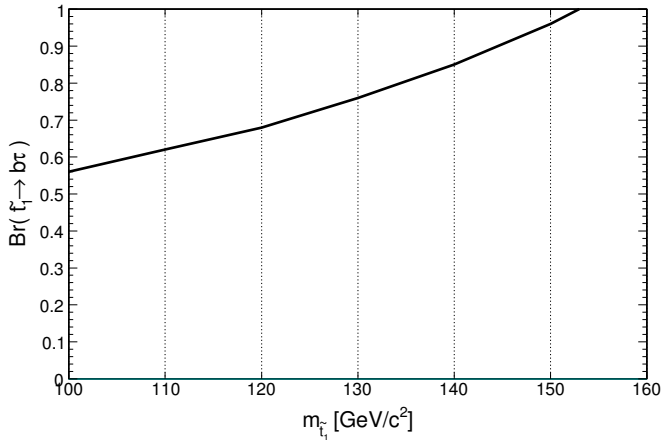

FIG. 29: 95% C.L. lower limit on branching ratio of stop decaying into a tau leptone and a b quark as a function of $m(\tilde{t}_1)$ limit. The region above the solid curve is excluded.

D. Prospects for Future Analyses

There are good prospects for RPV stop searches in a bigger dataset with luminosity of 2 fb^{-1} or more. A simple projection to 2 fb^{-1} is made by scaling the number of signal and background events together with the luminosity and choosing the expected number of events observed in data to be the same as the expected scaled SM background prediction. Such an estimate gives the expected value of stop mass limit at around 180 GeV/c^2. But this is also a minimal limit that we may expect at this luminosity, as the analysis procedure should be reoptimized for such an increased amount of data. While the current study would not benefit from employing the b tagging capapilities of CDF II detector[4], b tagging would be a major source of improvement for a big dataset, as it would greatly reduce contribution of all backgrounds except

[4]Due to relatively low efficiency of b tagging ($\sim$ 50%) and low statistics of the dataset the limit would not be improved if we would require at least one jet to be consistent with originating from the hadronization of a b quark.

top pair production, which has jets coming from real b quarks. The whole analysis methodology, regions, and limit calculation methods need to be rethought in this case.

Another possible extension for this analysis is to increase its physics scope by incorporating other possible RPV stop decays, namely considering also $\tilde{t}_1 \to eb$ and $\tilde{t}_1 \to \mu b$ together with $\tilde{t}_1 \to \tau b$. Such study is motivated by findings based on neutrino oscillation data [12], which show that the branching ratios of stop decaying into eb or μb could be as sizable as one of the $\tilde{t}_1 \to \tau b$ decay. The analysis complexity would be much higher, but the sensitivity and the physics value would be higher as well.

CHAPTER VI

CONCLUSION

We performed a search for stop quark pair production in a framework of R-parity violating SUSY where stop may decay into τb. The final state signature includes one lepton (e or μ), an hadronically decaying τ lepton, plus at least two jets. We did not require each jet to be consistent with originating from the hadronization of a b quark.

We observed two events which are consistent with the SM precesses expectation. Therefore, we set upper limits on the stop pair production cross section times $\mathcal{B}(\tilde{t}_1 \to \tau b)^2$ as a function of the stop mass. By taking into account the theoretical uncertainties on the NLO cross section and assuming $\mathcal{B}(\tilde{t}_1 \to \tau b) = 1$, we set a 95% C.L. lower limit on the $\tilde{t}_1$ mass of 153 GeV/c^2. Our results also exclude $\mathcal{B}(\tilde{t}_1 \to \tau b) > 0.56$ (0.74) if $m(\tilde{t}_1) = 100$ (130) GeV/c^2. These results are also applicable to LQ_3 pair production.

REFERENCES

[1] S. Weinberg, *The Quantum Theory of Fields, Vols. 1-3.* (Cambridge Univ. Pr., Cambridge, UK, 1995-2000).

[2] H. P. Nilles, Phys. Rept. **110**, 1 (1984); H. E. Haber and G. L. Kane, Phys. Rept. **117**, 75 (1985).

[3] S. P. Martin, "A Supersymmetry Primer," arXiv:hep-ph/9709356.

[4] S. Weinberg, Phys. Rev. D **26**, 287 (1982); G. R. Farrar and S. Weinberg, Phys. Rev. D **27**, 2732 (1983); S. Dawson, Nucl. Phys. B **261**, 297 (1985).

[5] R. Barbier *et al.*, Phys. Rept. **420**, 1 (2005); arXiv:hep-ph/0406039.

[6] M. Chemtob, Prog. Part. Nucl. Phys. **54**, 71 (2005); arXiv:hep-ph/0406029.

[7] K. Inoue, A. Kakuto, H. Komatsu, and S. Takeshita, Prog. Theor. Phys. **68**, 927 (1982); Erratum-*ibid.* **70**, 330 (1983); L. E. Ibanez and C. Lopez, Nucl. Phys. B **233**, 511 (1984); J. R. Ellis and S. Rudaz, Phys. Lett. B **128**, 248 (1983).

[8] F. de Campos, M. A. Diaz, O. J. P. Eboli, M. B. Magro, L. Navarro, W. Porod, D. A. Restrepo, and J. W. F. Valle, "R-parity Violating Decays of the Top-Quark and the Top-Squark at the Tevatron," arXiv:hep-ph/9903245.

[9] W. Porod, D. Restrepo, and J. W. F. Valle, "Light Stop: MSSM Versus R-Parity Violation," arXiv:hep-ph/0001033.

[10] D. Restrepo, W. Porod, and J. W. F. Valle, Phys. Rev. D **64**, 055011 (2001); arXiv:hep-ph/0104040.

[11] S. P. Das, A. Datta, and M. Guchait, Phys. Rev. D **70**, 015009 (2004); arXiv:hep-ph/0309168.

[12] S. P. Das, A. Datta, and S. Poddar, Phys. Rev. D **73**, 075014 (2006); arXiv:hep-ph/0509171.

[13] D. E. Acosta *et al.* (CDF Collaboration), Phys. Rev. Lett. **92**, 051803 (2004); arXiv:hep-ex/0305010.

[14] For a review on models with leptoquarks, see S. Davidson, D. C. Bailey, and B. A. Campbell, Z. Phys. C **61**, 613 (1994); arXiv:hep-ph/9309310.

[15] G. Abbiendi *et al.* (OPAL Collaboration), Eur. Phys. J. C **31**, 281 (2003); arXiv:hep-ex/0305053.

[16] F. Abe *et al.* (CDF Collaboration), Phys. Rev. Lett. **78**, 2906 (1997).

[17] L. Brigliadori *et al.* (CDF Collaboration), "Search for Pair Production of Scalar Top Quarks Decaying to a τ Lepton and a b Quark in $p\overline{p}$ Collisions at $\sqrt{s} = 1.96$ TeV," arXiv:0802.3887 (to be published).

[18] W. M. Yao *et al.* (Particle Data Group), J. Phys. G **33**, 1 (2006).

[19] M. C. Gonzalez-Garcia and M. Maltoni, "Phenomenology with Massive Neutrinos," arXiv:0704.1800.

[20] D. N. Spergel *et al.* (WMAP Collaboration), Astrophys. J. Suppl. **170**, 377 (2007); arXiv:astro-ph/0603449.

[21] G. Bertone, D. Hooper, and J. Silk, Phys. Rept. **405**, 279 (2005); arXiv:hep-ph/0404175.

[22] G. W. Bennett *et al.* (Muon $g-2$ Collaboration), Phys. Rev. Lett. **89**, 101804 (2002); Erratum-*ibid.* **89**, 129903 (2002); arXiv:hep-ex/0208001.

[23] M. Davier, Nucl. Phys. Proc. Suppl. **169**, 288 (2007); arXiv:hep-ph/0701163.

[24] D. Stockinger, "$(g-2)_\mu$ and Supersymmetry: Status and Prospects," arXiv:0710.2429 (to be published).

[25] D. J. H. Chung, L. L. Everett, G. L. Kane, S. F. King, J. D. Lykken, and L. T. Wang, Phys. Rept. **407**, 1 (2005); arXiv:hep-ph/0312378.

[26] S. Scopel, "Particle Dark Matter Candidates," arXiv:0711.2870 [hep-ph].

[27] L. M. Krauss and F. Wilczek, Phys. Rev. Lett. **62**, 1221 (1989); L. E. Ibanez and G. G. Ross, Phys. Lett. B **260**, 291 (1991).

[28] A. Dedes, S. Rimmer, and J. Rosiek, JHEP **0608**, 005 (2006); arXiv:hep-ph/0603225.

[29] B. C. Allanach, A. Dedes, and H. K. Dreiner, Phys. Rev. D **69**, 115002 (2004); Erratum-*ibid.* D **72**, 079902 (2005); arXiv:hep-ph/0309196.

[30] A. Alves, O. Eboli, and T. Plehn, Phys. Lett. B **558**, 165 (2003); arXiv:hep-ph/0211441.

[31] Fermilab Visual Media Services, Graphic Arts Gallery, http://www-visualmedia.fnal.gov (accessed on April 25, 2008).

[32] Tevatron Accelerator Division, *Operations Rookie Books*, http://www-bdnew.fnal.gov/operations/rookie_books/rbooks.html (accessed on April 25, 2008).

[33] D. E. Acosta *et al.* (CDF Collaboration), Phys. Rev. D **71**, 032001 (2005); arXiv:hep-ex/0412071.

[34] CDF Pictures Database, http://www-cdf.fnal.gov/events/pics.html (accessed on April 25, 2008).

[35] R. Blair *et al.* (CDF Collaboration), Fermilab Report No. FERMILAB-PUB-96-390-E.

[36] C. S. Hill *et al.* (CDF Collaboration), Nucl. Instrum. Meth. A **530**, 1 (2004).

[37] A. Sill *et al.* (CDF Collaboration), Nucl. Instrum. Meth. A **447**, 1 (2000).

[38] A. A. Affolder *et al.* (CDF Collaboration), Nucl. Instrum. Meth. A **453**, 84 (2000).

[39] A. A. Affolder *et al.* (CDF Collaboration), Nucl. Instrum. Meth. A **526**, 249 (2004).

[40] L. Balka *et al.* (CDF Collaboration), Nucl. Instrum. Meth. A **267**, 272 (1988).

[41] S. Bertolucci *et al.* (CDF Collaboration), Nucl. Instrum. Meth. A **267**, 301 (1988).

[42] M. G. Albrow *et al.* (CDF Collaboration), Nucl. Instrum. Meth. A **480**, 524 (2002).

[43] G. Ascoli *et al.* (CDF Collaboration), Nucl. Instrum. Meth. A **268**, 33 (1988).

[44] G. Gomez-Ceballos *et al.*, Nucl. Instrum. Meth. A **518**, 522 (2004).

[45] E.J. Thomson *et al.*, IEEE Trans. Nucl. Sci. **49**, 1063 (2002).

[46] E. Sexton-Kennedy and P. Murat, in *Proceedings of 2003 Conference for Computing in High-Energy and Nuclear Physics (CHEP 03)* (La Jolla, California, 24-28 Mar 2003, pp THJT001); arXiv:physics/0306112.

[47] R. Brun *et al.* (ROOT Documentation Group), "ROOT - An Object-oriented Data Analysis Framework, users guide 5.16," (CERN, Geneva, Switzerland, 2007); http://root.cern.ch (accessed on April 25, 2008).

[48] C. Chen, I. Cho, C. Hays, M. Herndon, J. Kraus, J. Kroll, T. Miao, P. Murat, R. Oldeman, and J. C Yun, "Measurement of the Track Reconstruction Efficiency in the COT Using a MC Track Embedding Technique," CDF Report No. CDF-NOTE-6394, 2003 (unpublished).

[49] F. Abe *et al.* (CDF Collaboration), Phys. Rev. D **45**, 1448 (1992).

[50] A. Bhatti *et al.*, Nucl. Instrum. Meth. A **566**, 375 (2006); arXiv:hep-ex/0510047.

[51] A. Abulencia *et al.* (CDF Collaboration), Phys. Rev. D **75**, 092004 (2007).

[52] S.D'Auria, A.Dominguez, J.Nielsen, P.Murat, F.Prakoshyn, R.Snihur, R.Tafirout, A.Warburton, and D.Waters, "Run-Dependent MC Production for Summer 2004," CDF Report No. CDF-NOTE-7055, 2004 (unpublished).

[53] T. Sjöstrand *et al.*, Comput. Phys. Commun. **135**, 238 (2001); arXiv:hep-ph/0010017. We use PYTHIA version 6.216.

[54] S. Jadach, Z. Was, R. Decker, and J. H. Kuhn, Comput. Phys. Commun. **76**, 361 (1993).

[55] P. Avery, K. Read, and G. Trahern, "QQ: A Monte Carlo Generator," CLEO Software Note CSN-212 (1985); J. Lewis and P. Avery, "CLEOMC: The CDF Interface to the CLEO Monte Carlo (QQ)," CDF Report No. CDF-NOTE-2724, 1994 (unpublished).

[56] H. L. Lai *et al.* (CTEQ Collaboration), Eur. Phys. J. C **12**, 375 (2000); arXiv:hep-ph/9903282.

[57] R. Brun *et al.*, "GEANT3 User's Guide," CERN-DD-EE-81-1 (1989).

[58] A. Anastassov *et al.* (CDF Collaboration), Nucl. Instrum. Meth. A **518**, 609 (2004); arXiv:hep-ex/0312046.

[59] D. Acosta *et al.*, Nucl. Instrum. Methods A **494** (2002) 57; S. Klimenko, J. Konigsberg, and T. M. Liss, Fermilab Report No. FERMILAB-FN-0741 (2003).

[60] M. Chertok, J.P. Done, T. Kamon, Y. Kato, R. Oishi, A. Savoy-Navarro, and Y. Seiya, "Lepton + Track Trigger in Run II: A New Approach for Triggering on Dileptons: Electron Case," CDF Report No. CDF-NOTE-4807, 1998 (unpublished).

[61] J. Done, M. Chertok, T. Kamon, Y. Kato, R. Oishi, and A. Savoy-Navarro, "Lepton + Track Trigger for Run II: A New Approach for Triggering on Dileptons: Muon Case," CDF Report No. CDF-NOTE-5157, 1999 (unpublished).

[62] S. Baroiant *et al.*, "Update on the Lepton + Track Trigger in Run II: Definition and Physics Goals," CDF Report No. CDF-NOTE-6325, 2003 (unpublished).

[63] S. Baroiant *et al.*, "Measurement of the Electron Trigger Efficiencies for Level1 and Level2 8 GeV Triggers," CDF Report No. CDF-NOTE-6257, 2003 (unpublished).

[64] S. Baroiant *et al.*, "Measurement of Level3 Trigger Efficiency for 8 GeV Inclusive Electron Trigger Using Conversions," CDF Report No. CDF-NOTE-6324, 2003 (unpublished).

[65] S. Baroiant *et al.*, "Measurement of the Level 1 Trigger Efficiency for the Muon Plus Track Trigger," CDF Report No. CDF-NOTE-6358, 2003 (unpublished);

S. Baroiant *et al.*, "Level 1 and Level 3 Trigger Efficiency for the CMX Muon Plus Track Trigger," CDF Report No. CDF-NOTE-6760, 2003 (unpublished).

[66] S. Baroiant *et al.*, "Measurement of the Level 3 Trigger Efficiency for the Muon Plus Track Trigger (the CMUP case)," CDF Report No. CDF-NOTE-6621, 2003 (unpublished).

[67] S. Baroiant *et al.*, "XFT Efficiency for the Isolated Track Leg of the Electron+Track Trigger," CDF Report No. CDF-NOTE-6510, 2003 (unpublished).

[68] S. Baroiant *et al.*, "Lepton+Track Triggers: Measurement of the Level3 Trigger Efficiency for Taus," CDF Report No. CDF-NOTE-6553, 2003 (unpublished).

[69] W. Beenakker, R. Hopker, M. Spira, and P. M. Zerwas, Nucl. Phys. B **492**, 51 (1997); arXiv:hep-ph/9610490.

[70] J. Pumplin *et al.* (CTEQ Collaboration), J. High Energy Phys. **0207**, 012 (2002); arXiv:hep-ph/0201195.

[71] A. Abulencia *et al.* (CDF Collaboration), J. Phys. G **34**, 2457 (2007); arXiv:hep-ex/0508029.

[72] D. E. Acosta *et al.* (CDF Collaboration), Phys. Rev. Lett. **91**, 241804 (2003); arXiv:hep-ex/0307080.

[73] V. Martin, "High-Pt Muon ID Cuts and Efficiencies for Use with 5.3.1 Data and 5.3.3 MC," CDF Report No. CDF-NOTE-7367, 2005 (unpublished).

[74] S. Baroiant, M. Chertok, T. Kamon, V. Khotilovich, R. Lander, F. Ratnikov, and A. Safonov, "Measurement of Tau ID Efficiencies for the First 72 pb^{-1} of CDF Run II Data," CDF Report No. CDF-NOTE-7013, 2004 (unpublished).

[75] C. Hill, J. Incandela, and C. Mills, "Electron Identification in Offline Release 5.3," CDF Report No. CDF-NOTE-7309, 2005 (unpublished).

[76] T. Akimoto, S. Baroiant, A. Safonov, J.R. Smith, and A. Soha, "Electron ID Efficiencies for Intermediate p_T Using $\Upsilon \to e^+e^-$ Events," CDF Report No. CDF-NOTE-7713, 2005 (unpublished).

[77] V. Martin, "High p_T Muons, Recommended Cuts and Efficiencies for Release 5.3.1," CDF Report No. CDF-NOTE-7031, 2004 (unpublished).

[78] R. D. Field *et al.* (CDF Collaboration), in *Proceedings of APS / DPF / DPB Summer Study on the Future of Particle Physics (Snowmass 2001)* (Snowmass, Colorado, 30 Jun - 21 Jul 2001, pp P501); arXiv:hep-ph/0201192.

[79] A. Taffard, " Run II Cosmic Ray Tagger," CDF Report No. CDF-NOTE-6100, 2003 (unpublished).

[80] S. Baroiant *et al.*, "Energy Measurement for Hadronic Taus," CDF Report No. CDF-NOTE-6654, 2003 (unpublished).

[81] http://www-cdf.fnal.gov/physics/statistics/code/bayes.f (accessed on April 25, 2008).

[82] E. Halkiadakis, E. James, J. Kang, G. Manca, V. Martin, P. Murat, A. Robson, and M. Schmitt, "PDF Uncertainties for W and Z Cross Section Measurement," CDF Report No. CDF-NOTE-6890, 2004 (unpublished).

[83] O. Gonzalez and C. Rott, "Uncertainties Due to the PDFs for the Gluino-Sbottom Search," CDF Report No. CDF-NOTE-7051, 2004 (unpublished).

[84] M. Chertok, T. Kamon, V. Khotilovich, R. Lander, T. Ogawa, and A. Safonov, "Search for Pair Production of Stop Quarks Decaying to Tau and a B Jet," CDF Report No. CDF-NOTE-7312, 2004 (unpublished).

[85] M. Cacciari *et al.*, JHEP **0404**, 068 (2004); arXiv:hep-ph/0303085; N. Kidonakis and R. Vogt, Phys. Rev. D **68**, 114014 (2003); arXiv:hep-ph/0308222.

[86] J. M. Campbell and R. K. Ellis, Phys. Rev. D **60**, 113006 (1999); arXiv:hep-ph/9905386.

[87] S. Baroiant *et al.*, "γ+jet and W+jet Backgrounds to $Z/H \rightarrow \tau\tau$," CDF Report No. CDF-NOTE-6734, 2003 (unpublished).

[88] D. Glenzinski, M. Herndon, C.-J. Lin, J. Thom, and A. Yagil, "Run IIa COT Tracking Efficiency," CDF Report No. CDF-NOTE-5973, 2003 (unpublished).

[89] S. Sabik and P. Savard "Track Reconstruction Efficiency in Jets," CDF Report No. CDF-NOTE-6894, 2004 (unpublished).

[90] H. Georgi and S. L. Glashow, Phys. Rev. Lett. **32**, 438 (1974).

[91] H. Fritzsch and P. Minkowski, Annals Phys. **93**, 193 (1975).

[92] J. C. Pati and A. Salam, Phys. Rev. D **10**, 275 (1974); Erratum-*ibid.* D **11**, 703 (1975).

[93] I. Dorsner and P. Fileviez Perez, Nucl. Phys. B **723**, 53 (2005); arXiv:hep-ph/0504276.

[94] E. Farhi and L. Susskind, Phys. Rept. **74**, 277 (1981).

[95] K. D. Lane and M. V. Ramana, Phys. Rev. D **44**, 2678 (1991).

[96] B. Schrempp and F. Schrempp, Phys. Lett. B **153**, 101 (1985).

[97] V. M. Abazov *et al.* (DØ Collaboration), Phys. Lett. B **638**, 119 (2006); arXiv:hep-ex/0604029.

APPENDIX A

TAU IDENTIFICATION AND ITS EFFICIENCY

The $\tilde{t}_1\bar{\tilde{t}}_1 \to \tau_l\tau_h b\bar{b}$ search relies heavily on our ability to effectively reconstruct hadronically-decaying tau candidates. In order to do it we also need to reconstruct neutral pion candidates. In this Appendix we provide a detailed description of the reconstruction procedure and of the measurement of identification efficiency.

A. Tau and π^0 Identification

1. Hadronically-Decaying Tau Candidate Reconstruction

Hadronically-decaying tau candidates are reconstructed by matching calorimeter clusters with tracks and neutral pion candidates. The calorimeter cluster is required to have at least one tower with total energy $E_T > 5$ GeV, and the highest E_T tower in the cluster is called a seed tower. All adjacent towers with transverse energy deposition in excess of 1 GeV are added to the cluster. Only clusters consisting of six or fewer towers are retained for further reconstruction. This is because hadronically-decaying taus are expected to produce narrow jets. We allow tracks having reconstructed segments in at least two axial and two stereo COT segments that point to the tau calorimeter cluster to be associated with the hadronic tau candidate. The one with the highest p_T is selected as the seed track, which we require to have $p_T > 6$ GeV/c. If these requirements are satisfied, the cluster-track match becomes a hadronic tau candidate. Figure 30 [51] shows the efficiency of the hadronic tau reconstruction algorithm described above as a function of the true visible transverse momentum of a hadronic tau for $Z/\gamma^* \to \tau\tau$ events as obtained using PYTHIA MC.

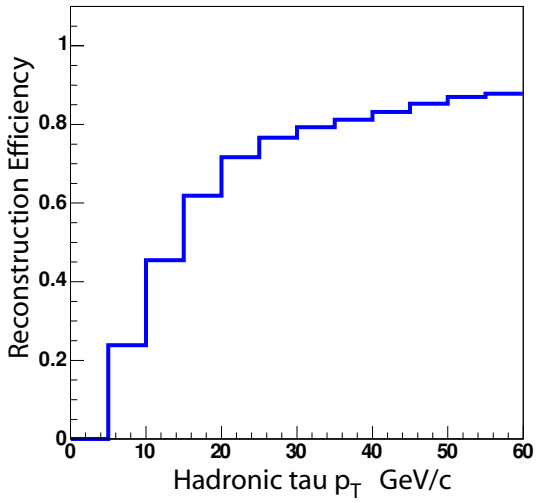

FIG. 30: Efficiency of the hadronic tau ($\tau_{\rm h}$) reconstruction as a function of the true visible (neutrino contribution excluded) transverse momentum of $\tau_{\rm h}$ for $Z/\gamma^* \rightarrow \tau\tau$ events as obtained using the PYTHIA MC and CDF II detector simulation. The efficiency is calculated for generated hadronic tau decays with $|\eta| < 0.9$.

With the initial tau candidate reconstructed, the algorithm associates additional tracks and reconstructed neutral pions (if found) with the tau candidate. The seed track is used to define signal and isolation cones. The track signal cone is defined as a cone with an opening angle $\alpha_{\rm trk}$ around the seed track:

$$\alpha_{\rm trk} = min[0.17, max(5\ {\rm GeV}/E^{\rm calo}, 0.05)]\ , \tag{A.1}$$

where $E^{\rm calo}$ is the energy (in GeV) of the calorimeter cluster associated with the tau candidate, and the other parameters are in radians. The energy dependence in the cone definition accounts for collimation of the decay products of highly boosted tau leptons; the lower bound on the cone size is driven by resolution effects. COT tracks in the signal cone that have (i) at least two axial and two stereo COT segments with at least 6 hits in each segment and (ii) z_0 compatible with that of the seed track ($|z_0^{\rm trk} - z_0^{\rm seed}| < 5$ cm) are assigned to the hadronic tau candidate. Tau decay modes

are classified by the number of "prongs," defined as the number of tracks with $p_T > 1$ GeV/c inside the track signal cone of a hadronic tau candidate.

Selected hadronic tau candidates are required to satisfy fiduciality requirements to ensure efficient reconstruction and triggering (Table IX). The tau seed track is required to be fully contained in the fiducial volume of the COT, and its trajectory extrapolation must point to a fully instrumented region of the CES detector in the z-direction, $9 < |z^{\mathrm{e-trk}}_{R_{\mathrm{CES}}}| < 230$ cm, to ensure efficient π^0 reconstruction.

2. Neutral Pion Candidate Reconstruction

Neutral pion candidates are reconstructed using clusters in the CES detector. Wire and strip CES energy depositions are clustered by starting with a seed wire or strip and combining up to five wires or strips into a cluster. Strip and wire clusters are matched to form 2D CES clusters. In cases where there are multiple reconstructed strip or wire clusters in a given CES segment, the matching is not unique, and the measured CES energy of the 1D clusters is used to identify which wire and strip clusters likely come from the same 2D cluster. A matched 2D cluster becomes a π^0 candidate if no COT track with $p_T > 1$ GeV/c is found nearby. If only one π^0 is found in a particular calorimeter tower, the π^0 is assigned the full EM calorimeter energy of this tower minus the expected deposited energy from all tracks traversing this tower:

$$E^{\pi^0} = E^{\mathrm{em}} - \sum_{\mathrm{trk}} (0.3\ \mathrm{GeV} + 0.21 \times p^{\mathrm{trk}}), \tag{A.2}$$

where p^{trk} is the magnitude of the momentum of the track. All energies are in GeV and momenta in GeV/c. The parametrization used in Eq. (A.2) is obtained from data by studying the calorimeter response to isolated charged pions. The constant term roughly corresponds to the energy deposition by a minimum ionizing particle, and

the slope accounts for the average energy deposition increase with the momentum of a particle. If there is more than one π^0 candidate in the same calorimeter tower, the EM calorimeter energy, after correction for energy deposited by charged tracks, is divided between them in proportion to their respective CES cluster energies.

Note that this algorithm makes no distinction between true π^0 mesons and photons, e.g. two photons from a sufficiently energetic π^0 meson ($E_T \geq 10$ GeV) are reconstructed as a single cluster, while for a lower momentum π^0 meson the algorithm typically finds two clusters, i.e. "resolved photons." Distinguishing between these two cases is not necessary for hadronic tau reconstruction since it has little effect on the measured parameters of a reconstructed tau candidate. Therefore, we take a "reconstructed π^0" to be either a true π^0 candidate or a single photon coming from either a $\pi^0 \rightarrow \gamma\gamma$ decay or from any other source.

3. Tau Candidate Identification Variables

For π^0's we define a π^0 signal cone around the seed track as

$$\alpha_{\pi^0} = 0.17 \text{ rad} . \tag{A.3}$$

All π^0 candidates with $E_T > 1$ GeV inside the π^0 signal cone that have matches in both the x- and z-views of CES are associated with the tau candidate.

The track and π^0 isolation regions are defined as annuli between the respective signal cones (Eqs. (A.1) and (A.3)) and the cone of

$$\alpha_{\text{ISO}} = 0.52 \text{ rad} \tag{A.4}$$

around the seed track. Figure 31 provides A schematic drawing of the $\tau \rightarrow 3\pi\gamma$ decay is shown in Fig. 31 as an example to illustrate signal and isolation cones.

Isolation plays an important role in tau identification as it is the most powerful

tool in rejecting QCD background. There are various ways to calculate tracking isolation. The first one is to define is as a sum of track momenta in isolation annulus as

$$I_{\rm trk}^{\tau\Delta\theta} = \sum_{\alpha_{\rm trk}<\Delta\theta<\alpha_{\rm ISO}} p_T^{\rm trk} \ . \tag{A.5}$$

And the second method is just to count the number of tracks with $p_T > 1$ GeV/c in isolation annulus, $N_{\rm trk}^{\tau\,\rm ISO}$. We use the second method because our signal events have rather strong jet activity and isolation requirement based on use of $I_{\rm trk}^{\tau\Delta\theta}$ would lead to lower signal acceptance. Note that only tracks with z_0 close to that of the seed track ($|z_0^{\rm trk} - z_0^{\rm seed}| < 5$ cm) are accounted in the isolation. In order to remove trigger bias we also use tracking isolation in annulus $0.17 < \Delta R < 0.52$, in which case we use a superscript ΔR in the corresponding isolation variable notations. In a similar way we define π^0 isolation:

$$I_{\pi^0}^{\tau\Delta\theta} = \sum_{\alpha_{\pi^0}<\Delta\theta<\alpha_{\rm ISO}} p_T^{\pi^0} \ . \tag{A.6}$$

For discriminating $\tau_{\rm h}$ candidates from electrons, a variable ξ is defined as

$$\xi = E_T^{\rm had} / \sum_{\tau\ tracks} p_T^{\rm trk} \ , \tag{A.7}$$

where $E_T^{\rm had}$ is the transverse energy of the tau candidate calculated using only hadronic deposition in the calorimeter. Electrons typically have small ξ, which allows substantial suppression of backgrounds with an electron faking a tau.

The visible mass of a tau candidate, $m^{\rm trk+\pi^0}$, is defined as the invariant mass of the tau momentum four-vector obtained in Eq. (A.9), before applying the correction for missed π^0's. The track mass of a tau candidate, $m^{\rm trk}$, is defined as the invariant mass of the track-only part of the tau momentum four-vector, Eq. (A.9). The charge

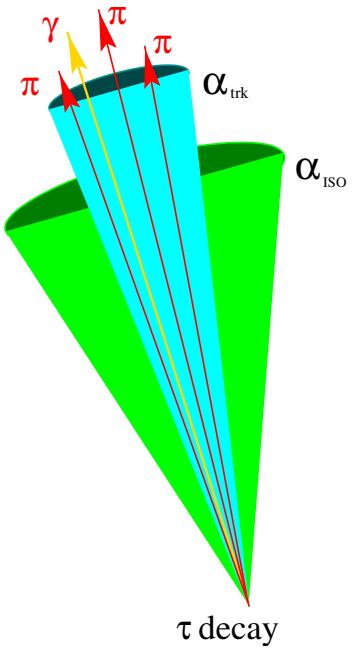

FIG. 31: Schematic representation of an example of τ 3-prong $\tau \to 3\pi\gamma$ decay and two cones used for τ identification: signal $\alpha_{\rm trk}$ cone and isolation $\alpha_{\rm ISO}$ cone.

of a tau candidate is defined as a sum of charges of the prongs associated with it:

$$Q^{\tau} = \sum_{\tau\ tracks} Q_{\rm trk}\ . \tag{A.8}$$

4. Tau Candidate Momentum

The energy of the tau candidate can be measured by using either the calorimeter information or the reconstructed tracks and π^0's. Due to the relatively poor energy resolution of the hadronic calorimeter, the latter is preferred. The four-vector momentum of a tau, p^{τ}, is defined as the sum of four-vectors of tau tracks with $p_T > 1$ GeV/c and π^0's with $E_T > 1$ GeV (both are assumed massless) associated with the tau candidate:

$$p^{\tau} \equiv \sum_{\Delta\Theta<\alpha_{\rm trk}} p^{\rm trk} + \sum_{\Delta\Theta<\alpha_{\pi^0}} p^{\pi^0}\ , \tag{A.9}$$

where p^{trk} and p^{π^0} denote four-vector momenta of contributing tracks and π^0 candidates, and $\Delta\Theta$ is the angle between the seed track and a particular track or π^0 candidate. Such momentum is often called as visible momentum of tau candidate as it does not include neutrino contribution.

Finally, a correction is applied to the hadronic tau energy, calculated above, that compensates for two effects: (i) inefficiency of π^0 reconstruction; and (ii) false π^0 reconstruction. While both of these effects are not predominant – in this analysis, the correction is invoked in approximately 10% of cases – they can result in substantial mismeasurement of a hadronic tau candidate energy. Such mismeasurement is undesirable not only for true hadronically-decaying taus, but also for the background jets or electrons misidentified as taus. In particular, false π^0 reconstruction can lead to promoting low energy hadronic jets or electrons misidentified as hadronic taus into the signal region.

The π^0 reconstruction inefficiency results in an underestimate of the tau candidate energy and is caused by either dead wires in the CES or the overlap of a π^0 meson with a track. When additional EM energy, not assigned to any of the π^0 candidates, is detected, the tau candidate energy is corrected by assuming the presence of an additional π^0 with an energy equal to the excess calorimeter energy, and a direction coinciding with the hadronic tau candidate.

For true hadronic taus, false π^0 reconstruction occurs when a charged hadron or an electron (from a photon conversion in $\tau \to \pi^0 + X \to \gamma\gamma + X$) deposits a large fraction of its energy in the EM calorimeter. If particle generates a wide shower in the CES, the shower size may exceed the five-strip/wire limit for 1D CES clusters and thus be split into two clusters. In this case, the cluster closer to the charged particle is not considered a π^0 candidate, since it is close to a track. The other CES cluster is reconstructed as a π^0 candidate with an energy nearly equal to the full EM

energy deposit in this tower leading to an overestimate of the hadronic tau energy. The same effect occurs when a hadronic jet or an electron from electroweak boson decay is misidentified as a hadronic tau promoting backgrounds to higher energies. In the case of electrons misidentified as taus, false π^0 reconstruction can lead to an overestimate of the hadronic tau candidate energy by up to a factor of two, since the same energy is counted both from the track and from the CES cluster. In cases where most of the tau energy is deposited in the EM calorimeter and there is significant disagreement between the calorimeter measurement and the calculation based on tracks and neutral pions, neutral pions (indicating double-counting of the EM energy in the p_T^τ calculation), p_T^τ is given by the calorimeter only.

B. Measurement of the Efficiency of Tau Identification Criteria

When we apply tau identifications requirements from Table XV to our signal MC sample we need to know how good is the correspondence between the efficiencies in data and the efficiencies in MC. The scale factor of 1.00 ± 0.03 used in Table XV is the result of such study, and below we discuss the details of that measurement.

1. Samples and Event Selection

For the measurement we used the following data and MC samples:

- Z-like set:
  - Lepton+Track dataset of 72 pb^{-1} (*etau*08 and *etlp*08);
  - PYTHIA MC $Z/\gamma^* \to \tau_e \tau_{\rm h}$ Pythia (*zewk*2*t*);
  - PYTHIA MC $Z/\gamma^* \to ee$ (*ztop*0*e*);
- W-like set:

– 72 pb^{-1}dataset collected by TAU_MET trigger;

– PYTHIA MC inclusive $W \rightarrow \tau\nu$ ($wewk4t$);

– PYTHIA MC $W \rightarrow e\nu$ ($wewk0e$).

Event selection for Z-like samples consisted in applying the geometrical and kinematical requirements for electron and tau (Table IX), electron candidate selection (Table XIII), and applying tau identification requirements as listed in Table XXXIV. We suppress conversions in the same way as it was discussed in Section IV.C.6.a. After that in order to suppress W + jets and QCD backgrounds, we have two additional requirements. The first one is on the transverse mass of electron and missing transverse energy, $m_T(e, \not\!\!E_T)$, to be $m_T(e, \not\!\!E_T) < 25$ GeV/c^2, and the second one is on the transverse momentum of electron and missing energy:

$$p_T(e, \not\!\!E_T) \equiv |\vec{p}_T^{\,e} + \vec{\not\!\!E}_T| > 25 \text{ GeV}/c. \tag{A.10}$$

TAU_MET trigger already requires $\not\!\!E_T > 25$ GeV and a tau candidate with $p_T > 25$ GeV/c. To improve selection of $W \rightarrow \tau\nu$ events by raising $\not\!\!E_T$ requirement to $\not\!\!E_T > 30$ GeV and requiring no other jets reconstructed with cone $\Delta R = 0.7$. (Table XXXV). It considerably suppresses QCD background. We use tighter electron rejection cut: $\xi^\tau = E_T^{had}/\Sigma {p_T}^{\text{trk}} \geq 0.2$, as $W \rightarrow \tau\nu$ sample is strongly contaminated with $W \rightarrow e\nu$ background, and require $p_T^\tau > 25$ GeV/c. In Figure 32 we show the distribution for number of tracks in a tau candidate. Such selection provides us with a "clean" sample of energetic taus.

2. Tracking and π^0 Isolation

We found that certain tau cuts are not well described by MC with the discrepancy especially pronounced for lower p_T taus. The cuts in question are related to the mod-

TABLE XXXIV: $\tau_{\rm h}$ identification cuts.

Seed Track: 3×3 ax/st SL's of 6 hits/SL
$d_0^{\tau-\rm trk} < 0.2$ cm
$\xi^\tau = E_T^{\rm had}/\Sigma {p_T}^{\rm trk} \geq 0.10$
$m^{\rm trk+\pi^0} \leq$2.5 GeV
$m^{\rm trk} \leq$1.8 GeV
$I_{\rm trk}^{\tau,\,\Delta\Theta} \leq 1{\rm GeV}/c$
$I_{\rm trk}^{\tau,\,\Delta R} \leq 1{\rm GeV}/c$
$I_{\pi^0}^{\tau,\,\Delta\Theta} \leq 0.6{\rm GeV}/c$
$N_{\rm trk}^{\tau\,\rm cone}$ =1 or 3

eling of the (hadronic) showering in the calorimeter and special features of calorimeter clustering used in tau reconstruction. Examples of such cuts are calorimeter isolation and the lateral profile of tau showers. Data suggests that showers are on average wider than predicted by MC. For this reason, we do not use cuts on tau calorimeter isolation $I_{\rm calo}^\tau < 6$ GeV, instead using track and π^0 isolations that we believe are more reliable.

We measure track and π^0 isolation efficiencies directly from the $Z{\rightarrow}ee$ data and MC samples and correct for small differences due to tau track and π^0 contamination of the isolation cone. To obtain a $Z{\rightarrow}ee$ sample we perform selection in the same way at for $Z{\rightarrow}\tau\tau$, but we reverse the anti-electron requirement for tau. We apply all the requirements except isolation and then measure the ratio of the "N$-$1" efficiencies of the isolation cuts in data to MC. The efficiency of the isolation cuts primarily depends on how well MC simulates the underlying event (UE). Another effect is that

TABLE XXXV: Event topology cuts for selection of "clean" $W \to \tau\nu$ events. The number 0.7 refers to jets reconstructed with cone $\Delta R = 0.7$.

$\not\!\!E_T$:	$\not\!\!E_T > 30$ GeV
0.7-Monojet:	$E_T > 25$ GeV
	$\lvert\eta_{det}\rvert < 1.2$
Veto other 0.7 jets:	$E_T > 5$ GeV
	$\lvert\eta_{det}\rvert < 10$

additional min-bias interactions are not simulated at all, and it can give a contribution not predicted by MC. Therefore, we choose to assign any observed difference between data and MC to this effect and apply a scale factor. Regarding π^0 isolation, we do expect differences due to inaccurate simulation of CES in MC. The π^0 reconstruction efficiency in data is lower than in MC, therefore we treat any difference that we observe as a correction. We also did check that isolation efficiencies measured in $Z \to ee$ events are similar to those in $Z \to \tau\tau$ events. Overall, the agreement between data and MC is quite good, and the correction factors are 0.995 ± 0.017 and 1.003 ± 0.005 for track and π^0 isolation efficiencies respectively, and one can conservatively use the difference as a systematic uncertainty.

3. Number of Charged Tracks

We then obtain a correction to the efficiency of the requirement of only 1 or 3 tracks for $\tau_{\rm h}$, $N^{\tau}_{\rm trk} = 1, 3$. The physics part of this inefficiency is due to one of the tau tracks happenning to have $p_T < 1$ GeV/c, and not being counted. This effect should be well simulated in MC. However, remaining "instrumental" inefficiency can exist due to tracks from UE and extra minbias interactions accidentally falling into the signal

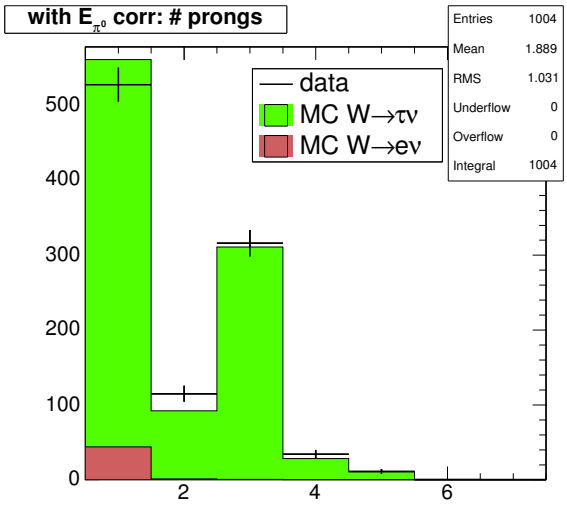

FIG. 32: Distribution for the number of prongs in a tau candidate in the "clean" $W \to \tau\nu$ sample. The only considered background is $W \to e\nu$. The $W \to \tau\nu$ MC is normalized to data minus $W \to e\nu$ MC.

cone. We estimate this effect by comparing the fraction of 2-prong tau candidates (electrons passing as taus) between $Z \to ee$ data and MC samples. If we assume that the difference is due to tracks from UE and secondary min-bias interactions, we can estimate the additional fraction of events that will migrate from 1 and 3 prong bins into even prong bins and compensate for this unaccounted by MC loss by applying the following scale factor to the efficiency of this cut:

$$f^{\text{min-bias}} = \frac{1}{(1 + N_{n=2}^{Z\to ee\ Data}/N_{n=1}^{Z\to ee,\ Data} - N_{n=2}^{Z\to ee\ MC}/N_{n=1}^{Z\to ee,\ MC})} , \qquad (A.11)$$

where n stands for the number of tracks in the signal cone of a tau candidate. However, this is likely an overestimation as the $Z \to ee$ data can have backgrounds that are partially responsible for this increase (e.g. bremstrahlung followed by a conversion escaping conversion filter). Also, description of the track isolation efficiencies suggests that this could be an upper bound on the deviation of data from MC. Thus,

we conservatively use a scale factor of 1.0 and assign a (very) conservative systematic uncertainty to be equal to the correction itself, $f^{\mathrm{min-bias}} = 1.00 \pm 0.02$. The intermidiate numbers are: fraction of events with an electron passing as a 2-prong tau candidate in data is 4.7% while MC predicts 2.7%.

Another possible effect that is important for the $N^{\tau}_{\mathrm{trk}} = 1, 3$ requirement is migration of events from 3-prong bin into the excluded 2-prong bin due to effects of track reconstruction efficiency. Estimation of this effect can probably be best made by embedding tau tracks into real events. At this time we do not have such estimation available, and we use default MC prediction for such migration and assign an uncertainty of 0.5% per track based on several available studies of tracking performance [48, 88, 89]. With two tracks that can be independently lost or misreconstructed (reconstruction efficiency for the seed track is accounted earlier), we arrive to a 1% uncertainty.

We use a total uncertainty of 2.9% that we assign to the effects associated with the number of tracks requirement.

4. Track Quality and Impact Parameter

For the tau seed track quality requirement and the impact parameter $d_0^{\tau-\mathrm{trk}}$ requirement we found using $Z \rightarrow ee$ events that the corerction factor is consistent with one.

5. Anti-Electron ξ Requirement

To estimate the systematic uncertainty associated with the anti-electron ξ requirement, we consider two possible sources for uncertainty: imprecise knowledge of the hadronic calorimeter energy scale and imperfect MC predictions of the fraction of charged hadrons showering early (in the EM calorimeter). For the first cause, we simply vary the value of this cut from $\xi_{min} = 0.094$ to $\xi_{max} = 0.106$, which corre-

sponds to a change in the hadronic scale in MC by 6%. We find the largest deviation to be around 0.4%, which we assign as a part the systematic uncertainty associated with this cut. This second issue is more complicated and required a more detailed study. Starting with electron+track and muon+track data, we obtain a sample of relatively pure 1-prong taus, and compare the ξ-cut efficiency to MC taus with an identical p_T distribution. The details of such selection are available in Ref. [74]. The resulting scale factor for the $\xi > 0.1$ requirement is found to be $0.995 \pm 0.013(\text{stat}) \pm 0.018(\text{syst})$.

6. Tau Mass

To measure the efficiency of the tau candidate mass requirement we use our "clean" $W \rightarrow \tau\nu$ sample. We apply all the selection criteria to the data and MC samples except the cuts on m^{trk} and $m^{\text{trk}+\pi^0}$, and then study the efficiency for various cut values. The $m^{\text{trk}+\pi^0}$ shows disagreement of data and MC for low and mid-values of the mass. There are two effects contributing to it: the first is that usually we get more π^0s reconstructed in MC; and the second is that when we apply tau energy correction to compensate for the lost π^0s we don't use it in calculation of tau visible mass. The mass requirements were set intentionally loose and approaching full efficiency. The result for the $m^{\text{trk}+\pi^0} \leq 2.5$ GeV/c^2 and $m^{\text{trk}} \leq 1.8$ GeV/c^2 requirement is 0.996 ± 0.004.

7. $N_{\text{tow}} \leq 6$ Requirement for Tau Cluster

We also studied the effect of the requirement that tau candidate's calorimeter cluster should have six or less towers with tower energy of $E_T > 1$ GeV. In data lateral profiles of hadronic showers are wider, and therefore one should expect a larger average number of towers in tau candidates than in MC. To model wider showers in MC we build a model that simulates on average the actual process: we use MC $Z \rightarrow \tau\tau$ events and for each tower in tau candidate cluster we assign a fraction f_E of the tower energy

to one of the four surroudning towers (no matter if it is a part of the tower or not) with a probability p_E. We perform this for all towers in the cluster only once and we do not re-assign the once assigned additional energy again. Then we count the number of towers in tau clusters and fit it to the distribution observed in data for different values of f_E and p_E. The result is χ^2 as a function of f_E and p_E. We find that the minimum of χ^2 occurs when $f_E = 0.37$ and $p_E = 0.23$. To estimate the systematic uncertainty we estimate the fraction of the number of events failing $N_{\rm tow} \leq 6$ cut. Thus, the scale factor for this additional loss of events due to imperfectness of MC is found to be about $1.005 \pm 0.005(syst)$.

8. Tau Identification Efficiency Summary

The summary of this study is presented in Table XXXVI.

TABLE XXXVI: Efficiency of tau ID cuts. We quote MC predictions based on $Z \to \tau\tau$ analysis and quote corresponding scale factors.

Cut	MC Efficiency [%]	Scale Factor
Seed Track Quality	97.9 ± 0.3	1.0
$d_0^{\tau-\text{seed}} < 0.2$ cm	97.6 ± 0.4	1.0
$\xi > 0.1$	91.3 ± 0.7	0.995 ± 0.022
$m^{\text{trk}} \leq 1.8$ GeV/c^2 & $m^{\text{trk}+\pi^0} \leq 2.5$ GeV/c^2	99.3 ± 0.2	0.996 ± 0.004
$I_{\text{trk}}^{\tau,\,\Delta\Theta} \leq 1$ GeV/c& $I_{\text{trk}}^{\tau,\,\Delta R} \leq 1$ GeV/c	75.0 ± 1.1	0.995 ± 0.017
$I_{\pi^0}^{\tau,\,\Delta\Theta} \leq 0.6$ GeV/c	96.1 ± 0.6	1.003 ± 0.005
$N_{\text{trk}}^{\tau\,\text{cone}}$ =1 or 3	89.5 ± 1.0	1.000 ± 0.026
N_{tow} Correction		1.005 ± 0.005
Cumulative	55.9 ± 1.6	0.994 ± 0.039
Final Efficiency	$55.6 \pm 1.6(stat) \pm 2.2(syst)$	

APPENDIX B

MEASUREMENT OF THE EFFICIENCIES FOR THE LEPTON-PLUS-TRACK TRIGGERS

Triggering algorithms are simpler and faster than those used in offline reconstruction software. It makes the efficiency of event selection by trigger system with relation to event selection made with the offline reconstruction software (or simply trigger efficiency) less than 100%. Lepton plus track (LT) triggers are described in details in Section III.A and Section III.B has short discussion of their efficiencies. In this appendix we present more details on the trigger efficiencies.

LT triggers are constructed of two parts: lepton (electron or muon) leg and isolated track leg. The total efficiency is a product of the efficiencies for each part:

$$\epsilon = \epsilon^{l} \times \epsilon^{\mathrm{trk}} \ . \tag{B.1}$$

Here we neglect any possible correlation effects due to existence of the requirements on $|z_0(l) - z_0(trk)|$ and $\Delta R(l, trk)$ (see Tables III, IV, and V) that involve both, lepton and track legs. The efficiency for each leg is a product of the efficiencies for each level:

$$\epsilon^{l} = \epsilon^{l}_{L1} \times \epsilon^{l}_{L2} \times \epsilon^{l}_{L3} \ , \tag{B.2}$$

$$\epsilon^{\mathrm{trk}} = \epsilon^{\mathrm{trk}}_{L1} \times \epsilon^{\mathrm{trk}}_{L2} \times \epsilon^{\mathrm{trk}}_{L3} \ . \tag{B.3}$$

Note that the efficiency for some specific level (except L1) should be measured with respect to events that passed all preceding levels, as various trigger levels cut on essentially the same values, and therefore are highly correlated.

Section B.A presents details of the trigger efficiency measurement for the isolated track trigger leg. Sections B.B and B.C give the essential results of the trigger efficiency measurement for the electron and muon trigger legs respectively.

A. Efficiency for the Isolated Track Trigger Leg

From Tables III, IV, and V which summarize the requirements for LT triggers we see that the isolated track side is only used at L2 (for electron plus track trigger only) and L3 (for both, electron and muon plus track triggers). It means that we set the multipliers for unused levels in Eq. (B.3) equal to one.

The measurement of the L2 XFT trigger efficiency is presented in Section B.A.1, and Section B.A.2 describes an efficiency study for the isolated track trigger leg at L3.

1. Level 2 XFT Trigger Efficiency

The material of this section is based on the study documented in Ref. [67].

The isolated track side of the electron plus track trigger at level 2 is required to have a 4-layer XFT track with $p_T \geq 5.18$ GeV/c (Table III).

a. XFT and COT Features Affecting Trigger Efficiency

The description of XFT features is given in Section II.C. These special features of the XFT can greatly affect the trigger efficiency. For example, an XFT track can erroneously combine hits or segments from different tracks and (especially when several tracks are clustered together) can "create" and report a higher p_T track than actually exists. Also, since the ability of the XFT to build a track depends on the COT occupancy, the more active the COT is in some ϕ-slice, the more likely XFT is

to find a track at all. Thus, when there are lots of tracks, not only is the XFT more likely to reconstruct tracks, but it is more likely to have its reported tracks be high p_T, which makes it more likely to pass the trigger threshold.

There are also several effects on the efficiency associated with the mechanical design of the COT chamber. One geometry related effect is that the XFT performs worse for the low η tracks as the shorter path length inside of COT gives a smaller charge collected by wires and thus a lower probability to produce a hit. Also, at $z = 0$ (right in the middle of the detector), a special structure called "the spacer" supports the COT wires. When a track passes through the spacer, it is less likely to produce hits in the region of small z. In both cases since two lost hits can result in the segment not being reconstructed the whole XFT track will not be found, causing an η-dependent XFT efficiency. This becomes especially pronounced for low p_T tracks since low p_T particles produce weaker ionization, decreasing the probability of generating a COT hit, further decreasing the efficiency. We also note that the L2 trigger (see Table III) requires each XFT track to have four segments[1]. This also reduces the trigger efficiency, as well as defines the fiducial volume of the XFT/COT.

There are three time periods of XFT operation that are relevant for the data used in this analysis:

A) March 2002 – September 2002: "2-miss" configuration;

B) October 2002 – January 2003: "1-miss" configuration;

C) January 2003 – August 2004: "1-miss" configuration and lowered COT voltage.

Lower COT voltage causes smaller showers and smaller gains on the wires, leading to smaller signals and smaller probability of COT hit detection. Again, if two hits are

[1]Four is a maximal possible number, as there are four axial superlayers (numbered as SL2, SL4, SL6, and SL8).

lost at the same superlayer, the whole XFT track will not be reconstructed, resulting in a loss of efficiency.

b. Efficiency and Track Matching Definition

The main purpose of the track leg of the lepton+track trigger is that it can result in a reconstructed tau candidate, and we should take this into account when defining how we calculate the efficiency. The tracks from hadronically decaying taus are typically tightly clustered together. So, when doing tau identification, we require these sets of tracks to be isolated from other tracks in the event.

For the isolated track leg we define the XFT efficiency as

$$\epsilon_{L2}^{\text{trk}} = \frac{\text{number of good isolated tracks with a triggered XFT match}}{\text{number of good isolated tracks}}, \qquad \text{(B.4)}$$

where *good isolated tracks* means that we have applied certain quality cuts for offline tracks (see Section B.A.1.c), and *triggered XFT match* means that the track has a corresponding XFT track which passed the trigger cuts.

The matching is of particular concern here because we expect the track to become a seed of a reconstructed tau candidate. Let's first consider matching of a single offline track to a single XFT track. If we had access to the information about the XFT track's hits, then we would be able to check if the fraction of hits it shares with the original track is significant. Unfortunately, it is not possible as trigger data banks do not keep this information. Also, as described in Section B.A.1.a, due to XFT particularities, an offline track could have an XFT "partner" with a dissimilar set of helix parameters. Therefore, it is better to think about the XFT efficiency as the "probability that the presence of a given track triggers the XFT," which is dependent on the density of COT hits. This method works well for electrons and muons, but for taus, which can have several tracks, another approach is better. Now we ask the

question "was there any XFT track which could have triggered the event for a given tau?" Exact matching is not needed here, as the tau could have several tracks. For these reasons we developed the following matching procedure for taus:

1. count the number of prongs (tracks with $p_T > 1$ GeV/c in a 3D 10° cone) for every track which passes the quality cuts;
2. check every track to see if it is the seed track (has the highest p_T in the cone);
3. for the seed track, look for a triggered XFT track in the corresponding 2D 10° sector;
4. we have a match if any XFT track is found.

The number of prongs in our "tau" is used later as a convenient measure of COT activity and to classify the efficiency accordingly.

c. Datasets and Offline Track Selection

For measuring the XFT trigger efficiency we created three data samples which correspond to the periods of XFT operation mentioned in Section B.A.1.a. We used events from jet datasets, choosing good high statistics runs and requiring at least one electron object with loose electron requirements (default EmObject cuts). This data does not have any bias from XFT triggers.

To select offline tracks we apply additional quality and fiduciality requirements to ensure that track can be expected to trigger the XFT if the XFT system is fully efficient. Table XXXVII presents both requirements as well as the track based tau ID emulation cuts (seed and isolation requirements) that we have used for offline track selection. We assume that the electron and tau legs of the trigger are independent. However, we use some of the L3 cuts here, including the electron-track topology requirements to select events which better resemble the targeted physics signal. Also,

TABLE XXXVII: Offline track selection cuts. $r_{2(8)}$ is the radius of the center of the first (last) axial superlayer. $\Delta\Theta$ denotes a 3D angle around the seed track (as in a standard $\tau_{\rm h}$ reconstruction).

Track quality cuts:	$p_T > 3$ GeV/c; $\|\eta\| \leq 1.5$; $N_{axialCThits} \geq 25$, $N_{stereoCThits} \geq 25$; $\|d_0^{\rm cor}\| < 0.2$ cm;
fiducial region for XFT requirements:	$\|z_{\rm COT}(r = r_2)\| < 150$ cm, $\|z_{\rm COT}(r = r_8)\| < 150$ cm;
seed track requirement:	has the highest p_T among the tracks within $\|\Delta z_0\| < 15$ cm in its 10° cone;
tau-like isolation, two cases:	1) no tracks with $p_T > 1.5$ GeV/c and $\|z_0({\rm seed}) - z_0({\rm trk})\| < 15$ cm within the cone $10^\circ < \Delta\Theta < 30^\circ$ around the seed track; 2) in addition to 1) no tracks with $p_T > 1.5$ GeV/c within the segment $\Delta\phi < 10^\circ$ around the seed track except for those in the 10° tau-cone;
electron partner requirement cuts:	$\|z_0(e) - z_0({\rm trk})\| \leq 15$ cm; $\Delta R(e, {\rm trk}) \geq 0.175$.

we repeat the efficiency calculation for a sample with no requirement of a partner electron. This "unbiased" sample has larger statistics, serves as a cross-check to verify the assumption of the two trigger legs (electron and track) being uncorrelated, and helps give a handle on the systematic uncertainties in our measurement.

We note that the COT environment for jet data is in general busier then for typical events which pass the electron plus track trigger. We don't want to overestimate our efficiency, so we use different types of isolation. This is also is helpful for the estimation of the systematic error. In our study we use the 3D tau-like offline track isolation (the same as in the L3 electron plus track trigger) and we check the case of an additional 2D isolation requirement in the segment $\Delta\phi < 10^\circ$ excluding the $\Delta\Theta < 10^\circ$ tau-cone as it helps to estimate a lower bound or "pure" XFT efficiency. Such ad-

ditional isolation ensures that the XFT, which works in two dimensions, deals only with tracks from our 10° tau-cone inside the $\Delta\phi < 10°$ segment. Also, this requirement automatically satisfies the L2 "other" requirement in Table III. We consider this efficiency as a lower bound for the efficiency: the fewer hits there are in some COT segment, the harder is the track reconstruction task for the XFT.

d. Results

We parametrize the XFT efficiency as a function of $1/p_T$ and as a function of $1/p_T$ and η for different number of prongs and time periods. Since real tau seed tracks may have a slightly different η distribution then our efficiency sample, having η-dependent parametrization is necessary. We also note that the averaged out η-dependence is also useful, as it allows direct comparison of the samples, makes it more easy to observe basic trends and gives a possibility to check if our efficiency parametrization in two dimensional ($1/p_T$ vs. η) space is good.

The $1/p_T$ only parametrization of the efficiency for the time period A is

$$\epsilon(1/p_T) = K_\infty \times freq\left(\frac{1/p_{T_0} - 1/p_T}{2\sigma_{1/p_T}}\right), \tag{B.5}$$

where p_T is the transverse momentum of the seed track, K_∞ is the asymptotic limit of the efficiency, p_{T_0} is the middle of the turn-on region and σ_{1/p_T} is the XFT curvature resolution.

For data for which the XFT allowed only one missing hit (samples B and C), the trigger efficiency acquires a non-negligible p_T dependence at high p_T. This can be parametrized by introducing a forth parameter, S, and the parametrization:

$$\epsilon(1/p_T) = (1 - S\,(1/p_T - 1/10)) \times K_{10} \times freq\left(\frac{1/p_{T_0} - 1/p_T}{2\sigma_{1/p_T}}\right), \tag{B.6}$$

where S is the slope of the efficiency at high p_T and K_{10} is the efficiency at $p_T = 10$

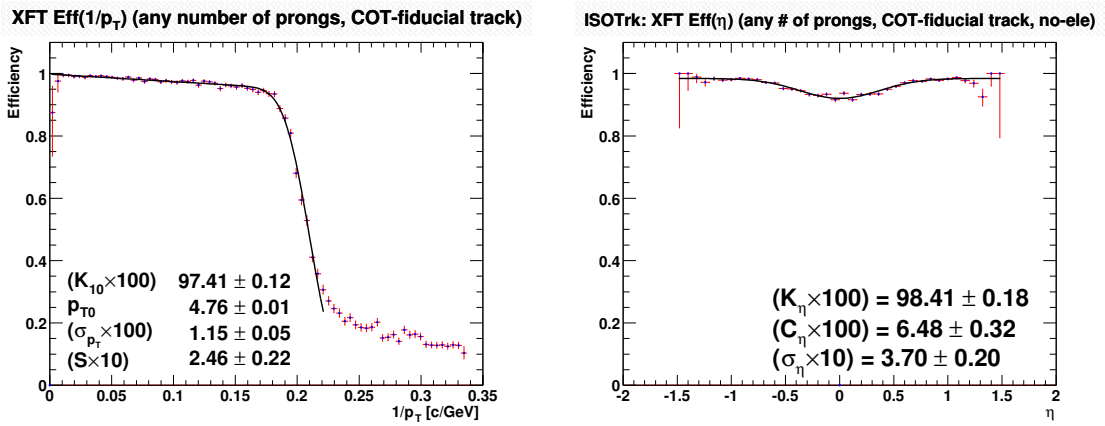

FIG. 33: The XFT track trigger efficiencies as a functions of $1/p_T$ (left, using Eq. (B.6)) and η (right, using Eq. (B.7)) for any number of prongs track with 3D-tau-like isolation and a requirement of an additional electron in data from time period C ("1-miss," lowered COT voltage). The $\epsilon(1/p_T)$ dependence shows noticeable slope in high-p_T region. For the $\epsilon(\eta)$ dependence the minimal offline track p_T is chosen to be 5 GeV/c, and the noticeable inefficiency in the center is due to the central COT spacer.

GeV/c. We have chosen this parametrization because K_{10} can be directly compared to the parameter K_∞ of the 3-parameter fit while parameters S and K_{10} remain almost uncorrelated. Figure 33 shows an example of a fit using Eq. (B.6).

As discussed in Section B.A.1.a, due to the COT geometry, the XFT efficiency also depends on η. We use a 3-parameter Gaussian-like parametrization of the efficiency to take this dependence in account:

$$\epsilon(\eta) = K_\eta \times \left(1 - C_\eta \exp\left(-\frac{\eta^2}{2\sigma_\eta^2}\right)\right), \tag{B.7}$$

where C_η and σ_η are the Gaussian height and width, respectively. Figure 33 shows an example of such a fit and demonstrates an inefficiency at low η. We note that the depth of the dip depends on the p_T of the tracks contributing to the sample, being smaller for higher p_T tracks and larger for soft tracks. To properly account for these

effects we use the following parametrization:

$$\epsilon(1/p_T, \eta) = K_\infty \times freq\left(\frac{1/p_{T_0} - 1/p_T}{2\sigma_{1/p_T}}\right) \times \left(1 - C_\eta \times 1/p_T \times \exp\left(-\frac{\eta^2}{2\sigma_\eta^2}\right)\right) \quad \text{(B.8)}$$

If compared to Eq.(B.6), one may note that the effective slope is still present but now is part of the η-dependent gaussian portion.

The detailed results are available in Ref. [67]. Here we only present the essential result in summary Table XXXVIII which we use in our analysis.

2. Efficiency for the Isolated Track at Level 3

The material of this section is based on the study documented in Ref. [68].

The L3 isolated track leg requirements are the same for all LT triggers: $p_T \geq 5$ GeV/c; $|\eta| \leq 1.5$; and the isolation requirement of no track with $p_T > 1.5$ GeV/c and $|\Delta z_0| < 15$ cm in $0.175 \leq \Delta R \leq 0.524$ (Tables III, IV, and V).

a. Datasets and Tau Selection

For the measurement we used a dataset of events collected from jet triggers. The jet triggers use calorimeter information only, while LT triggers use exclusively tracks. Therefore the jet sample is not correlated with the LT sample.

For pre-selection, we required at least one loose tau candidate with $p_T^{\text{seed}} > 4$ GeV/c and $m^{\text{trk}+\pi^0} < 3$ GeV/c^2. After such selection we drop all high-level objects, re-run L3 executable and then run Production again to have both L3 and offline reconstructed objects.

For the final efficiency measurement, we used events with high quality tau candidates by applying a set of requirements summarized in Table XXXIX which are close to the standard tau quality cuts (Tables IX and XV). Note that despite of rather strict requirements the sample still consists of mainly jets misidentified as taus.

TABLE XXXVIII: Results of the 5-parameter (Eq. (B.8)) fit of the XFT track trigger efficiency for different time periods (Section B.A.1.a) for the case when we require only 3D track isolation and require an additional electron. We also give estimates of the parameter systematic uncertainties (marked with *sys* superscript) calculated as unbiased variance over different requirements for electron and isolation. K_∞ is measured in %, p_{T_0} in GeV/c , σ_{pT0} in $(100 \times \text{GeV}/c)^{-1}$, C_η in $(0.1 \times \text{GeV}/c)$ and σ_η in $0.1 \times$ (*inversed units of rapidity*).

Time period		number of prongs				
		1	2	3	4	5
A	K_∞	$99.84^{+0.16}_{-0.37}$	$99.99^{+0.01}_{-0.85}$	$99.90^{+0.10}_{-0.18}$	99.87±0.13	$99.92^{+0.08}_{-0.11}$
	p_{T_0}	4.75±0.02	4.70±0.02	4.59±0.04	4.47±0.06	4.40±0.09
	σ_{pT0}	0.94±0.06	1.06±0.09	1.18±0.14	1.34±0.21	1.33±0.29
	C_η	3.64±0.82	2.70±0.77	1.04±0.52	1.61±0.86	1.22±0.79
	σ_η	3.01±0.57	2.76±0.63	3.56±1.57	1.99±0.65	2.44±0.88
	${\Delta K_\infty}^{sys}$	±0.09	±0.11	±0.09	±0.06	±0.04
	${\Delta p_{T_0}}^{sys}$	±0.02	±0.02	±0.02	±0.04	±0.04
	${\Delta \sigma_{pT0}}^{sys}$	±0.04	±0.03	±0.11	±0.08	±0.10
	${\Delta C_\eta}^{sys}$	±0.48	±0.23	±0.36	±0.33	±0.26
	${\Delta \sigma_\eta}^{sys}$	±0.18	±0.14	±0.49	±0.52	±0.26
B	K_∞	98.93±0.73	98.78±0.62	99.00±0.54	99.57±0.41	$99.85^{+0.15}_{-0.23}$
	p_{T_0}	4.88±0.02	4.81±0.02	4.75±0.03	4.62±0.04	4.58±0.06
	σ_{pT0}	0.86±0.06	1.03±0.09	1.10±0.12	1.28±0.17	1.31±0.21
	C_η	9.03±1.19	6.66±1.13	6.79±1.21	4.12±1.04	2.06±0.85
	σ_η	3.55±0.46	3.31±0.59	3.43±0.63	3.87±0.81	3.72±1.61
	${\Delta K_\infty}^{sys}$	±0.39	±0.07	±0.09	±0.25	±0.12
	${\Delta p_{T_0}}^{sys}$	±0.01	±0.02	±0.00	±0.02	±0.02
	${\Delta \sigma_{pT0}}^{sys}$	±0.04	±0.02	±0.06	±0.06	±0.03
	${\Delta C_\eta}^{sys}$	±0.68	±0.48	±0.29	±0.05	±0.27
	${\Delta \sigma_\eta}^{sys}$	±0.17	±0.31	±0.18	±0.22	±0.32
C	K_∞	98.09±0.75	98.84±0.49	$99.75^{+0.25}_{-0.46}$	99.48±0.29	99.63±0.21
	p_{T_0}	4.88±0.01	4.81±0.02	4.75±0.02	4.63±0.04	4.43±0.08
	σ_{pT0}	0.93±0.05	1.01±0.07	1.19±0.10	1.50±0.17	1.88±0.32
	C_η	8.95±1.03	6.48±0.94	5.20±0.77	3.82±0.87	2.22±0.87
	σ_η	3.28±0.42	3.52±0.42	4.41±0.83	3.38±0.68	2.82±0.82
	${\Delta K_\infty}^{sys}$	±0.26	±0.28	±0.21	±0.15	±0.11
	${\Delta p_{T_0}}^{sys}$	±0.02	±0.02	±0.02	±0.02	±0.06
	${\Delta \sigma_{pT0}}^{sys}$	±0.06	±0.01	±0.02	±0.08	±0.24
	${\Delta C_\eta}^{sys}$	±0.85	±0.13	±0.59	±0.33	±0.79
	${\Delta \sigma_\eta}^{sys}$	±0.11	±0.19	±0.30	±0.40	±0.17

TABLE XXXIX: Offline τ quality cuts.

· Seed Tower $E_{\rm T} > 6$ GeV
· Seed Track $p_T > 4$ GeV/c
· Seed Track $\lvert z_0\rvert < 60$ cm
· $\lvert z_0(\text{seed}) - z_0(\text{closest primary vertex})\rvert < 5$ cm
· Seed Track $\lvert d_0^{cor}\rvert < 0.1$ cm
· $CalIso < 6.0$ GeV
· ${p_T}^{\rm vis} \geq 4$ GeV/c
· $\lvert\eta\rvert \leq 1.0$
· $m^{\rm trk+\pi^0} < 1.8$ GeV/c^2
· $\xi \equiv E_{\rm T}^{\rm had}/\Sigma\lvert{p_T}^{\rm trk}\rvert > 0.1$
· No track with $p_T > 1.0$ GeV/c in isolation annulus
· No π^0 with $E_T > 0.5$ GeV in isolation annulus
· Fiducial for Seed Track
$9 \leq \lvert z_{\rm CES}(r = 183.9 \text{ cm})\rvert \leq 230$ cm
$\lvert z_{\rm COT}(r = 183.9 \text{ cm})\rvert \leq 150$ cm
$N_{\text{axial SL}}, N_{\text{stereo SL}} \geq 3$
· Fiducial in terms of L3 isolation
No track with $p_T > 1.0$ GeV/c and $\lvert\Delta z_0\rvert < 15$ cm
in $0.175 \leq \Delta R \leq 0.524$ around the seed track

The efficiency depends on how well it is possible to match Level 3 isolated track to the offline tau. We adopted a very simple prescription for the matching: the isolated track must be inside of the tau signal cone, and $|\Delta z|$ between the track and the tau seed track is less then 15 cm.

b. Major Sources of Inefficiency

We found several important effects that cause L3 to fail a seemingly good offline tau candidate.

First, there are effects of angular resolution when an offline track is reconstructed by L3 with a slightly different angular parameters. For relatively "wide" tau candidates it may lead to one of the tau tracks fall outside the signal cone defined by the

seed track. If that happens, the formerly tau track becomes a background track and the event is vetoed by L3. We define a variable $\Delta\theta^{\text{in}}$ as the minimum angle in θ out of all tracks in the L3 signal cone of the tau candidate and the boundary of the signal cone[2]. The closer the track is to the boundary, the higher is the probability of the event to fail L3 trigger. The beauty of this variable is that it represents the track "resolution" in θ and is independent of η of the detector. Also, the measurement will apply to any size of the signal cone.

Another effect is related to L3 curvature resolution with respect to the offline. We break this effect into two pieces. In the first case, the seed track p_T sometimes can fluctuate below the L3 threshold of 5 GeV/c. This affects the resolution of the turn-on curve as a function of the seed track transverse momentum, p_T^{-1}. Second effect is related to the soft background tracks in $0.175 < \Delta R < 0.524$ being promoted by L3 to exceed the threshold of 1.5 GeV/c, at which point such track will violate the isolation requirement and the event will be vetoed. This effect is less trivial as it depends on the number of soft tracks in the isolation region and also has a non-linear contribution when many hits from these tracks can confuse L3 and make it combine unrelated hits into a new track with p_T above the threshold. We found that tracking isolation defined as a scalar sum of all COT tracks inside the cone $0.175 < \Delta R < 0.524$, called $\Sigma^{\text{iso}}p_T$, is a good variable to parameterize this effect.

Furthermore, as tau candidates are essentially jets with tracks being close to each other, these tracks often overlap and have common hits complicating pattern recognition. These effects are always difficult to quantify. We chose to use the number of prongs in the tau candidate as a measure of the COT activity. The number of prongs might not be the best variable to account for pattern recognition effects, but

[2]The considered tracks all have $p_T > 1.5$ GeV/c, and $|\Delta z| < 15$ cm from the seed track.

it is a natural variable for taus, which determined our choice.

There are a number of less prominent effects affecting the efficiency that we noticed but chose to ignore in the final parameterization to avoid over-complicating things.

c. Efficiency Definition

In Section B.A.2.b we found that the following variables contribute independently to the overall efficiency: $\Delta\theta^{\text{in}}$, tracking isolation $\Sigma^{\text{iso}}p_T$, and the inverted transverse momentum of the seed track p_T^{-1}. For each variable we select a region where all efficiencies due to other variables are flat, measure the efficiency as a function of that variable. The function used to fit the transverse momentum of the tau seed track is the standard error function convoluted with the first degree polynomial:

$$\epsilon_p(p_T^{-1}) = K_p \times \epsilon_p^{sh}(p_T^{-1}) = K_p \times (1 - S_p \cdot (p_T^{-1} - 1/10)) \times freq\left(\frac{p_{T_0}^{-1} - p_T^{-1}}{2\sigma_p}\right), \quad \text{(B.9)}$$

where K_p is the efficiency at $p_T^{-1} = 0.1$ $(\text{GeV}/c)^{-1}$, S_p is the slope of the efficiency at plateau region, and the "sh" superscript stands for the "shape" of the distribution. We fit $\Delta\theta^{\text{in}}$ distribution with the standard error function:

$$\epsilon_\Delta(\Delta\theta^{\text{in}}) = K_\Delta \times \epsilon_\Delta^{sh}(\Delta\theta^{\text{in}}) = K_\Delta \times freq\left(\frac{\Delta\theta_0^{\text{in}} - \Delta\theta^{\text{in}}}{2\sigma_{\Delta\theta^{\text{in}}}}\right). \quad \text{(B.10)}$$

And for the $\Sigma^{\text{iso}}p_T$ a simple first degree polynomial is used:

$$\epsilon_I(\Sigma^{\text{iso}}p_T) = K_I \times \epsilon_I^{sh}(\Sigma^{\text{iso}}p_T) = K_I \times (1 - S_{\text{iso}} \cdot \Sigma^{\text{iso}}p_T). \quad \text{(B.11)}$$

Variables p_T^{-1}, $\Delta\theta^{\text{in}}$, and $\Sigma^{\text{iso}}p_T$ are independent of each other, therefore we introduce K_{tot}, the total scaling factor, and present the total efficiency as

$$\varepsilon_{tot} = K \times \varepsilon_p \times \varepsilon_\Delta \times \varepsilon_I = K_{tot} \times \varepsilon_p^{sh} \times \varepsilon_\Delta^{sh} \times \varepsilon_I^{sh}, \quad \text{(B.12)}$$

So at the end we are left with 7 independent parameters.

d. Results

We start with identifying a region for each variable where the efficiency is flat. Then by selecting flat regions in two other dimensions it is easy to find the true efficiency for the variable of interest. The standard cuts used for the flat efficiency region selection in each variable are:

$$p_T^{-1} < 0.18\ c/\text{GeV}, \quad \Delta\theta^{\text{in}} > 0.12\ rad, \quad \Sigma^{\text{iso}} p_T < 0.3\ \text{GeV}/c.$$

Figure 34 shows the $\Delta\theta^{\text{in}}$ and $\Sigma^{\text{iso}} p_T$ variables fitted with the corresponding functions. The overall scaling factor K_{tot} quoted in the Table XL is obtained from the 3-dimensional fit when all shapes in each variable are fixed. The systematic uncertainty for K_{tot} for any number of prongs was estimated to be 0.72%.

TABLE XL: The result for the L3 efficiency parametrization (Eq. (B.12)).

Parameter	1 Prong	2 Prongs	3 Prongs
$\Delta\theta_0^{\text{in}}$	$-0.009^{+0.002}_{-0.003}$		
$\sigma_{\Delta\theta^{\text{in}}}$	$0.012^{+0.0018}_{-0.0014}$		
S_{iso}	$-0.0105^{+0.0009}_{-0.001}$		
$p_{T_0}^{-1}$	$0.1998^{+0.0006}_{-0.0005}$	$0.2000^{+0.0012}_{-0.0001}$	$0.1998^{+0.0016}_{-0.0012}$
σ_p	$0.0022^{+0.0005}_{-0.0004}$	$0.0036^{+0.0010}_{-0.0007}$	$0.0032^{+0.0017}_{-0.0011}$
S_p	$-0.08^{+0.04}_{-0.04}$	$-0.07^{+0.04}_{-0.04}$	$-0.06^{+0.06}_{-0.07}$
K_{tot}, %	$98.90^{+0.11}_{-0.12}$	$98.95^{+0.11}_{-0.11}$	$99.01^{+0.13}_{-0.13}$

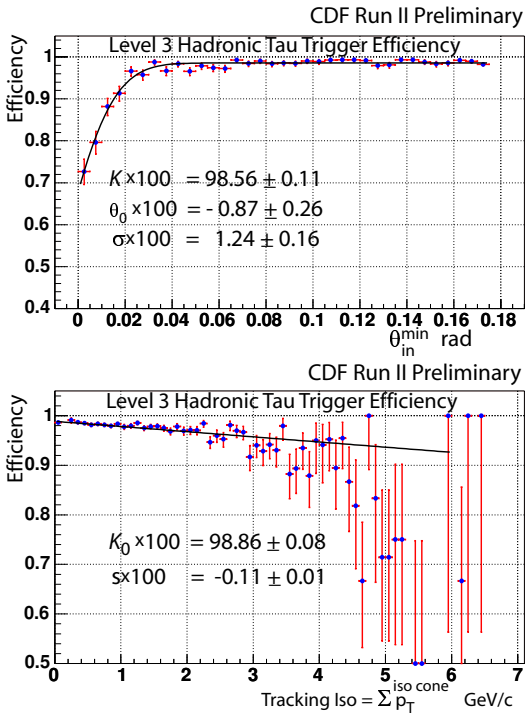

FIG. 34: Efficiency for $\Delta\theta^{\text{in}}$ (Eq. (B.10)) and $\Sigma^{\text{iso}}p_T$ (Eq. (B.11)) for any number of prongs.

B. Efficiency for the Electron Trigger Leg

1. Level 1 and Level 2 Efficiencies

We present the results of a measurement of the electron trigger efficiency for the Level 1 (L1_CEM8_PT8) and Level 2 (L2_CEM8_PT8_CES2) stages of the electron plus track trigger. The trigger requirements for the inclusive 8 GeV electron at L1 and L2 are given in Table III.

We use a sample of electrons coming from several jet and muon triggers by selecting conversion tracks and applying certain electron quality requirements (fiducial etc.). To select a sample of conversion electrons, we require that the two candidate tracks are close in 2D in the point of closest approach of their helices and that tracks have similar cotθ. The background contribution (and corresponding correction to the

efficiency) is estimated using sideband subtraction on the $\Delta\cot\theta$ distribution.

To measure the efficiency and to disentangle various sources of inefficiencies, we perform a detailed simulation of the L1 and L2 decision logic by translating L1 hardware logic and the L2 online Alpha code into AC++ modules. Testing has shown an excellent agreement between the decisions made by actual L1&L2 and the simulated decision (the error rate is about 10^{-3}, comparable with the rate of hardware problems in the trigger), which assures us that the simulation is adequate.

The definition of the electron trigger efficiency determines if a particular electron of interest would have fired the trigger irrespective of all other electrons present in the event. Therefore, an unambiguous matching between the offline electrons and the online objects (trigger towers, XFT tracks, etc.) is necessary. We used a procedure to match electron tracks to one of the XFT tracks found in the event, also requiring that the trigger tower (or a L2 EM cluster) has non-zero overlap with the offline electron calorimeter cluster. Finally, we extract the efficiency and fit it to a standard error function to obtain the efficiency parametrization.

A detailed description of each step could be found in Ref. [63]. Here we quote the results.

For the L1 trigger we use the following efficiency parametrization:

$$\epsilon^{e}_{L1}(E_T, p_T) = K_\infty \times freq\left(\frac{\sqrt{E_T}-\sqrt{E_{T_0}}}{2\sigma_{E_T}}\right) \times freq\left(\frac{1/p_{T_0}-1/p_T}{2\sigma_{1/p_T}}\right), \quad \text{(B.13)}$$

The results of a fit are given in Table XLI. Final numbers are based on using the "decoupled" fits for the case of isolation $I_{R=0.4} \leq 4$ GeV. Systematic uncertainties include all known effects, such as associated with the XFT switch to a "1-miss" scheme, dependence on the allowed number of CES wire clusters, and imprecise knowledge of the background fractions (varied by as much as 30%) and not understood in quantitative details effects of electron isolation.

TABLE XLI: Parameters for the efficiency of the L1_CEM8_PT8 trigger. K_∞ is the asymptotic limit of the efficiency; the other parameters are defined as in Eq. (B.13). We assume that the trigger requires 4-layer XFT track. Parameters E_{T_0} and $1/p_{T_0}$ are strongly (negatively) correlated.

L1_CEM8_PT8
$K_\infty = 0.98 \pm 0.01 \pm 0.01$
$E_{T_0} = 7.93 \pm 0.07 \pm 0.05$ GeV
$\sigma_{E_T} = 0.096 \pm 0.009 \pm 0.006$ GeV
$p_{T_0} = 7.56 \pm 0.09 \pm 0.18$ GeV/c
$\sigma_{1/p_T} = 0.0139 \pm 0.0010 \pm 0.0008$ GeV/c

For the L2 trigger the efficiency parametrization is:

$$\epsilon^e_{L2}(E_T) = 1 - K_\infty \times exp\left(-\frac{E_T - 2.0}{2\sigma_{E_T}}\right) \ . \tag{B.14}$$

The final results are obtained in a way similar to the L1 and are given in Table XLII

TABLE XLII: Parameters for the efficiency of the L2_CEM8_PT8_CES2 trigger as a function of electron cluster E_T. K_∞ is the asymptotic limit of the efficiency, as defined in Eq. (B.14).

L2_CEM8_PT8_CES2
$K_\infty = 1.00^{+0.00}_{-0.013}(stat)^{+0.00}_{-0.014}(sys)$
$\sigma_{E_T} = 1.10 \pm 0.10 \pm 0.12$ GeV

2. Level 3 Efficiency

To measure the L3 efficiency for the electron plus track trigger electron leg we used the same sample of conversions that was used for the L1 and L2 efficiency measurement, and we do it for event that pass L1 and L2 requirements. To match an offline electron and a L3 electron, a pair (offline and L3) of EM clusters is required for at least one overlapping physical tower in the calorimeter. The matching requirement for estimation of the tracking part of the efficiency is that the angle between L3 and offline tracks associated with respective electron objects be less than 0.08 rad.

We measure the efficiency at L3 by disentangling calorimeter and tracking effects. The L3 requirements (Table III) $E_T \geq 8$ GeV and $\chi^2_{\rm strip} \leq 20$ are assigned to calorimeter part, while $p_T \geq 8$ GeV/c and $|\Delta z_{\rm CES}| \leq 8$ cm to tracking part. So the efficiency parametrization is a product of these two parts times a normalization coefficient K_∞:

$$\epsilon^e_{L3}(E_T, p_T) = K_\infty \times freq\left(\frac{\sqrt{E_T} - \sqrt{E_{T_0}}}{2\sigma_{E_T}}\right) \times freq\left(\frac{1/p_{T_0} - 1/p_T}{2\sigma_{1/p_T}}\right) \ . \quad \text{(B.15)}$$

Details of the study are presented in Ref. [64]. We show the resulting parameters in Table XLIII

TABLE XLIII: Parameters for the L3 efficiency for the electron plus track trigger electron leg as defined in Eq. (B.15).

L1_ELECTRON8_TRACK5_ISO
$K_\infty = 0.992^{+0.008}_{-0.009}$
$E_{T_0} = 7.4 \pm 0.3$ GeV
$\sigma_{E_T} = 0.05 \pm 0.03$ GeV
$p_{T_0} = 8.06 \pm 0.06$ GeV/c
$\sigma_{1/p_T} = 0.0010^{+0.0019}_{-0.0010}$ GeV/c

C. Efficiency for the Muon Trigger Leg

The measurement of the efficiency of the L1_CMUP6_PT4 trigger is performed using a $J/\Psi \to \mu\mu$ sample collected with the inclusive CMUP triggers that use L1_CMUP6_PT4. After performing an accurate offline to L3 muon matching, the efficiency is estimated by proper handling of possible trigger bias and background removal using sideband subtraction technique. The study is documented in Ref. [65]. The parametrization of the efficiency is the following one:

$$\epsilon^{\mu}(p_T) = \frac{\gamma}{1 + e^{\alpha p_T + \beta}} \ , \tag{B.16}$$

with the results presented in Table XLIV.

TABLE XLIV: Parameters for the L1_CMUP6_PT4 trigger efficiency as defined in Eq. (B.16).

L1_CMUP6_PT4
$\alpha = -1.35 \pm 0.69$ c/GeV
$\beta = 4.48 \pm 3.38$
$\gamma = 0.957 \pm 0.006$

The L3 CMUP muon trigger efficiency for the LT trigger is estimated using the same $J/\Psi \rightarrow \mu\mu$ sample collected with the inclusive CMUP triggers that was used for the L1 efficiency measurement. And also a sample of $Z \rightarrow \mu\mu$ collected with L3_MUON_CMX18 is used to improve the measurement at high p_T. Using a similar technique as in the L1 study and the same parametrization as in Eq. (B.16), we obtain the result presented in Table XLV [66].

TABLE XLV: Parameters for level 3 CMUP muon trigger efficiency for the LT trigger as defined in Eq. (B.16).

L1_CMUP8_TRACK5_ISO
$\alpha = -6.02 \pm 0.80$ c/GeV
$\beta = 48.0 \pm 6.0$
$\gamma = 0.997 \pm 0.003$

APPENDIX C

CALCULATION OF SCALE FACTORS FOR DRELL-YAN BACKGROUNDS

In this appendix we present the methodology and the results of calculation of the scale factors (SF) for $Z \to ee$ and $Z \to \tau\tau$ MC events.

A. Scale Factors Justification

One of major background (BG) in this study is Drell-Yan (DY) production. After applying fiduciality and ID selections, further event selection relies on differences in kinematical properties of the stop events and leading SM backgrounds. As a part of these event level cuts, we cut on $N_{\rm jet}$, Y_T, and m_T. Accuracy of MC in predicting efficiencies of these cuts are correlated with the accuracy of MC in describing kinematical properties of the Z boson production. From various studies, we know that these quantities are not modeled well in MC, so the event acceptance for the $Z \to \tau\tau$ and $Z \to ee$ processes may be not accurately predicted. Here we attempt to correct MC kinematics of the Z production taking into account their correlation with the Y_T and m_T cuts used in the event selection.

Our inclusive DY samples were generated with PYTHIA. For these events PYTHIA utilizes the 2→1 calculation smeared by ISR. Given that PYTHIA is a LO MC, this calculation is not reliable even at moderate $p_T(Z) \sim 20$ GeV/c because this is already a perturbative process that is still treated as 2→1. Further, it is known that $\not\!\!E_T$ in $Z \to ee$ (CDFSOFT version 5.3.3) disagrees with data because minbias and calorimeter response to jets are not well modeled. All tunings in CDF MC simulation are done on average and may well be off in the part of the phase space that is of interest to us. For example, if we just select $Z(\to ee) + 1$ jet events, even before applying Y_T

and m_T cuts, we find the ratio of data to MC prediction in the number of events to be 0.92 ± 0.05.

B. Calculation of the Scale Factors for $Z \to ee$

We estimate $Z \to ee$ SF by directly comparing $Z \to ee$ events in data and MC in the part of the parameter space where kinematical cuts on Y_T and m_T are already applied. The event selection is similar to one that was used for stop search (Section IV.C) except that we modify some cuts in order to enhance (rather than suppress as in the stop analysis) statistics and to obtain a relatively clean sample of $Z \to ee$ events in data:

- ξ cut is inverted for τ (select electrons instead of taus);
- an electron that matches with τ is required to additionally pass good electron ID cuts;
- 66 GeV $< m(e^+e^-) <$ 116 GeV/c^2 (Z mass window) is required.

The scale factor will be given as:

$$SF^{Z \to ee} = \frac{[\text{Observation in } Z \to ee \text{ data}]}{[\text{Prediction in } Z \to ee \text{ MC}]} \tag{C.1}$$

in a given kinematical region.

The results for different Y_T and m_T cuts are given in Table XLVI. Note that the uncertainties in these SF come dominantly from the limited data statistics.

C. Calculation of the Scale Factors for $Z \to \tau\tau$: Procedure

We cannot use the same technique as in Section C.B for calculation of SF for $Z \to \tau\tau$ events because of very limited statistics in the data sample of $Z \to \tau\tau$ events. We

TABLE XLVI: Scale factors for $Z \rightarrow ee$ events (see Eq. (C.1)) for two values of Y_T requirement.

	Extra Jet Multiplicity		
	0	1	≥ 2
$Y_T > 80$:			
$m_T < 35$	1.00 ± 0.02	0.96 ± 0.05	1.09 ± 0.15
$m_T > 35$	0.87 ± 0.04	0.89 ± 0.08	1.10 ± 0.21
$Y_T > 110$:			
$m_T < 35$	1.07 ± 0.13	0.99 ± 0.12	1.28 ± 0.27
$m_T > 35$	0.87 ± 0.13	0.91 ± 0.12	1.19 ± 0.28

propose a technique to evaluate the SF for $Z \rightarrow \tau\tau$ events using $Z \rightarrow ee$ MC and data and $Z \rightarrow \tau\tau$ MC events.

The $Z \rightarrow \tau\tau$ and $Z \rightarrow ee$ events are originated from the same physics process $p\bar{p} \rightarrow Z + X$, and have exactly the same kinematics of Z boson. One cannot study these variables directly with $Z \rightarrow \tau\tau$ events because neutrinos escaping the detector do not allow reconstruction of the Z boson properties as it can be done in $Z \rightarrow ee$ events. With a good assumption that Z decays are modeled well by MC, we can use $Z \rightarrow ee$ events in data and MC to study (and to correct) distributions related to Z production and then apply the same corrections to $Z \rightarrow \tau\tau$ MC events.

The procedure has the following steps: choice of the variables to parametrize kinematics of Z boson production (Section C.C.1); calculation of SFs using $Z \rightarrow ee$ events as a function of these parameters (Section C.C.2); and applying these corrections to the $Z \rightarrow \tau\tau$ MC events (Section C.C.3). An important point here is that in obtaining the SFs, we use $Z \rightarrow ee$ events with only minimal kinematical selections to

ensure that the parameter space in which corrections are calculated (which is done using $Z \to ee$ events) is broader than the parameter space relevant to the $Z \to \tau\tau$ events that make it into the final stop sample (for which we do apply cuts on Y_T and m_T).

1. Choice of Variables for the Mapping Procedure.

We have performed a similar SF study in the earlier stage of this analysis [84], where we used N_{jet}, $p_T(Z)$ and $\eta(Z)$ to map the two processes. Here we reevaluate the choice of the variables. Proper variables for use in the mapping procedure should satisfy the following requirements:

1) to have a direct correspondence between $Z \to ee$ and $Z \to \tau\tau$;

2) their set should be enough to describe the data/MC disagreement with respect to application of the N_{jet}, Y_T and m_T cuts used in stop event selection;

3) to be not strongly correlated between each other;

4) to be well defined and can be measured in $Z \to ee$ data/MC and $Z \to \tau\tau$ MC events.

We considered several possible variables, but the final set of variables that was satisfying the mentioned above requirements is N_{jet}, $p_T(Z)$ and $\not\!\!E_T{}^{\text{instr}}$, where $\not\!\!E_T{}^{\text{instr}}$ is

$$\not\!\!E_T{}^{\text{instr}} = \begin{cases} Z \to ee: & \not\!\!E_T, \\ Z \to \tau\tau: & \not\!\!E_T \text{ minus contribution from neutrinos, and corrected} \\ & \text{for the difference between HEPG tau momentum and} \\ & \text{reconstructed tau cluster momentum,} \end{cases} \tag{C.2}$$

which we call "instrumental" missing energy.

2. *Dependence of $Z \to ee$ SF on $N_{\rm jet}$, $p_T(Z)$ and $\not\!\!E_T^{\rm instr}$*

For each jet multiplicity ($N_{\rm jet}= 0, 1, \geq 2$), we find an analytical function of $Z\to ee$ SF dependence on $p_T(Z)$ and $\not\!\!E_T^{\rm instr}$ that fits a binned $p_T(Z)$ vs. $\not\!\!E_T^{\rm instr}$ $Z\to ee$ SF distribution the best. This task is simplified by the fact that $p_T(Z)$ and $\not\!\!E_T^{\rm instr}$ have weak correlation. It allows us to perform two separate 1D fits and use their product time some normalization coefficient C to obtain the 2D dependence:

$$SF_N^{Z\to ee}(p_T(Z), \not\!\!E_T^{\rm instr}) = C \times f_N(p_T(Z)) \times g_N(\not\!\!E_T^{\rm instr}), \tag{C.3}$$

where we estimate functions $f_N(p_T(Z))$ and $g_N(\not\!\!E_T^{\rm instr})$ as 3^{rd} degree polynomials. The coefficients of the polynomials are given in Table XLVII. The normalization coefficient is constrained by imposing an additional requirement that the corrected number of $Z\to ee$ MC events is equal to the number of $Z\to ee$ data events for each $N_{\rm jet}$ bin.

TABLE XLVII: The coefficients of the polynomial function $f(x) = a_0 + a_1 x + a_2 x^2 + a_3 x^3$ (with x being either $p_T(Z)$ or $\not\!\!E_T^{\rm instr}$) used to fit the distributions for $Z \to ee$ data to MC ratios.

	N_{jet}	a_0	a_1	a_2	a_3
$p_T(Z)$	0	1.03 ± 0.05	$(-1.5 \pm 1.4) \times 10^2$	$(1.2 \pm 1.0) \times 10^3$	$(-1.4 \pm 1.7) \times 10^5$
	1	0.36 ± 0.19	$(2.8 \pm 1.3) \times 10^2$	$(-3.2 \pm 2.7) \times 10^4$	$(0.9 \pm 1.4) \times 10^6$
	≥ 2	1.1 ± 0.3	$(-1.4 \pm 4.6) \times 10^3$	0	0
$\not\!\!E_T$	0	1.22 ± 0.05	$(-5.0 \pm 1.2) \times 10^2$	$(1.7 \pm 0.7) \times 10^3$	0
	1	0.87 ± 0.12	$(1.1 \pm 2.4) \times 10^2$	$(-4.3 \pm 9.3) \times 10^4$	0
	≥ 2	1.0 ± 0.3	$(0.6 \pm 2.6) \times 10^2$	0	0

3. Calculation of $Z \to \tau\tau$ SF

We calculate the scale factor for events with N extra jets as

$$SF_N = \sum_{i=1}^{K_N} w_{iN} \times s_{iN}, \tag{C.4}$$

where K_N is the total number of bins in the $p_T(Z)$ vs. $\not\!\!E_T{}^{\rm instr}$ 2D space,

$$w_{iN} = z_{iN} / \sum_i z_{iN}, \tag{C.5}$$

$$s_{iN} \equiv SF_N^{Z\to ee}(p_{Ti}(Z), \not\!\!E_{Ti}{}^{\rm instr}), \tag{C.6}$$

where z_{iN} is the number of $Z{\to}\tau\tau$ MC events in i^{th} bin for events with N extra jets; $p_{Ti}(Z)$ and $\not\!\!E_{Ti}{}^{\rm instr}$ are the coordinates of i^{th} bin center.

The uncertainty of the scale factor due to w_{iN} is calculated as

$$\Delta SF_N^{stat} = \sqrt{\sum_i (\Delta w_{iN})^2 \times s_{iN}^2}. \tag{C.7}$$

Note that ΔSF_N^{stat} in Eq. (C.7) is driven by statistics of the $Z{\to}\tau\tau$ MC sample. In order to avoid double-counting this uncertainty should not be included when applying these scale factors to correct the number of events in $Z{\to}\tau\tau$ MC.

There should also be a contribution to ΔSF_N due to Δs_{iN}. We estimate the systematic uncertainty as

$$\Delta SF_N^{sys} = \sqrt{\sum_i w_{iN}^2 \times (\Delta s_{iN})^2}. \tag{C.8}$$

One can evaluate Eq. (C.8) with Δs_{iN} obtained from the fit covariance matrix and the fit parameters uncertainties. We, however, choose a different technique estimate the "systematics" for $Z \to \tau\tau$ SF we calculate the RMS of SFs over 12 trial samples, which were made by splitting a large $Z \to ee$ MC sample into 12 parts. We

perform the SF calculations for both trial and combined samples, considering them respectively as if they were new "data" and "MC". We pick one of the 12 samples as a test sample and combine the remaining 11 into a one large sample. Thus we have 12 combinations that give us 12 SF estimates. Note that the combined samples between these various combinations are correlated, but the test samples are independent. As expected, both methods of systematic uncertainty estimation produce similar results. However the systematic uncertainties obtained with this method are slightly bigger, so we use it for the final results.

D. Calculation of the Scale Factors for $Z \to \tau\tau$: Results

For $Z \to \tau\tau$ events selected with $Y_T > 80$ GeV and $Y_T > 110$ GeV we apply the "mapping" procedure, and obtain the results for the SFs presented in Table XLVIII. Figure 35 shows the SF dependencies on the Y_T cut value (only stat uncertainties shown). Only systematic parts of the uncertainties should be applied in $Z \to \tau\tau$ BG scaling to avoid a double counting.

TABLE XLVIII: Scale factors for $Z \to \tau\tau$. See Eq. (C.4). The first and second uncertainties are statistical and systematical uncertainties.

	Jet Bin		
	0	1	≥ 2
$Y_T > 80$:			
$m_T < 35$	$1.02 \pm 0.02 \pm 0.02$	$0.97 \pm 0.04 \pm 0.04$	$1.06 \pm 0.09 \pm 0.10$
$m_T > 35$	$1.00 \pm 0.05 \pm 0.02$	$0.97 \pm 0.08 \pm 0.04$	$1.05 \pm 0.18 \pm 0.16$
$Y_T > 110$:			
$m_T < 35$	$1.00 \pm 0.10 \pm 0.02$	$0.90 \pm 0.09 \pm 0.14$	$1.02 \pm 0.19 \pm 0.18$
$m_T > 35$	$0.99 \pm 0.18 \pm 0.02$	$0.94 \pm 0.23 \pm 0.11$	$1.03 \pm 0.23 \pm 0.19$

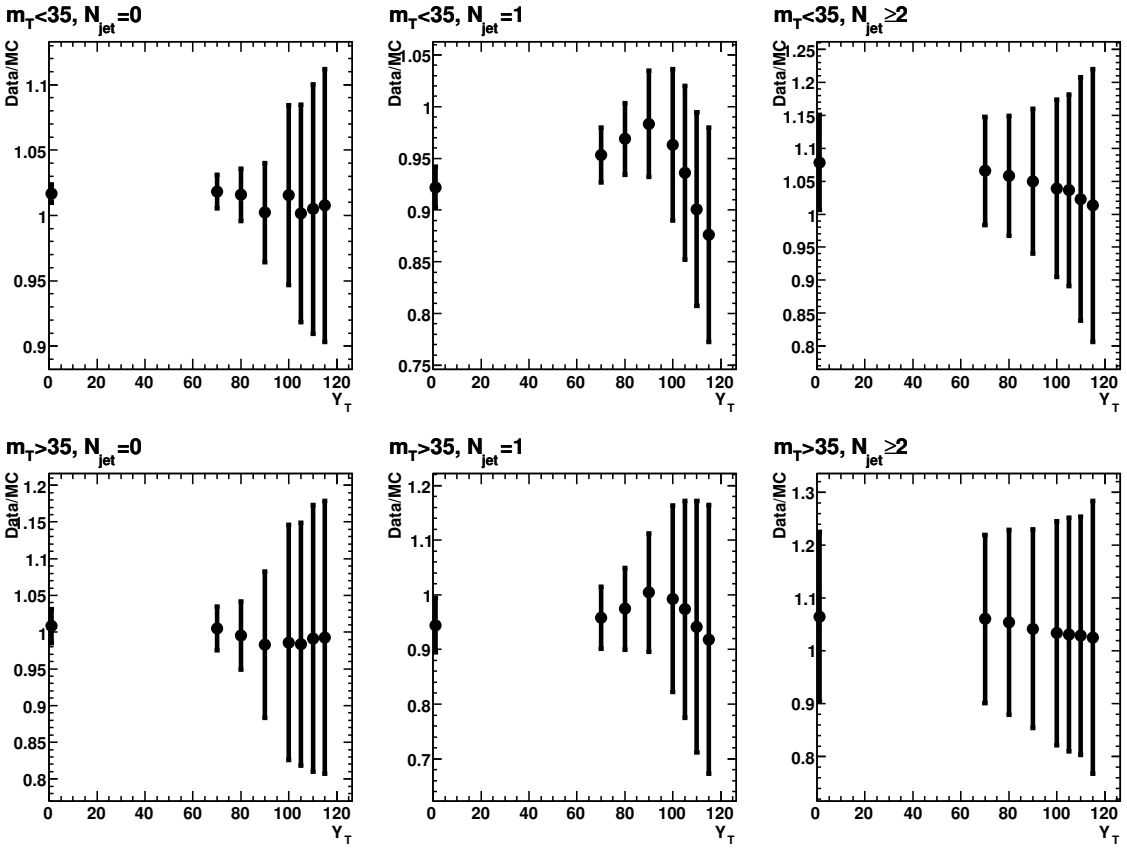

FIG. 35: $Z \to \tau\tau$ SF dependence on Y_T cut value for events with various jet multiplicity (from left to right) with $m_T < 35$ GeV/c^2 (top) and $m_T > 35$ GeV/c^2 (bottom). Only statistical uncertainties from $Z \to \tau\tau$ are shown.

APPENDIX D

INTERPRETATION OF THE RESULTS FOR THIRD GENERATION SCALAR LEPTOQUARKS

The remarkable symmetry observed in the SM between quarks and gluons may lead one to a thought that there might be a deeper connection between those particle classes. Leptoquarks (LQs) are hypothetical particles that are predicted by many extensions to the SM. They can interact with leptons and with quarks and carry both, lepton and baryon number. LQ might have spin 0 or 1, are color triplets and have fractional electric charge. Limits on four-fermion interactions [14] and the muon anomalous magnetic moment measurement suggest that a LQ state couples only to a single generation in a chiral interaction. So, e.g., a LQ state which couple to the third generation of quarks and leptons is called a third generation leptoquark or shortly LQ_3. In the following we will use LQ_3 notation only for a scalar 3^{rd} generation LQ. LQ may decay either into a quark and a charged lepton or into a quark and neutrino. We will briefly review theories predicting LQ particles.

Grand Unification Theories (GUTs) postulate a unified group, e.g. $SU(5)$ [90] or $SO(10)$ [91], with a single coupling constant. Leptoquarks emerge in GUT as a class of gauge bosons that mediate interactions between leptons and quarks in the same multiplet. Pati-Salam models might now be considered as part of some GUT theories, and originally they treated lepton number as the fourth color, extending the $SU(3)_C$ to the $SU(4)_C$ symmetry group [92]. However, in order to preserve a proton from rapid decay, most of GUT theories have strong limits on baryon number violation that lead to very high mases of LQ particles at the scale of $M_{\text{GUT}} \approx 10^{16}$ GeV/c^2. Some GUT models though predict light scalar LQ with masses within current experimental

bounds and provide mechanism for neutrino mass generation (see Ref. [93] for a resent example).

Scalar LQ are expected to exist at TeV scale in extended technicolor models [94, 95] where leptoquark states appear as the bound states of techni-fermions. Compositeness of quarks and leptons also provides examples of models which may have light leptoquark states [96].

What is important for our analysis, scalar quarks in RPV SUSY models may also have leptoquark-type Yukawa couplings, which are λ'_{ijk} (Eq. (1.3)). Thus, supersymmetric top quark has interaction properties very similar to LQ_3 in other leptoquark models. Stop pair production and decay Feynman diagrams at tree level (Figure 1) are the same as for LQ_3. It should be noted that there is one more diagram that contributes to the LO stop pair production, which is the gluino exchange $t\bar{t} \rightarrow$ (t-channel gluino exchange) $\rightarrow \tilde{t}_1\bar{\tilde{t}}_1$. However, this diagram is strongly suppressed by negligibly low contents of sea t-quarks in parton distribution functions (PDF) and high expected gluino mass. At NLO there will be more dependence on different SUSY parameters, mostly on gluino mass. However, we checked that for the existing limits on gluino mass [97] the NLO cross section for $LQ_3\overline{L}Q_3$ production is very close to that for $\tilde{t}_1\bar{\tilde{t}}_1$. We did it by widely varying gluino mass when calculating $\sigma(\tilde{t}_1\bar{\tilde{t}}_1)$. For example, the difference in $\sigma(\tilde{t}_1\bar{\tilde{t}}_1)$ for the case of gluino mass of 200 GeV/c^2 and the case of a very heavy gluino is about 3% (for $m(\tilde{t}_1) = 150$ GeV/c^2).

From the symmetry consideration, there are nine scalar and nine vector LQ species possible. Following the notation from Ref. [14], the following species of scalar LQ posses properties similar to the PRV stop: $\bar{S}_0(-4/3)$, $S_1(-4/3)$, $S_{-1/2}(-2/3)$, and $\bar{S}_{1/2}(-2/3)$, where lower indices represent the weak isospin projection and the number in brackets is the electric charge. Charge-4/3 LQ_3 will always decay into τb, and charge-2/3 LQ may decay into $\tau\bar{b}$ and when $m(LQ_3) > m(t)$ into $t\nu_\tau$. The fact

that $\mathcal{B}(LQ_3 \to \tau b) = 1$ while $m(LQ_3) < m(t)$ provides an additional motivation for the search.

Thus, the limit results obtained here for $\not{R}_p$ stop should be fully applicable to the case of LQ_3 pair production. Previous LQ_3 searches at LEP [15] (model independent) and CDF [16] resulted in 95% C.L. limit on $m(LQ_3) > 99$ GeV/c^2. Figure 36 is similar to Fig. 27 except that it shows the result for LQ_3 pair production.

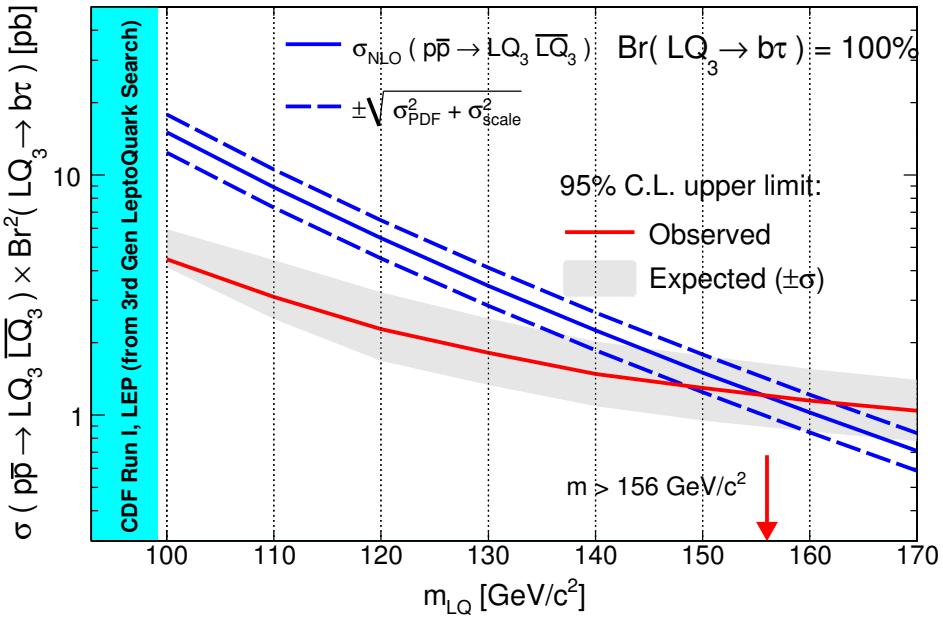

FIG. 36: Theoretical prediction of the pair production cross section (solid blue curve) for the third generation scalar leptoquark (LQ_3) and its uncertainty due to factorization and normalization scales combined with the PDF error (dashed blue curves). Solid red curve shows the observed 95% C.L. limit for the LQ_3 production cross section obtained by combining data in electron and muon channels. The previous limits from CDF and LEP leptoquark searches ($m(LQ_3) > 99$ GeV/c^2) are also shown. In all cases we assume the branching ratio $LQ_3 \to \tau b = 100\%$. Projected 95% C.L. upper limit for the $\tilde{t}_1\bar{\tilde{t}}_1$ production cross section is shown as a grey band (corresponds to a 68% probability range of possible limit if data were to follow SM background expectation). The 95% C.L. limit on LQ_3 mass at $m(LQ_3)$ >156 GeV/c^2 was set without taking into account uncertainties on theoretical cross section.

VITA

Vadim Khotilovich was born in 1978 in Glubokoe, Belarus. He graduated from Kirovskaya middle school in 1994. He attended Belarus State University from 1994 to 2000. His major was physics with specialization in theoretical physics and the minor degree was in computer science. Upon graduation with a B.S. he started a graduate program at Belarus State University. In the winter of 2001 he joined Texas A&M University and began working with experimental high energy physics group. He received a Ph.D. in Physics from Texas A&M University in May 2008. His permanent mailing address is Department of Physics, 4242 TAMU, College Station, TX 77843-4242. His email is khotilovich@tamu.edu.

The typist for this dissertation was Vadim Khotilovich.